Title	Galaxy Evolution and Radiative Properties in the Epoch of Reionization: multi-wavelength analysis in cosmological hydrodynamic simulations
Author(s)	荒田, 翔平
Citation	大阪大学, 2020, 博士論文
Version Type	VoR
URL	https://doi.org/10.18910/76405
rights	
Note	

Galaxy Evolution and Radiative Properties in the Epoch of Reionization: multi-wavelength analysis in cosmological hydrodynamic simulations

Ph.D. thesis in Physics

Author:

Shohei Arata

Department of Earth and Space Science,

Graduate School of Science, Osaka University

March 2020

Abstract

Based on the structure formation of the cold dark matter with the cosmological constant (Λ-CDM cosmology), dwarf galaxies initially form in the early Universe and evolve into the Milky Way-like massive galaxies via frequent mergers. Since the 'first galaxies' are building blocks of present galaxies, understanding of the formation and evolution mechanisms is crucially important for astronomy.

Due to development of observational facilities, galaxies in the early epoch (first billion years from the Big Bang; redshift $(z) \gtrsim 6$) have been observed in multi-wavelength: rest-ultraviolet (UV), infrared (IR, due to dust emission), metal emission lines. These observations revealed wide varieties of the galactic radiative properties e.g., Lyman-α emitters, sub-millimeter galaxies and [O III] and/or [C II] emitting galaxies. It has not been understood yet that how the variety are created and how it relates to galaxies evolution.

Combining cosmological hydrodynamic simulations and radiative transfer calculations, we investigate galaxy evolution and radiative properties at $z = 6 - 15$. The star formation proceeds intermittently due supernova (SN) feedback and gas accretion. In star-burst phases, UV photons are efficiently absorbed by dusty clouds, meanwhile can escape easily in outflowing phases. We find that the escape fraction of UV light fluctuates between $20 - 80\,\%$ via theses processes.

Associating with the changes of escape fraction, IR luminosity due to dust re-emission also fluctuates. The spectral energy distribution (SED) becomes IR-bright in star-burst phases, which could be detectable in sub-mm wavelength on the ground. The sub-mm flux of a galaxy with the DM halo mass of $\sim 10^{11}\,\mathrm{M_\odot}$ ($\sim 10^{12}\,\mathrm{M_\odot}$) at $z = 6$ reaches $\sim 0.1\,\mathrm{mJy}$ ($\sim 1\,\mathrm{mJy}$), which is consistent with previous observations. We further study the observability of sub-mm galaxies using large samples of high-z galaxies. We find that observations with the detection threshold of 0.1 mJy (0.01 mJy) can detect $10^{11}\,\mathrm{M_\odot}$ ($10^{10.5}\,\mathrm{M_\odot}$) haloes with $50\,\%$ probability.

[O III] line is emitted only in star-burst phases, because $\mathrm{O^{2+}}$ ions exist in H II regions formed by massive stars. The luminosity fluctuates between $\sim 10^{40} - 10^{42}\,\mathrm{erg\ s^{-1}}$ at $z = 6 - 10$. Meanwhile, [C II] line is continuously emitted from neutral gas even in outflowing phases. We find that deep [C II] observation ($\sim 10^{-2}\,\mathrm{mJy\ arcsec^{-2}}$) will reveal the $\sim 20\,$physical kpc extended neutral gas distribution. We also find that the $L_{\mathrm{[O\,III]}}/L_{\mathrm{[C\,II]}}$ ratio decreases from ~ 10 to ~ 1 with increasing metallicity from $\sim 0.1\,\mathrm{Z_\odot}$ to $\sim \mathrm{Z_\odot}$. The O/C abundance ratio is initially high, which is dominated by Type-II SNe, but decreases due to the carbon-rich winds from AGB stars. Furthermore, we investigate the average [C II] surface brightness

profile by stacking over many galaxy samples. As a result, the profile is very peaky at the central region ($r < 5$ physical kpc) and smoothly extends outer part. The [C II] observation showed flatter profile over ~ 10 kpc, which implies that unresolved physics remains in the simulations.

Our simulations show that radiative properties in the first galaxies rapidly changes due to intermittent star formation, which generates the observational varieties. We also present that the theoretical models for star formation and feedback processes can be tested by directly comparing our simulations to the observations. For example, we show how the deviation from the Kennicutt–Schmidt law affects the $L_{[\mathrm{O\,III}]}/L_{[\mathrm{C\,II}]}$ ratio and [C II] surface brightness profile. Deep observations by the next generation telescopes will constrain star formation model at high-z.

The consistency between our simulations and observations implies the validity of the Λ-CDM theory. We also suggest that there are abundant high-z galaxies with low-mass DM haloes which have been missed by UV observations so far, which would change the faint-end of UV luminosity function and the estimation of star-formation rate density. However, the number of samples in our simulations is quite limited. We will study the statistical properties of high-z galaxies using large-scale simulation boxes in our future work.

Contents

Chapter 1

Introduction

In this chapter, we briefly explain the history of research for galaxy formation and evolution. We also describe theoretical and observational advances.

1.1 Structure Formation and First Galaxies

One of the biggest goals of astronomy is to self-consistently connect between the beginning and the present-day Universe. The Universe was created in the form of a single point (the *Big Bang*), rapidly increased its volume by inflation, and has been expanding until today. The cosmic expansion law is described by the general relativity with the assumption of *homogeneous* and *isotropic* geometry, so-called the Freedman equation,

$$H^2 = \frac{8\pi G}{3c^2}\varrho - \frac{c^2 K}{a^2} + \frac{c^2\Lambda}{3}, \tag{1.1}$$

where $H \equiv \dot{a}/a$ is the Hubble parameter which represents the rate of expansion at the time t, and $a(t)$ is the scale factor that is related to the cosmic time as $t = \int (1/aH)da$. The $\varrho = \varrho_{\rm m} + \varrho_{\rm r}$ is total energy density of relativistic (radiation) and non-relativistic (matter) components. The matter is composed of baryons and cold dark matter (CDM), and follows $\varrho_{\rm m} \propto a^{-3}$, representing that the energy density decreases with the increasing comoving volume of the Universe. The CDM is thought to be collision-less particles that interact with each other only via gravity. The radiation is composed of photons and neutrinos, which follows $\varrho_{\rm r} \propto a^{-4}$ including the effect of increasing wavelength with cosmic expansion. The K is the curvature of the geometry ($K > 0$ for open, $K = 0$ for flat, and $K < 0$ for closed Universe). The parameter Λ is the 'cosmological constant', which represents a repulsive force against gravity, and is time-independent. More general term for the origin of the accelerating expansion of the Universe is the *dark energy* whose energy density depends on time as $\varrho_{\rm d} \propto \exp\left[-3\int_0^a (1 + w_d)/a da\right]$, where w_d is a parameter of the equation of state (Peebles & Ratra, 1988, 2003). When $w_d = -1$, the dark energy is identical to the

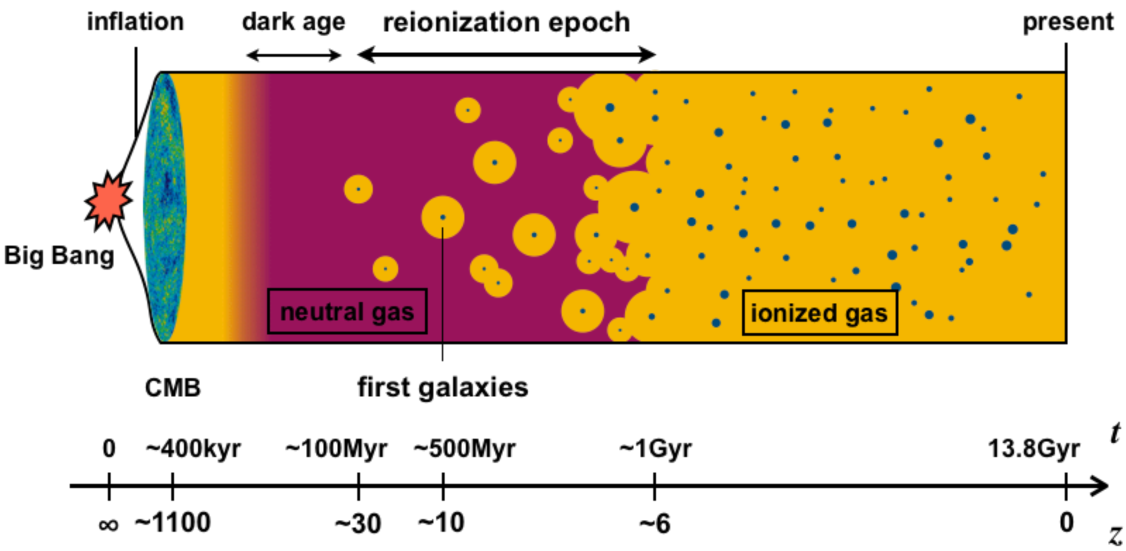

Figure 1.1: Schematic picture of the cosmic thermal history. Yellow and purple colors represent ionized and neutral hydrogen, respectively. Blue dots represent galaxies that form ionized bubbles. The map of the CMB is cited from a website of the Wilkinson Microwave Anisotropy Probe (WMAP, https://map.gsfc.nasa.gov/).

cosmological constant Λ. The standard cosmological model is called ΛCDM theory. The total energy density for the present-time $t = t_0$ in the flat Universe ($K = 0$) is derived from the Freedman equation, $\varrho_{\mathrm{cr},0} = 3c^2 H_0^2/8\pi G$, which is called the critical energy density. Then equation (1.1) can be rewritten as

$$\dot{a}^2 = H_0^2 \left(\frac{\Omega_{\mathrm{r}0}}{a^2} + \frac{\Omega_{\mathrm{m}0}}{a} + \Omega_{\mathrm{K}0} + \Omega_{\Lambda 0} a^2 \exp\left[3 \int_a^{a_0} (1 + w_d) \frac{da}{a} \right] \right), \tag{1.2}$$

where

$$\Omega_{\mathrm{A}0} \equiv \frac{\varrho_{\mathrm{A},0}}{\varrho_{\mathrm{cr},0}} = \frac{8\pi G \varrho_{\mathrm{A},0}}{3c^2 H_0^2}, \quad \Omega_{\mathrm{K}0} \equiv \frac{\varrho_{\mathrm{K}}}{\varrho_{\mathrm{cr},0}} = -\frac{c^2 K}{H_0^2}, \quad \Omega_{\Lambda 0} \equiv \frac{\varrho_{\Lambda}}{\varrho_{\mathrm{cr},0}} = \frac{c^2 \Lambda}{3H_0^2}. \tag{1.3}$$

These density parameters are fundamental for characterising the cosmic evolution, which can be determined only from observations.

Just after the inflation, gas is highly dense and completely ionized, also optically thick to Thomson scattering. The gas temperature decreases adiabatically with cosmic expansion and the neutral fraction of hydrogen gradually increases, then photons begin to move freely at a few 10^5 yr after the Big Bang (redshift (z) ≈ 1100). The last-scattering surface has been observed as the *cosmic microwave background* (CMB) radiation with the temperature of $\approx 2.7\,\mathrm{K}$ with the Cosmic Background Explorer (COBE, Mather et al., 1990; Smoot et al., 1992; Bennett et al., 1996) [1],

[1] https://lambda.gsfc.nasa.gov/product/cobe/

the Wilkinson Microwave Anisotropy Probe (WMAP, Spergel et al., 2003; Komatsu et al., 2009; Larson et al., 2011; Bennett et al., 2013; Hinshaw et al., 2013) [2] and the ESA Planck Satellite (Planck Collaboration et al., 2014, 2016, 2018) [3]. Analyzing the CMB anisotropies of temperature and polarization, the cosmological parameters in a spatially-flat ΛCDM Universe are constrained as $H_0 = 67.4 \pm 0.5$ km s^{-1} Mpc^{-1}, $t_0 = 13.8 \pm 0.02$ billion years, $\Omega_{\rm m0} = 0.315 \pm 0.007$ and the scalar spectral index $n_s = 0.965 \pm 0.04$ (Planck Collaboration et al., 2018). In addition, the cosmological parameters have been constrained using the distant ladder of Type-Ia supernovae (Riess et al., 1998; Perlmutter et al., 1999; Riess et al., 2004, 2007; Kowalski et al., 2008), and using the baryon acoustic oscillations (Seo & Eisenstein, 2003; Eisenstein et al., 2005; Percival et al., 2007, 2010; Anderson et al., 2014; Delubac et al., 2015). Combining results of those methods, the dark energy-dominated flat Universe ($\Omega_{\rm K0} = 0$) with constant dark energy ($w_d = -1$) is the most plausible so far.

After the CMB era ($z \approx 1100$), the gas temperature further decreases with time, and eventually hydrogens become neutral atoms. This epoch is called the *dark age* (see Figure 1.1). On the other hand, the CDM aggregates by gravity and forms clumps (DM haloes) which evolve into more massive DM haloes via frequent mergers (see Figure 1.2). This scenario is called 'hierarchical structure formation' in the ΛCDM model (Press & Schechter, 1974; White & Rees, 1978; Lacey & Cole, 1993; Navarro et al., 1996, 1997; Sheth & Tormen, 1999; Somerville & Kolatt, 1999; Sheth & Tormen, 2002; Reed et al., 2003; Springel et al., 2005b; De Lucia & Blaizot, 2007; Boylan-Kolchin et al., 2009; Guo et al., 2011; Vogelsberger et al., 2014). Gas falls into the gravitational potential of the DM haloes. The collisional gas particles generate shocks during mergers, and the gas cools due to energy release via radiation and form stars. Thus the formation of *first galaxies* is related to the DM assembly history (Rees & Ostriker, 1977; Blumenthal et al., 1984; Davis et al., 1985; Couchman & Rees, 1986; White & Frenk, 1991; Efstathiou, 1992; Kauffmann et al., 1993, 1999; Haardt & Madau, 1996; Tegmark et al., 1997; Barkana & Loeb, 2001; Abel et al., 2002; Yoshida et al., 2006, 2008; Greif et al., 2008, 2010; Wise et al., 2012a,b).

The first galaxies produce ionizing photons and form H II bubbles in the intergalactic medium (IGM). As galaxy formation and evolution proceed, the ionized regions extend and overlap, and finally hydrogen is almost completely ionized again (Fig. 1.1). This duration is called the *epoch of reionization* (EoR) which is ended at $\sim$ 1 billion years after the Big Bang ($z \sim 6$, see Section 1.2 for observational evidences). Numerical models show that low-mass haloes initially contribute to the reionization because of their huge abundance and high escape fraction, but massive

[2] https://map.gsfc.nasa.gov/
[3] https://www.cosmos.esa.int/web/planck

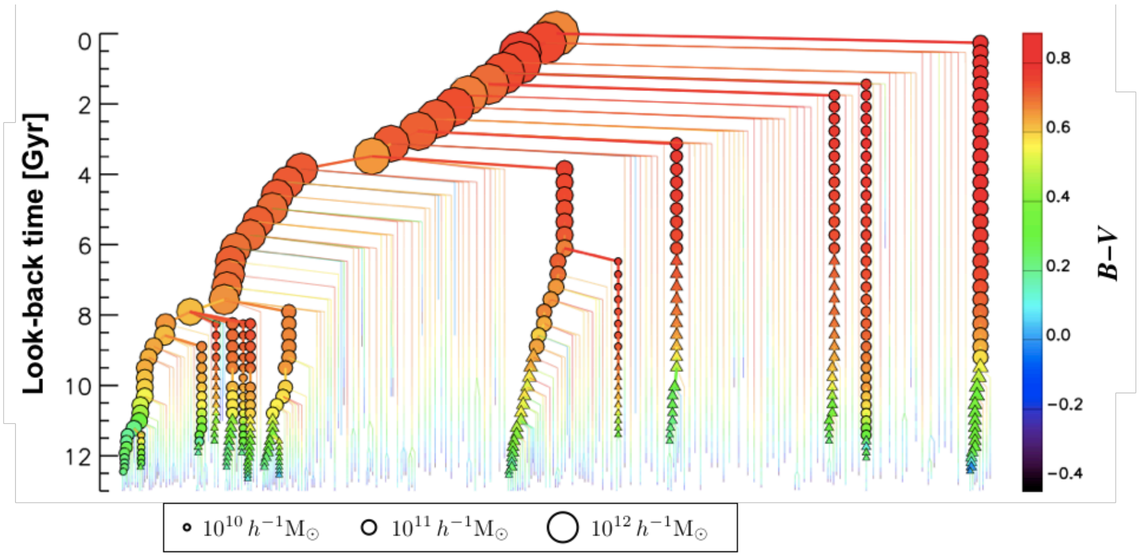

Figure 1.2: Assembly history of DM haloes produced by N-body simulation (altered from De Lucia & Blaizot, 2007). The size of symbols represents the mass of the halo. The filled color is scaled by the spectral color $(B - V)$ of associating galaxies.

haloes become main sources in later phase due to producing copious ionizing photons (Gnedin, 2000a,b; Ricotti et al., 2002a,b; Furlanetto et al., 2004; Dijkstra et al., 2004; Shapiro et al., 2004; Iliev et al., 2006, 2007; McQuinn et al., 2007; Gnedin et al., 2008; Petkova & Springel, 2011; Haardt & Madau, 2012; Wise et al., 2014; Kimm & Cen, 2014; Paardekooper et al., 2015; Ma et al., 2015; Xu et al., 2016). The first galaxies further evolve into more massive ones via galaxy mergers, and finally become present galaxies like the Milky Way. Therefore, the first galaxies are building blocks or initial conditions of present galaxies. Understanding of their formation mechanism is crucial to test the validity of the ΛCDM theory. In addition, it is well-known that present galaxies have a tight correlation between the mass of the central black hole (BH) and the stellar velocity dispersion of the spheroidal component, so-called Maggorian relation (Magorrian et al., 1998; Ferrarese & Merritt, 2000) (see Kormendy & Ho, 2013, for review). This implies that the feedback from star formation affects BH growth during galaxy evolution. The first galaxies are the formation sites of seed BHs, and quasar (quasi-stellar object, QSO) observations show that super-massive BHs ($M_{\rm BH} \sim 10^8 - 10^9\,\mathrm{M}_\odot$) have already been formed at $z \sim 6$ (see Section 1.2). The 'co-evolution' process for the galaxies and the BHs has been studied theoretically (Silk & Rees, 1998; Fabian, 1999; Kauffmann & Haehnelt, 2000; King, 2003; Granato et al., 2004; Di Matteo et al., 2005, 2008, 2012; Hopkins et al., 2006; Li et al., 2007; Somerville et al., 2008; Schaye et al., 2010; Sijacki et al., 2015; Katz et al., 2015; Anglés-Alcázar et al., 2017). They found that BHs rapidly grow via galaxy mergers, and the feedback from the active galactic nuclei (AGN),

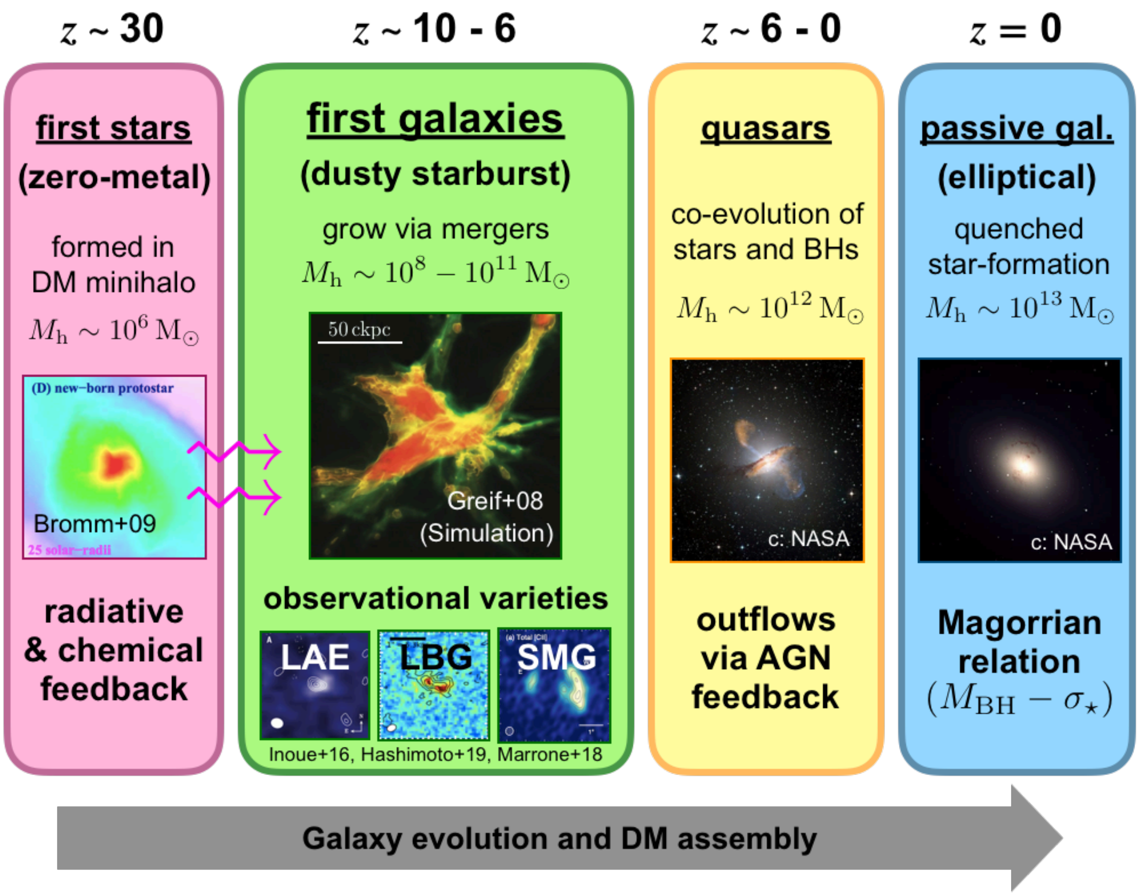

Figure 1.3: Schematic view of a galaxy evolution which we suppose based on the results of numerical studies (see text). Inserted figures are altered from Greif et al. (2008); Bromm et al. (2009); Inoue et al. (2016); Marrone et al. (2018); Hashimoto et al. (2019).

which are activated by the central BHs, becomes more powerful as galaxy evolves. The AGN feedback finally expels the gas from the galaxies and quenches the star formation when the stellar mass becomes $\sim 10^{10}\,\mathrm{M}_\odot$ (see Figure 1.3).

To understand how the first galaxies affect subsequent cosmic history, it is crucially important to constrain feedback processes. There are two-types of stellar feedback; radiative and supernova feedback. The supernovae (SNe) supply huge momentum and energy into the surrounding gas. It also enriches galaxies with heavy elements that enhances radiative cooling, resulting in changing stellar population. This is because the gravitational collapsing scale (Jeans length, λ_J) decreases with temperature,

$$\lambda_\mathrm{J} = \sqrt{\pi c_s^2/G\rho} = 1.06 \times 10^3 \left(\frac{\mu}{0.6}\right)^{-1} \left(\frac{T}{10^4\,\mathrm{K}}\right)^{1/2} \left(\frac{n_\mathrm{H}}{10\,\mathrm{cm}^{-3}}\right)^{-1/2} \mathrm{pc}, \qquad (1.4)$$

where c_s is the sound speed, G is the gravitational constant and ρ is the mass density.

In the right-hand side of the second equality, μ is the mean molecular weight that is 0.6 for ionized primordial gas, T is the gas temperature and $n_{\rm H}$ is the number density of hydrogen nuclei. The spectral energy distribution (SED) depends on the stellar mass, thus the stellar population in the first galaxies is one of important ingredients for observations. Some theoretical studies show that the critical metallicity for switching from the birth of first stars or Population III (Pop. III) stars to that of Population II (Pop. II) stars lies at $\sim 10^{-6} - 10^{-4}\,{\rm Z}_{\odot}$, and most of the first galaxies at $z \sim 10$ were enriched by pre-existing progenitors (Haiman et al., 1996; Galli & Palla, 1998; Oh & Haiman, 2002; Bromm & Loeb, 2003; Omukai et al., 2005, 2008; Trenti & Stiavelli, 2009; Maio et al., 2010; Greif et al., 2010; Safranek-Shrader et al., 2012, 2014; Chiaki et al., 2013b). The formation sites of Pop. III stars are *minihaloes* with the DM mass of $\sim 10^{6}\,{\rm M}_{\odot}$ at $z \sim 20 - 30$ and the cooling source is radiation of molecular hydrogen (H_2) whose abundance is determined by the balance between formation and dissociation rates under far-ultraviolet (FUV) background radiation (Draine & Bertoldi, 1996; Haiman et al., 1997; Dijkstra et al., 2008; Wolcott-Green et al., 2011; Johnson et al., 2013; Sugimura et al., 2014; Luo et al., 2019). The Pop. I I stars subsequently form at $z \sim 10$ and survive longer time than Pop. III because of the lower mass due to efficient metal cooling, and the old generation might be present in our Galaxy (Ricotti & Gnedin, 2005; Bovill & Ricotti, 2011a,b). In addition, the presence of old globular clusters whose ages are $\gtrsim 10\,{\rm Gyr}$ requires first galaxies to satisfy specific conditions for the formation of highly dense stellar clumps (Kravtsov & Gnedin, 2005; Brodie & Strader, 2006; Moore et al., 2006; Prieto & Gnedin, 2008; Kruijssen, 2015; Trenti et al., 2015; Ricotti et al., 2016; Kimm et al., 2016; Kim et al., 2018; Arata et al., 2018).

The radiative and SN feedbacks heat the surrounding gas to $\sim 10^{4}\,{\rm K}$ and $\sim 10^{7}\,{\rm K}$, respectively. Also, when gas falls into a DM halo, the gas collides with gas in outer side of the halo, and is heated up by shocks to the virial temperature $T_{\rm vir}$ which corresponds to the released gravitational energy. If gravitational potential of the DM halo is deep enough to retain the heated gas, the galaxy is possible to sustain the star formation due to cooling of that gas. Comparing gravitational energy to thermal one using a virial theory, we can estimate whether the heating process evacuates the gas from the halo:

$$T_{\rm vir} = \frac{\mu m_{\rm H} V_{\rm c}^2}{2 k_{\rm B}} \approx 10^4 \left(\frac{\mu}{0.6}\right) \left(\frac{M_{\rm h}}{10^8\,{\rm M}_{\odot}}\right)^{2/3} \left(\frac{\Delta_{\rm c}}{18\pi^2}\right)^{1/3} \left(\frac{1+z}{10}\right)\,{\rm K}, \tag{1.5}$$

where $m_{\rm H}$ is the mass of a hydrogen nucleus, $V_{\rm c}$ is the circular velocity and $k_{\rm B}$ is the Boltzmann constant. $M_{\rm h}$ is mass of the DM halo and $\Delta_{\rm c}$ is overdensity compared to the cosmic mean density. The hydrogen Lyman-α cooling becomes very efficient at $T \sim 10^{4}\,{\rm K}$, thus if the halo mass $M_{\rm h}$ exceeds $10^{8}\,{\rm M}_{\odot}$, the primordial gas in the halo can contract isothermally. Also if the gas is metal-enriched, the contraction proceeds with decreasing the gas temperature. In addition, state-of-the-art numerical calculations have shown that there is a significant fraction of infalling gas do not form shocks and efficiently supply cool gas ($T \sim 10^4$ K) to the central galaxy disks (Kereš et al., 2005, 2009; Dekel & Birnboim, 2006, 2008; Dekel et al., 2009; Agertz et al., 2011; Di Matteo et al., 2012; Nelson et al., 2013; Mandelker et al., 2016, 2018). This is because the gas is confined by cosmic filaments and the cooling time-scale is shorter than that of shock-heating. The cold mode significantly excites star formation in low-mass galaxies, which forms ionized bubbles and enhances Lyα emission by the recombination. This could be a good probe of very high-z galaxies ($z \gtrsim 10$, Dijkstra et al., 2007; Dijkstra & Loeb, 2009; Dijkstra & Wyithe, 2010; Zheng et al., 2010; Faucher-Giguère et al., 2010; Yajima et al., 2014b, 2015b, 2018). Thanks to the advancement of observational technologies, massive galaxies with $M_\star \sim 10^{10}\,\mathrm{M}_\odot$ in the reionization era ($z \gtrsim 6$) have been to be detected (see Section 1.3 for details). However, to investigate statistical properties of the first galaxies, we need observational data of less-massive galaxies.

Big projects for constructing the next generation telescopes are advancing; the James Webb Space Telescope (JWST)[4], the Wide Field Infrared Survey Telescope (WFIRST)[5], the Thirty Meter Telescope (TMT)[6], the European Extremely Large Telescope (E-ELT)[7] and so on. It is expected that deep surveys with these telescopes will reveal new insights into the first galaxies in early phase of the EoR ($z \gtrsim 10$). Therefore, theoretical predictions of the SED and the number density of observable sources are essentially needed. The robust predictions can be realized by more realistic cosmological simulations using massive parallel codes with supercomputers, which has been rapidly developed in the last two decades.

1.2 Observational Evidences of the Reionization

Here we briefly review observational evidences of the reionization.

Gunn–Peterson Effect

Gunn & Peterson (1965) originally predicted that if quasars existed before the end of reionization, photons with energies higher than Lyman-α line ($\lambda_\alpha = 1216$ Å) were absorbed by neutral IGM and created complete absorption troughs (GP effect). The

[4] https://www.jwst.nasa.gov/
[5] https://wfirst.gsfc.nasa.gov/
[6] https://www.tmt.org/
[7] https://www.eso.org/public/teles-instr/elt/

GP optical depth for Lyα photons is written as:

$$\begin{aligned}\tau_{\rm GP} &= \frac{\pi e^2}{m_e c} f_\alpha \lambda_\alpha H(z)^{-1} n_{\rm HI} \\ &= 4.9\times10^5 \left(\frac{\Omega_{\rm m}h^2}{0.13}\right)^{-1/2} \left(\frac{\Omega_{\rm b}h^2}{0.02}\right) \left(\frac{1+z}{7}\right)^{3/2} x_{\rm HI}, \end{aligned} \tag{1.6}$$

where f_α and λ_α are oscillation strength and wavelength of Lyα, and $H(z)$ is the Hubble constant at redshift z. In the right-hand side of the second equation, $\Omega_{\rm m}$ and $\Omega_{\rm b}$ are energy density parameters of matter and baryons, respectively, and h is related to the Hubble parameter $H = 100h$ km s^{-1} Mpc^{-1}. We here assume uniform IGM at high-redshift. This shows that a complete absorption trough should be created in the QSOs spectra even for $x_{\rm HI} \sim 10^{-4}$. The IGM absorption was first detected as the Lyα forest at $z < 5$ created by intervening H I clouds (e.g., Rauch, 1998). The *average* ionization fraction of IGM should be decided from thermal equilibrium between heating of UV background and cooling due to radiation and the cosmic expansion. The average ionization fraction was estimated from the spectra without the absorption trees.

The Sloan Digital Sky Survey (SDSS) [8] found ~ 50 QSOs at $z = 2-6.3$ (e.g., Fan et al., 2006). The complete absorption trough appeared in $z \gtrsim 6$ spectra ($\tau_{\rm GP} \gg 1$). With Lyα absorption only, it was difficult to determine whether the trough was created by accumulating Lyα forest clouds (smooth transition) or the end of the reionization (dramatic transition). The GP optical depth ($\tau \propto f\lambda$) for Lyβ and Lyγ is 6.2 and 17.9 times smaller than that of Lyα. When Lyα absorption is saturated, Lyβ can be used as a indicator of hydrogen ionization state. If Lyβ is also completely absorbed at the same redshift, one predicts rapid increase of neutral hydrogen. Fan et al. (2006) analyzed SDSS spectra of 19 QSOs, and found that the GP optical depth increased with redshift as $(1+z)^{4.3}$ at $z < 5.5$, and accelerated as $(1+z)^{>10}$ at $z > 5.5$ for both of Lyα and Lyβ, which they argued the end of the reionization. Note that, however, they also found significant scatters of optical depth at $z \lesssim 5.5$ as a function of directions of line of sights, which showed that there were residual neutral regions on a large scale (Becker et al., 2015).

Lyman-Alpha Emitters Luminosity Function

The number of and clustering of Lyman-α emitters (LAEs, see Sec. 1.3.2) depend on the cosmic mean ionization fraction (e.g., Dijkstra, 2014). Malhotra & Rhoads (2004) first adopted LAE luminosity function (LF) in the context of the reionization. They found that the number density of LAEs did not significantly change between

[8] https://www.sdss.org/

$z = 5.7$ and 6.6, which implied that gas was not fully neutral at $z \sim 6.5$. The number of LAE samples strongly increased by the Subaru/Suprim–Cam, and it has been shown that the LAE density (ρ_{LAE}) evolved as $(1+z)^{-5.0}$ at $z = 5.7 - 6.5$ and $(1+z)^{-20.8}$ at $z = 6.6 - 7.3$ with $> 90\,\%$ confidence (Konno et al., 2014). The accelerated decline was not seen in the UV-selected galaxies, thus not driven by simply decreasing the number of galaxies. Also, Lyα photons likely escape from higher-z galaxies because dust amount seems to be smaller. Therefore, the decreasing ρ_{LAE} with increasing redshift is certainly one of the evidence of the reionization. The quantitative constrain to the cosmic mean neutral fraction (x_{HI}) could be derived from comparing evolution of the LF with theoretical predictions that show how Lyα transmission changes with proceeding reionization. Using theoretical model of photo-ionization by McQuinn et al. (2007), Kashikawa et al. (2011) obtained $x_{\mathrm{HI}} \sim 0.4$ at $z = 6.5$.

CMB Photons

The CMB photons are produced in the last scattering surface at $z \approx 1100$, and can be re-scattered by free electrons in reionied and/or reionizing Universe. Thomson scattering creates the E-mode polarization, and with the analysis of cross-correlation with anisotropy of CMB temperature, one can obtain the optical depth τ. The 9-years observations of the Wilkinson Microwave Anisotropy Probe (WMAP) showed a value of $\tau = 0.088 \pm 0.014$, which corresponded to "instantaneous" reionization at $z \approx 10.5 \pm 1.1$ (Hinshaw et al., 2013). This might imply the reionization began at $z \sim 15$ or even earlier. However, the optical depth was updated to $\tau = 0.066 \pm 0.012$ by Planck Collaboration et al. (2016), corresponding to lower reionization redshift of $z \approx 8.8^{+1.2}_{-1.1}$. The Planck result reduced the need for significant star formation at $z > 10$.

If star-forming galaxies are main sources producing Lyman continuum photons (LyC; $h\nu \geq 13.6\,\mathrm{eV}$) in the reionization era, evolution of the star formation rate density (SFRD) would be used as an estimator of time-dependent cosmic ionization rate. Madau & Dickinson (2014) collected observed infrared and rest-UV LFs, and derived ρ_{SFR} as a function of redshift with a correction of empirical dust attenuation law (Calzetti et al., 1994, 2000; Meurer et al., 1999; Takeuchi et al., 2012). They showed that ρ_{SFR} peaked at $z \sim 2$ and rapidly declined with increasing redshift, but the evolution has been poorly constrained for $z \gtrsim 4$ because of the lack of observational data (see Figure 1.4c for reference). Using the Planck result as an additional condition for constraining $\rho_{\mathrm{SFR}}(z)$, Robertson et al. (2015) found that neutral fraction was decreased by star-forming galaxies at $z \approx 6 - 10$.

The analysis of the SFRD was based on the assumption of $f_{\rm esc}^{\rm LyC} = 0.2$, where $f_{\rm esc}^{\rm LyC}$ is escape fraction of LyC photons from galaxies. However, dependency of $f_{\rm esc}^{\rm LyC}$ on physical properties of the galaxies e.g., the halo mass, dust amount, covering fraction of neutral gas and redshift, has not fully understood yet (Wise & Cen, 2009; Yajima et al., 2011; Kimm & Cen, 2014; Paardekooper et al., 2015; Xu et al., 2016). Numerical studies also showed significant dependence on the spatial resolution (e.g., Ma et al., 2015). In addition, the cosmic neutral fraction is directly measured by intensity mapping of rest-frame 21-cm emission line (Furlanetto et al., 2004, 2006; Mellema et al., 2006; McQuinn et al., 2007; Morales & Wyithe, 2010; Kim et al., 2013; Yajima & Li, 2014). The size distribution of ionized bubbles could reflect the LyC LF. Upcoming the Square Kilometre Array (SKA) will be possible to newly constrain duration of the EoR.

1.3 Galaxy Populations at High-redshift

Owing to the development of observations, galaxies at $z > 6$ have been detected in multi-wavelength: rest-UV, dust continuum, Lyman-α line, and metal emission lines. These observations have revealed the wide variety of radiative properties of the first galaxies. The physical origin of the variety has not been understood yet. Here we briefly introduce galaxy populations at high-z. We use the apparent AB magnitude ($m_{\rm AB}$) that is defined as $m_{\rm AB} = -2.5 \log f_\nu - 48.60$, where $f_\nu = L_\nu / 4\pi d_{\rm L}^2$ is the observed flux in unit of erg s^{-1} cm^{-2} Hz^{-1}, and L_ν and $d_{\rm L}$ are the specific luminosity and the luminosity distance, respectively. The absolute magnitude (M) is defined as the apparent magnitude when the distance to the object is 10 pc, which represents intrinsic brightness without cosmological dimming.

1.3.1 Lyman-break Galaxies

High-z galaxies have been identified by Lyman-break technique (Steidel et al., 1999; Ouchi et al., 2004; Shapley, 2011). Without dust attenuation, star-forming galaxies generally have blue UV continuum spectra produced by young massive OB stars. Photons with shorter wavelengths than the Lyman-limit (912 Å) or Lyman-α (1216 Å) are absorbed by their interstellar medium (ISM) and IGM, which forms a sharp break in the spectrum at $\lambda = 1216 \times (1+z)$ Å for a redshift z galaxy (see Figure 1.4a). Thus, high-z galaxies have distinct rest-frame UV colors, and efficiently be selected by multi-band photometric imaging. Galaxies identified by this technique are called Lyman-break galaxies (LBGs). For example, the wavelength Lyman-α becomes $\sim 0.85\,\mu$m for a $z = 6$ galaxy in observer's frame, which would be dropout in optical i-band, but detectable in near-infrared z-band.

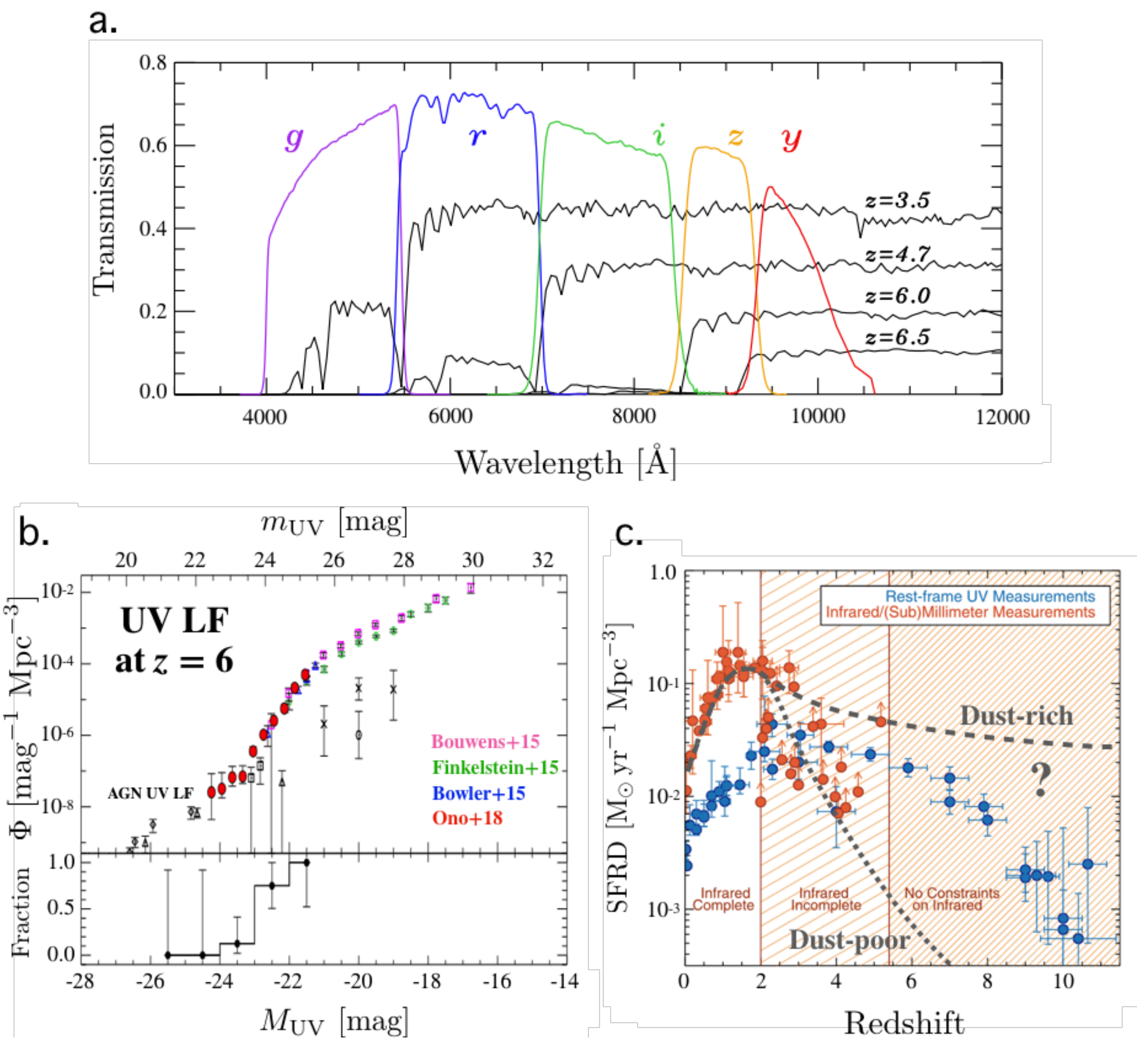

Figure 1.4: (a) Schematic picture for explaining the Lyman-break technique. Colored lines represent filters of the Subaru/Hyper Suprime–Cam (HSC). Black lines show example spectra of galaxies at $z = 3.5,\ 4.7,\ 6.0$ & 6.5 from Bruzual & Charlot (2003) library. **(b)** Observed UV luminosity function at $z = 6$. The bottom panel shows fraction of the number of observed galaxies by HSC. **(c)** Estimated history of the cosmic star formation density (SFRD). Blue points represent the measurements by rest-frame UV observations. Red points are for infrared and (sub-)millimeter observations. There is no constrains on infrared at $z \gtrsim 6$. If the high-z Universe is rich in dust, a significant fraction of star formation has been missed by the UV observations (dashed line). Alternatively, population of dust-obscured galaxies might be poor at high-z (dotted line). Panel (a) and (b) are altered from Ono et al. (2018), and panel (c) from Casey et al. (2018).

From early 2000s, the Hubble Space Telescope (HST)[9] made a breakthrough for high-z observations using the LBG technique. The HST was installed with Advanced Camera for Survey (ACS) and Near Infrared Camera and Multi-Object Spectrometer (NICMOS). Some big projects for constructing LBG catalogs have been conducted; The Great Observatories Origins Deep Survey (GOODS) program[10], in which the images of the Chandra Deep Field South (CDF-S) and Hubble Deep Field North (HDF-N) have been taken. The surveyed area was provided $\sim 320\,\mathrm{arcmin}^2$ to 5σ sensitivity limits of $m_{\mathrm{AB}} \sim 27$. The Hubble Ultra Deep Field (HUDF) program reached $m_{\mathrm{AB}} \sim 29$ over a $11.3\,\mathrm{arcmin}^2$ region of CDF-S field (Bouwens et al., 2006). By 2007, more than 600 LBGs at $z \sim 6$ were identified by multi-bands HST imaging. At the 2010s, deeper and wider field ($4.8\,\mathrm{arcmin}^2$) survey with HST has identified $z \sim 7-8$ galaxies (Bouwens et al., 2011). The depth of the HUDF imaging reached to $m_{\mathrm{AB}} = 29-30$ (eXtreme Deep Field; XDF), which corresponded to the UV absolute magnitude of $M_{\mathrm{UV}} \sim -17$ at $z \sim 7$ (Illingworth et al., 2013). The Cosmic Assembly Near-IR Deep Extragalactic Legacy Survey (CANDELS, Grogin et al., 2011) has been carried out to study a very wide field ($553\,\mathrm{arcmin}^2$ with the depth of $m_{\mathrm{AB}} = 26.6-26.8$). It succeeded to detect abundant UV sources with $-21 \lesssim M_{\mathrm{UV}} \lesssim -19$, which is close to the turning point of the broken power-law fit to the LF at $z \sim 6$ (Figure 1.4b). So far, the total number of LBGs in HST data are $300-500$ for $z \sim 7$ galaxies and $100-200$ for $z \sim 8$ galaxies (Bouwens et al., 2015; Finkelstein et al., 2015). The Subaru/Hyper Suprime–Cam (HSC)[11] has conducted a remarkably wide field survey ($> 100\,\mathrm{deg}^2$), and the number of LBG samples at $z \sim 4-7$ has increased to $\sim 500,000$ (Ono et al., 2018). Ultra-deep imaging ($m_{\mathrm{AB}} \sim 29$) of the Hubble Frontier Field (HFF) has also been advanced utilizing the magnification effect via gravitational lensing (Lotz et al., 2017). The final goal of this project is to constrain abundances of low luminosity (faint-end) galaxies at $z \sim 7-10$ (Kawamata et al., 2018).

1.3.2 Lyman-Alpha Emitters

Partridge & Peebles (1967) first suggested that Lyman-α line could be useful probe of high-z galaxies. Since the late of 1990s, surveys of the Lyman-α emitters (LAEs) have made considerable progress in understanding of early star-forming galaxies (e.g., Dey et al., 1998). Observed wavelength of Lyα for $z > 5$ objects is $> 7000\,\text{Å}$, and could be veiled by a forest of OH sky lines. This led to development of narrow band (NB) filters focusing on gaps of the OH forest, which corresponds to $z = 5.7,\ 6.5,\ 7.0$ and 7.3. The NB filters allowed us to conduct a survey of galaxies

[9]https://hubblesite.org/
[10]http://www.stsci.edu/science/goods/
[11]https://www.subarutelescope.org/

with $\gtrsim 1$ mag brighter Lyα line than UV continuum, corresponding to the equivalent width (EW) of ~ 20 Å. As wide-field CCD imaging cameras became more common for the ground-base telescopes, NB filters were more used. Early wide-field surveys succeeded to obtain LAE LF at $z \approx 4.5 - 6.5$ (Rhoads & Malhotra, 2001). The Subaru/Suprime–Cam which was installed two NB filters (NB816 and NB912 corresponding to $z = 5.7$ and 6.6) further proceeded LAE survey. The total number of identified LAEs by this campaign was ~ 700 (~ 300) at $z = 5.7$ (6.6), and the number of spectroscopically confirmed LAEs was 211 (91) (e.g., Kashikawa et al., 2006; Shimasaku et al., 2006; Ouchi et al., 2008, 2010). Recently, Subaru/HSC installed four NB filters further increased the number of $z \sim 4 - 7$ LAEs to $\sim 2,000$ (Inoue et al., 2018).

1.3.3 Sub-millimeter Galaxies and Metal-line Emitters

In general, UV observations could miss dust-enshrouded galaxies, and this population significantly contributes to the total SFRD (see Figure 1.4c, Casey et al., 2018). However, it is difficult to estimate the accurate abundance at high-z, because it is related to the complex physics of dust evolution (Weingartner & Draine, 2001; Todini & Ferrara, 2001; Inoue, 2003; Bianchi & Schneider, 2007; Nozawa et al., 2007; Kuo & Hirashita, 2012; Asano et al., 2013; McKinnon et al., 2016, 2018; Aoyama et al., 2017, 2018). The first detection of dust emission from $z > 6$ Universe is reported by Riechers et al. (2013), who showed that a galaxy at $z = 6.34$ had a large dust mass ($M_{\rm d} \sim 10^9\,{\rm M}_\odot$). The high-$z$ dust emission is observed in the sub-millimeter wavelength band on the ground. The emission comes from sub-mm galaxies (SMGs), whose SFRs are estimated to be quite high ($\gtrsim 1000\,{\rm M}_\odot\ {\rm yr}^{-1}$). The sensitivity for SMG detection has been dramatically improved with the ALMA. Using the gravitational lensing effect, Watson et al. (2015) reported detection of dust emission from a sub-$L_\star$ galaxy at $z = 7.5$. Laporte et al. (2017) detected dust emission from a higher-redshift galaxy ($z = 8.38$), which has been used to test the validity of theoretical models of dust evolution (Behrens et al., 2018; Liu & Hirashita, 2019). Also, merging massive galaxies (SFR $\sim 3000\,{\rm M}_\odot\ {\rm yr}^{-1}$) were found at $z = 6.9$ (Marrone et al., 2018), which required a theory of galaxy evolution that can explain the rapid growth. Detection of dust emission from high-z LBGs has been subsequently reported (Capak et al., 2015; Bouwens et al., 2015; Bowler et al., 2018; Hashimoto et al., 2019; Tamura et al., 2019).

Metal-lines of [O III] 88 μm and [C II] 158 μm are observed in sub-mm wavelengths in the observer's frame, and used as excellent probes of high-z galaxies with ALMA. The [C II] is a main coolant of warm neutral medium ($\sim 10^4$ K), which forms cold clumps via thermal instability (Arata et al., 2018). The clumps are gravitationally confined and become molecular clouds, and finally form stars. [O III] is emitted from the ionized regions formed by the massive stars. Thus, we can investigate the physical processes from gas to star formation using these metal-lines (Cormier et al., 2015). The [O III] line at $z > 6$ was first detected by Inoue et al. (2016). Other groups have also reported detection of the line (Carniani et al., 2017; Laporte et al., 2017; Marrone et al., 2018; Hashimoto et al., 2019; Tamura et al., 2019; Harikane et al., 2019), which led to the identification of the highest-redshift galaxy ($z = 9.11$, Hashimoto et al., 2018). For the [C II] line, some groups claimed the detection (Capak et al., 2015; Carniani et al., 2017; Marrone et al., 2018; Hashimoto et al., 2019; Harikane et al., 2019), while others reported null-detection (Ouchi et al., 2013; Inoue et al., 2016; Laporte et al., 2019). The upper limited [C II] luminosity is lower than expectation extrapolated from the local relation (De Looze et al., 2014). Harikane et al. (2018) showed that high-z LAEs had low $L_{[\mathrm{C\,II}]}$/SFR. This may imply the difference of chemical abundance between present and high-z galaxies.

1.4 This Thesis

Here we introduce relevant studies and clarify the motivation of our work. Researchers began to use numerical simulations and semi-analytical models in 1990s to study galaxy formation and evolution based on the hierarchical structure formation scenario in the ΛCDM Universe (Davis et al., 1985; White & Frenk, 1991; Cen & Ostriker, 1992; Kauffmann et al., 1993; Lacey & Cole, 1993; Katz et al., 1996; Kauffmann et al., 1999; Somerville & Kolatt, 1999). From 2000s, various physical models used in cosmological hydrodynamics simulations have been proposed; For example, star-formation (Mihos & Hernquist, 1994; Springel, 2000; Kravtsov, 2003; Schaye, 2004; Krumholz & McKee, 2005; Schaye & Dalla Vecchia, 2008; Gnedin & Kravtsov, 2011), and stellar and black-hole feedback models (Thacker & Couchman, 2001; Springel & Hernquist, 2003; Springel et al., 2005a; Stinson et al., 2006; Oppenheimer & Davé, 2006; Dalla Vecchia & Schaye, 2008; Booth & Schaye, 2009; Wiersma et al., 2009b; Choi & Nagamine, 2011; Dalla Vecchia & Schaye, 2012; Stinson et al., 2013; Hopkins et al., 2013; Kimm & Cen, 2014; Okamoto et al., 2014; Muratov et al., 2015; Shimizu et al., 2019), which have successfully reproduced the cosmic star formation history for tuned parameters (e.g. Springel et al., 2005b; Schaye et al., 2010, 2015; Vogelsberger et al., 2014; Hopkins et al., 2014, 2018; Pillepich et al., 2018).

Especially, numerical studies focusing on the formation mechanism of the first galaxies have made progress since the late of 2000s (Greif et al., 2008; Maio et al., 2011; Safranek-Shrader et al., 2012; Wise et al., 2012b,a; Johnson et al., 2013; Hopkins et al., 2014; Kimm & Cen, 2014; Yajima et al., 2015a,b; Paardekooper et al.,

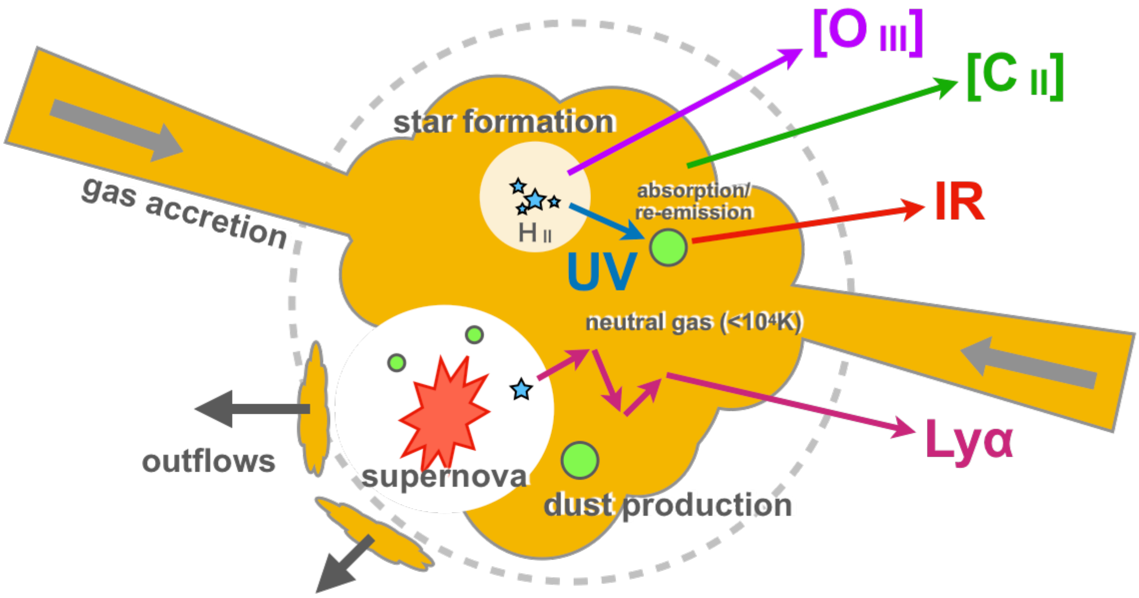

Figure 1.5: Schematic picture of the relation between galaxy evolution and radiative properties. Due to gravitational potential of a DM halo, gas accretes onto the central region and forms stars in local high-density regions. Massive stars explode as supernovae, which blow the surrounding gas as galactic outflows, and they also produce dust grains. The dusts play an important role in radiative transfer because they absorb UV light and re-emit infrared photons. Since Lyα is a resonant line, the photons are frequently scattered by neutral gas, and they finally escape from the system with frequencies different from Lyα. [O III] line is emitted from H II regions, while [C II] line is mainly emitted from H I regions as described below. Therefore the line ratio is directly related to the structure of the galaxy.

2015; Ricotti et al., 2016; Yajima et al., 2017b; Trebitsch et al., 2017; Kim et al., 2018). These studies revealed that stellar and supernova (SN) feedbacks are crucially important for high-z galaxy evolution. Kimm & Cen (2014) studied star formation in high-z dwarf galaxies using cosmological hydrodynamic simulations, and found that the star formation proceeds intermittently due to SN feedback and gas accretion. Also Yajima et al. (2017b) showed that the intermittent star formation occurs even in massive haloes ($M_{\rm h}|_{z=6} \sim 10^{11} - 10^{12}\,{\rm M}_{\odot}$) that corresponds to the host of observed LAEs and LBGs. This fact significantly affects physical properties of the first galaxies e.g., the galaxy sizes and DM concentrations. However, the radiative properties associated with the bursty star-formation history are not fully understood yet. **In this thesis, we focus on the radiative output of the first galaxies by carrying out radiative transfer calculations in post-processing of cosmological hydrodynamic simulations.** Our method can reproduce all of the complex physics that relates to the galactic radiative properties (see Figure 1.5).

There were earlier works studying the radiative properties of the first galaxies with similar methodologies. Yajima et al. (2015a) found that simulated galaxies in 5σ overdense regions were heavily obscured by dust, and bright at infrared wavelengths. Wilkins et al. (2016) investigated the statistical nature of the first galaxies using galaxy samples in a large cosmological volume, and successfully reproduced the observed UV LF and the stellar mass function. They showed that the stellar radiation from massive galaxies suffered from dust extinction even at $z \sim 8$. These previous studies suggest that first galaxies smoothly evolved into dusty star-burst galaxies as their halo mass increases. Even for very high-z galaxies ($z \sim 15$), dust extinction can reduce the observability with JWST (Barrow et al., 2018).

The metal-line emission of high-z galaxies has also been studied. Combining cosmological simulations and analytical models for multi-phase ISM, Nagamine et al. (2006) predicted the ALMA observability of [C II] line emission from star-forming galaxies at $z = 3-6$. Vallini et al. (2015) studied contributions of various gas phases to total [C II] luminosity. The CMB photons have high temperature ($T_{\rm CMB} \sim 20\,{\rm K}$) at $z \gtrsim 6$, which can increase the electron temperature due to Thomson scattering. They found that the heating of cold gas by CMB photons significantly suppressed the contribution from the cold neutral medium. Pallottini et al. (2017) focused on properties of LBGs at $z \sim 6$. They used zoom-in simulations, and found that H_2 galactic disks mainly contributed to total [C II] luminosity (see also, Pallottini et al., 2019). Using large-scale semi-analytic simulations, Lagache et al. (2018) succeeded to reproduce observed SFR-$L_{[{\rm C_{II}}]}$ relations. Moriwaki et al. (2018) studied observability of [O III] emitters at $z \sim 8$ with $(50\,{\rm Mpc})^3$ simulation box and sub-grid modeling for capturing ionized structures. Also Katz et al. (2019) studied various metal emission lines at $z \gtrsim 9$ using zoom-in radiative hydrodynamics simulations and a massive emissivity table (Cloudy, Ferland et al., 1998). They predicted a kpc-scale offset between [O III] and [C II] emitting regions. However, their galaxy sample was limited because of the expensive numerical costs. **We conduct more than 10 high-resolution simulations and investigate statistical trends of multi-wavelength radiative properties.**

The state-of-the-art simulations with SN feedback models showed that star formation activity and gas structures change rapidly on short time-scales due to galactic outflows (Kimm & Cen, 2014; Hopkins et al., 2014; Davis et al., 2014; Muratov et al., 2015; Yajima et al., 2017b). Thus, strong outflows are likely to change the radiative properties of galaxies as well. However, it has not been understood well how intense starbursts affect the relationship between the radiative properties and galaxy evolution. Ma et al. (2015) used high-resolution cosmological simulations, and showed that the escape fraction of ionizing photons in less-massive galaxies

($M_{\rm h} \sim 10^9 - 10^{11}\,{\rm M_\odot}$) was significantly affected by intermittent star formation (see also, Paardekooper et al., 2015). Despite progress in our understanding on feedback, the radiative properties of massive galaxies are still unclear. **We focus on the radiative properties of massive galaxies that repeat short starbursts and investigate the origin of the observational varieties.**

In order to study the radiative properties, we need to capture spatial distribution of dusts and stars. As galaxies evolve, dusts and metals are produced by Type-II SNe[12]. When the interstellar dust in high-z galaxies absorbs the stellar UV radiation and re-emits the energy in infrared, the galaxies could be bright in the sub-mm wavelength. In contrast, if the dust absorption is ineffective, the star-forming galaxies are bright in the rest-frame UV wavelength and become targets for HST, Subaru and Keck telescopes. To capture the covering fraction of dust over the stars, we use three-dimensional hydrodynamic simulations.

Dust attenuation sensitively depends on the dust abundance, size distribution and spatial distribution. However, observational data of dust emission from high-z galaxies are quite limited. Theoretical predictions of dust properties can give important insights. For example, Todini & Ferrara (2001) theoretically studied the dust compositions (amorphous carbon, Fe_3O_4, Mg_2SiO_4 and so on) and size distributions by taking account of the dust growth via nucleation and accretion processes in Type-II supernova shocks (see also, Nozawa et al., 2007). Asano et al. (2013) evaluated the dust properties using phenomenological models that involved dust formation and destruction processes in combination with star formation histories in galaxies. Yajima et al. (2014a) carried out radiative transfer calculations in cosmological simulations, and estimated the typical dust size by comparing the colors of simulated galaxies with observations. Cullen et al. (2017) examined the dust attenuation law by matching the UV LF and slope of the UV continuum spectra (β) of simulated galaxies, and showed that the Calzetti law is actually the best description rather than the SMC law (see also Cullen et al., 2018). Narayanan et al. (2018b) used consmological simulations at $z = 0 - 6$, and showed that the dust extinction curve had a large dispersion due to the inhomogeneous spatial distribution of dust in star-forming galaxies. In addition, Behrens et al. (2018) studied dust abundances in an observed SMG at $z = 8.38$ (Laporte et al., 2017) using high-resolution simula-

[12] AGB stars also produce dust. However, the evolution of low-mass stars toward the AGB phase takes longer than 1 Gyr. Thus, SNe dominate the dust enrichment of first galaxies, which occurs at the end of the lifetimes of massive stars ($\lesssim 10$ Myr). The pair-instability SNe are also important in the early universe (e.g. Nozawa et al., 2007), but for evolved galaxies Type-II SNe dominate the dust production. For example, Maiolino et al. (2004) showed that the extinction curves of $z \sim 6$ quasars agree with the Type-II SN model.

tions. In the present work, we study the sub-mm fluxes from more massive galaxies with bursty star formation histories and the impact of stellar feedback on the radiative properties of first galaxies at $z \gtrsim 6$ using cosmological zoom-in hydrodynamic simulations.

In addition to the SED of galaxies, the sizes of galaxies at UV and [C II] wavelengths are likely to change as galaxies evolve. Galaxy sizes have a large impact on the observational estimation of the faint-end slope of UV luminosity function, because of surface brightness dimming[13] and observational limits (Grazian et al., 2011). As we discuss in this paper, the morphology and the size of a galactic disk is significantly dependent on the feedback strength at high-z, and if the extended low-mass galaxies are missed in current HFF observations, the cosmic SFRD could be significantly underestimated at $z \gtrsim 6$ (e.g. Jaacks et al., 2012a). The low-mass galaxies studied in this paper are mainly satellites of massive galaxies at $z \gtrsim 6$, and separate zoom simulations of low-density regions will have to be performed in the future to examine the low-mass galaxies in the field regions. Anyway, **we investigate the galaxy sizes as well as the SEDs by radiative transfer calculations, and find an interesting transition between UV and sub-mm bright phases due to intermittent starburst and its feedback.** These fluctuations may affect the estimate of luminosity functions as we will discuss in Sec. 3.3.1, and we quantify the duty cycle of such fluctuations.

This paper is organized as follows. We describe our models of cosmological hydrodynamic simulations with a zoom-in technique and multi-wavelength radiative transfer calculations in Section 2.1 & 2.2, respectively. From Section 3.1, we explain our simulation results. We first present projected images of gas distributions and intensity maps. In Section 3.3, we focus on the redshift evolution of our fiducial galaxy and describe how the radiative properties changes with a bursty star formation history. We statistically compare the simulation results with recent observations in Section 3.4, where we investigate the observability with ALMA and

[13] The observed surface brightness decreases as $\propto (1+z)^{-4}$ due to cosmological expansion. Let us consider emission sources in a volume of ℓ^3 with the density of n and the luminosity of each source is L, observed flux becomes $F = Ln\ell^3/(4\pi d_{\rm L}^2)$, where $d_{\rm L}$ is the luminosity distance. Also if the solid angle of the volume is $\delta\Omega$, observed surface brightness is $S = F/\delta\Omega$. The solid angle can be rewritten as $\delta\Omega = \delta\theta^2$, where $\delta\theta = \ell/d_{\rm A}$ and $d_{\rm A}$ is the angular diameter distance. Thus, the surface brightness becomes

$$S = \frac{Ln\ell^3}{4\pi d_{\rm L}^2}\frac{d_{\rm A}^2}{\ell^2} = \frac{Ln\ell}{4\pi}\frac{d_{\rm A}^2}{d_{\rm L}^2} = \frac{Ln\ell}{4\pi}\frac{1}{(1+z)^4} \propto (1+z)^{-4}.$$

This includes the effects of extending solid angle of the object ($(1+z)^{-2}$), increasing wavelength with cosmic expansion ($(1+z)^{-1}$) and stretching time interval of emission ($(1+z)^{-1}$).

the physical origin of the observational relation between the metal-line luminosity ratio and the star formation rate. In Section 3.5, we study dust properties at high-z. In Section 3.6, we discuss the sizes of galaxies in UV and [C II] wavelengths. We find that the compactness of galaxies induces dust heating by absorption of stellar radiation. Finally, we summarise our findings in Chapter 4.

Chapter 2

Basic Methodologies

2.1 Cosmological Hydrodynamic Simulations

2.1.1 Simulation Code and Initial Conditions

We use the smoothed particle hydrodynamics (SPH) simulation code Gadget-3 (Springel et al., 2005b). In SPH, the fluid dynamics is approximated by motions of discrete particles, and physical quantities are computed from kernel interpolation. One of the advantage of SPH is that the spacial resolution automatically becomes higher in denser regions, thus it is available for cosmological simulations that have strong density contrasts i.e., the clusters and voids. Our code first calculates the local density at the position of particle i,

$$\rho_i = \sum_j m_j W_{ij}(h), \tag{2.1}$$

where m_j is the mass of particle j, and $W_{ij}(h) = W(|\boldsymbol{r}_i - \boldsymbol{r}_j|, h)$ is a cubic-spline kernel function. h is the size of the kernel function and corresponds to the spatial resolution, so-called the smoothing length. The equation of motion is approximated as

$$\frac{d^2\boldsymbol{r}_i}{dt^2} = -\sum_j m_j \left(\frac{P_i}{\rho_i^2} + \frac{P_j}{\rho_j^2} \right) \nabla W_{ij}(h), \tag{2.2}$$

where t is time and P is pressure. The energy equation is also calculated as

$$\frac{du_i}{dt} = \frac{P_i}{\rho_i^2} \sum_j m_j \boldsymbol{v}_{ij} \cdot \nabla W_{ij}(h), \tag{2.3}$$

where u is the internal energy, and $\boldsymbol{v}_{ij} = \boldsymbol{v}_i - \boldsymbol{v}_j$. When we consider an additional cooling process e.g., radiative cooling, the term is added in the right hand side. These fluid equations are closed by the equation of state,

$$P = (\gamma - 1)\rho u, \tag{2.4}$$

where γ is the specific heat ratio, which is set to $5/3$ because the diffuse gas in our interests can be treated as an ideal gas. Our code employs the variable kernel size h which is determined iteratively with ρ, imposing a condition that the number of neighbor particles is kept in a fixed range $N_{\rm ngb} \sim 48$. In this case, $\nabla W_{ij}(h_i)$ in above equations is simply replaced by $\nabla \widetilde{W_{ij}} = 0.5[\nabla W_{ij}(h_i) + \nabla W_{ij}(h_j)]$.

Our code implements the sub-grid models developed in the *Overwhelming Large Simulations* (OWLS) project (Schaye et al., 2010) and *First billion Years* (FiBY) project (Johnson et al., 2013) e.g., formation of Pop. III/Pop. II stars, SN energy feedback, chemical enrichment, non-equilibrium primordial chemistry and dust formation/destruction processes. It has successfully reproduced statistical properties of high-z galaxies e.g., the UV luminosity function corrected by dust absorption (Cullen et al., 2017) and evolution of SFRD at $z \gtrsim 10$ (Johnson et al., 2013). In this work, we do not use Pop. III star formation and non-equilibrium primordial chemistry because our focus is on more massive evolved galaxies, not on early dwarf galaxies. We use cosmological parameters of $\Omega_{\rm m} = 0.3$, $\Omega_{\rm b} = 0.045$, $\Omega_\Lambda = 0.7$, $n_{\rm s} = 0.965$, $\sigma_8 = 0.82$ and $h = 0.7$ (Planck Collaboration et al., 2016).

We focus on massive haloes studied by Yajima et al. (2017b) whose masses are $\sim 10^{11}\,{\rm M_\odot}$ (Halo-11) and $\sim 10^{12}\,{\rm M_\odot}$ (Halo-12) at $z = 6$ as *fiducial* runs. To study statistical trends, we increase simulation samples with the same set-up of Yajima et al. (2017b). Here we briefly explain our models. Since massive haloes are very rare at high-z, we need to use large-scale simulations for identifying these haloes. For example, the number density of $M_{\rm h} \sim 10^{12}\,{\rm M_\odot}$ haloes at $z \sim 6$ is $dn/d\ln M \sim 10^{-5}\,{\rm Mpc^{-3}}$ in the comoving unit (Press & Schechter, 1974; Sheth & Tormen, 2002; Li et al., 2007), thus simulations with $(100\,h^{-1}{\rm Mpc})^3$ boxes could create ~ 10 such massive haloes. We first conduct the N-body simulations in comoving $(20\,h^{-1}{\rm Mpc})^3$ and $(100\,h^{-1}{\rm Mpc})^3$ boxes until $z = 6.0$. We make the initial conditions using the Music code (Hahn & Abel, 2011). The Lagrangian perturbation theory describes the evolution of density perturbation in the rest-frame of the fluid. The position and velocity vector of a particle at the time of t is written as

$$\boldsymbol{x}(t) = \boldsymbol{q} + \boldsymbol{L}(\boldsymbol{q}, t), \qquad \boldsymbol{v} = \frac{d}{dt}\boldsymbol{L}(\boldsymbol{q}, t), \tag{2.5}$$

where $\boldsymbol{q}$ is its initial position, which represents the initial over-density field δ. The δ is assumed to be the Gaussian distribution function, which is well constrained by observations. Since a density perturbation grows following a linear transformation, the Gaussianity is kept during the evolution in the linear regime. The Fourier-transformed over-density $\tilde{\delta}_k$ is linked to the power spectrum $P(k) = \langle \tilde{\delta}_k\ \tilde{\delta}_k^* \rangle = \alpha k^{n_s} T^2(k)$, where α is a normalization coefficient, n_s is the spectral index just after the inflation, and $T(k)$ is a transfer function (Eisenstein & Hu, 1998). $\boldsymbol{L}(\boldsymbol{q}, t)$

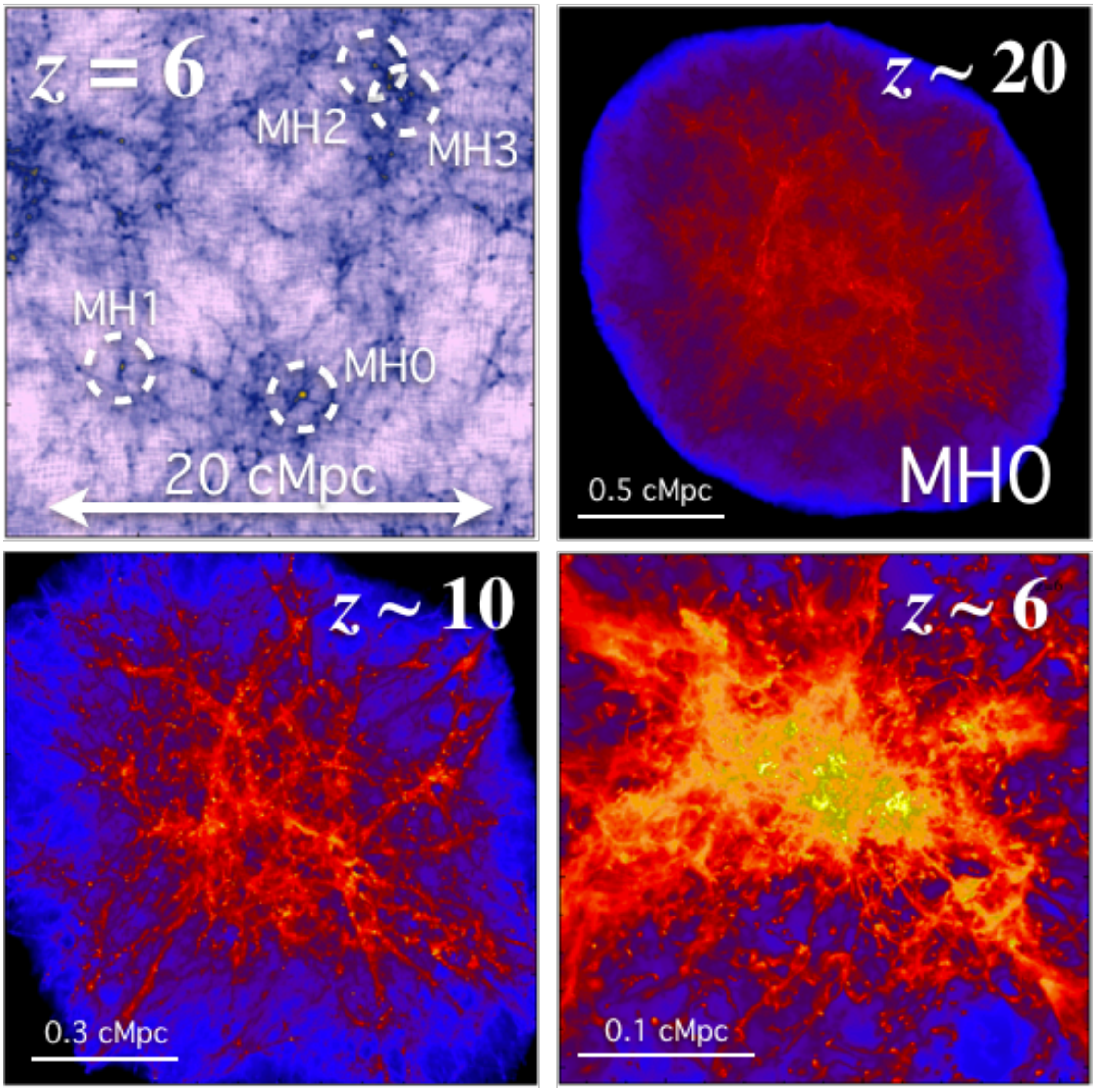

Figure 2.1: Simulation images. The top left panel shows the result of a N-body simulation in (20 comoving Mpc)^3 box until $z = 6$, and white dashed circles represent the positions of identified most massive haloes. The other three panels show gas surface density in the zoom region of the MHalo-0 run at $z \sim 20$, 10 & 6. The bottom left bar in each panel shows the spatial scale.

represents the 'displacement' field which is derived from the perturbation theory (c.f. Zel'Dovich, 1970),

$$\boldsymbol{L}(\boldsymbol{q},t) = -\frac{2}{3H_0^2 a^2 D_+(t)} \boldsymbol{\nabla}_{\boldsymbol{q}} \Phi(\boldsymbol{q},t), \tag{2.6}$$

where $D_+(t)$ is the linear growth factor which depends on the cosmological parameters, $D_+ \propto H \int_0^a (1/a^3 H^3) da$, where H is the Hubble parameter at the time of t (Eq. 1.2). Φ is the gravitational potential which follows Poisson's equation,

$$\boldsymbol{\Delta}_{\boldsymbol{q}} \Phi(\boldsymbol{q},t) = \frac{3}{2} H_0^2 a^2 \delta(\boldsymbol{q},t). \tag{2.7}$$

Note that the Gaussian over-density field δ is the source field of the displacements.

Through these procedures, we conduct N-body simulations and identify four most massive haloes with the friends-of-friends method. We call them medium-mass-halo-(MHalo-)0, 1, 2, 3 and large-mass-halo-(LHalo-)0, 1, 2, 3, respectively (see Table 2.1). Next we make a zoom-in initial condition for each halo. For MHaloes, the effective resolution is 2048^3 (the mass resolution of DM particles is $6.6 \times 10^4\,h^{-1}\mathrm{M}_\odot$) and the scale of the zoom-in region is comoving $\sim 1\,h^{-1}$Mpc. For LHaloes, the effective resolution is 4096^3 ($m_{\mathrm{DM}} = 1.1 \times 10^6\,h^{-1}\mathrm{M}_\odot$) and the zoom-in region is $\sim 8\,h^{-1}$Mpc. We then conduct cosmological hydrodynamic simulations until $z = 6.0$.

Figure 2.1 shows an example picture of our zoom-in simulations. Gas in the zoom region gravitationally contracts with decreasing redshift and forms filamentaly structures (red color). As described below, star formation occurs in the high-density knots (yellow color). Table 2.1 summarises properties of the runs. We set the gravitational softening length of $200\,h^{-1}$pc in the comoving scale, and the minimum smoothing length of $20\,h^{-1}$pc. This corresponds to the resolution of $\lesssim 10$ pc in physical scale at $z \sim 10$, which allows us to resolve internal gas structure of galaxies.

Figure 2.2 shows halo masses as a function of redshift. We observe differences in the growth rates between Halo-12 and LHaloes. We ascribe it to their environments, which can be quantified by the mass overdensity $\delta \equiv \rho/\rho_{\mathrm{crit}}$ at $z = 10$ within a sphere of radius 1 cMpc centered on each halo: $\delta = 2.02$ (for Halo-12), and $\delta = 3.12, 2.50, 2.29$ and 2.20 for LHalo-0, 1, 2 and 3, respectively. From these values, it is evident that LHaloes live in more dense environments than Halo-12, which results in earlier growth of halo masses. At $z \sim 6$, Halo-12 catches up with LHaloes and achieves an intermediate halo mass among them. These massive haloes are thought as hosts of observed LAEs and LBGs at $z \gtrsim 6$ (Ouchi et al., 2010).

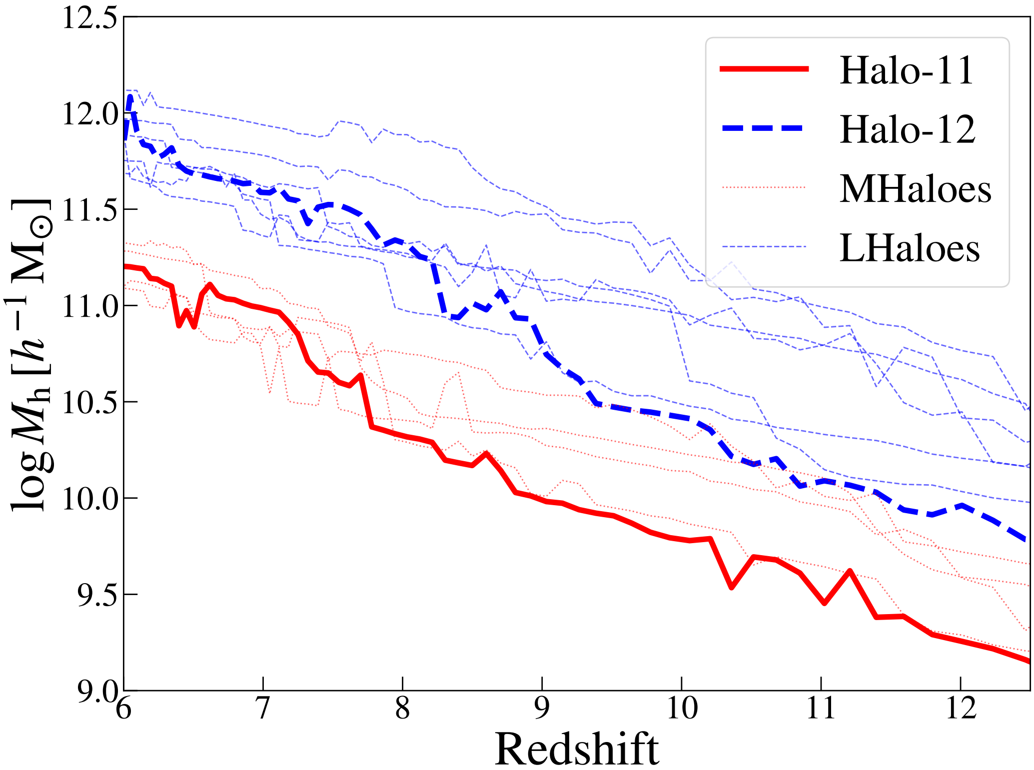

Figure 2.2: Mass growth of the DM haloes identified by the friends-of-friends method. The thick red and blue lines represent evolution of Halo-11 and Halo-12, respectively. The thin red and blues lines are for MHaloes ($M_{\rm h}|_{z=6} \sim 10^{11}\,{\rm M_\odot}$) and LHaloes ($M_{\rm h}|_{z=6} \sim 10^{12}\,{\rm M_\odot}$). The detailed properties of each halo are described in Table 2.1.

2.1.2 Star Formation Model

In our star formation model (Schaye & Dalla Vecchia, 2008), stellar particles are formed at high gas density regions, which represent star clusters with the masses of $m_\star \sim 10^4\,{\rm M_\odot}$. The stellar mass distribution in a particle at the formation time is assumed to follow the Chabrier initial mass function (Chabrier, 2003). The rate of SN feedback and chemical enrichment from evolving stars are computed from the age and metallicity of each particles (see Section 2.1.3 and 2.1.4). We set a free parameter of $n_{\rm H,th} = 10\,{\rm cm^{-3}}$, where $n_{\rm H,th}$ is the threshold density of hydrogen nuclei above which the gas particles follow the effective equation of state for the self-gravitating gas ($\gamma_{\rm eff} = 4/3$), and are converted their masses into the stellar particles. As described later, this threshold density satisfies the condition for evaluating the escape fraction of ionizing photons (Ma et al., 2015). The local star formation rate is estimated as:

$$\dot{m}_\star = A(1\,{\rm M_\odot}\ {\rm pc}^{-2})^{-n} m_{\rm g} \left(\frac{\gamma}{G} f_{\rm g} P_{\rm tot}\right)^{(n-1)/2}, \qquad (2.8)$$

where $m_{\rm g}$ is the mass of a gas particle, γ is the heat capacity ratio, and $P_{\rm tot}$ is total (thermal and turbulent) ISM pressure. $f_{\rm g}$ is the gas mass fraction in a self-gravitating galactic disk, which we set to unity because our target is the star-less and gas-rich galaxies at high-z. In addition, this star formation model is based on an empirical relation between gas surface density ($\Sigma_{\rm g}$) and surface SFR density ($\dot{\Sigma}_\star$), so-called the Kennicutt–Schmidt law (Kennicutt, 1998):

$$\dot{\Sigma}_\star = A \left(\frac{\Sigma_{\rm g}}{1\,{\rm M_\odot\ pc^{-2}}} \right)^n. \tag{2.9}$$

The best-fit parameters for local galaxies are $A_{\rm loc} = 2.5 \times 10^{-4}\,{\rm M_\odot\ yr^{-1}\ kpc^{-2}}$, and $n = 1.4$ in case of the Chabrier initial mass function. Schaye et al. (2010) succeeded to reproduce observed SFRD in their simulations with this model. However, recent observations showed that the coefficient of A in merging or high-z galaxies is significantly higher than local one (Genzel et al., 2010; Tacconi et al., 2013). Thus we use $A_{\rm fid} = 2.5 \times 10^{-3}\,{\rm M_\odot\ yr^{-1}\ kpc^{-2}}$ as a fiducial case. To clarify dependence of our results on star formation model, we also compute the case of $A_{\rm loc}$ which is indicated as 'low-SF' in Tab 2.1.

2.1.3 Chemical Enrichment and Radiative Cooling

Our simulation tracks the abundances of 9 elements (H, He, C, N, O, Ne, Mg, Si and Fe) for each particle separately, which are used for estimating the radiative cooling rate (Wiersma et al., 2009a,b). The mass ejection from a stellar particle during the time of $(t, t + \Delta t)$ is

$$\Delta m_\star = m_{\star,0} \int_{M_Z(t-t_\star+\Delta t)}^{M_Z(t-t_\star)} \Phi(M) m_{\rm ej}(M, Z) dM, \tag{2.10}$$

where $m_{\star,0}$ is the initial mass of the stellar particle, $t_\star$ represents the formation time, $\Phi(M) = dN/dM$ is the initial mass function, and $m_{\rm ej}(M, Z)$ is the ejected mass from a star with the mass of M and metallicity Z. $[M_Z(t-t_\star), M_Z(t-t_\star+\Delta t)]$ represents the mass range of stars which eject their masses during the time interval. The sources of chemical enrichment are Type-II/Ia SNe and AGB stars, and the ejected mass of each element is computed as

$$m_{\rm j,ej} = m_{\rm j,0:ej} + m_{\rm j,p:ej}, \tag{2.11}$$

where j runs over the 9 elements, and $m_{\rm j,0:ej}$ is the initial mass of j-th element in the star, which is inherited from the progenitor gas particle. $m_{\rm j,p:ej}$ is the ejected mass of j-th element created in the stellar interior, which is tabled by the models of stellar evolution and nucleosynthesis (Portinari et al., 1998; Marigo, 2001). Note that $m_{\rm j,p:ej}$ can be minus when the element is converted into heavier one. Each stellar particle increases the mass fraction of j-th element of neighbor gas particles in every time-steps, with the weight of

$$w_k = \frac{\frac{m_k}{\rho_k} W(r_k, h)}{\Sigma_i \frac{m_i}{\rho_i} W(r_i, h)}, \tag{2.12}$$

where m_k and ρ_k are the mass and mass density of k-th gas particle, thus m_k/ρ_k represents the volume. r_k is the distance from the stellar particle. Thanks for the volume-weighting method, the anisotopic enrichment of heavy elements is relatively avoided (see Wiersma et al., 2009b). The radiative cooling rate per unit volume for each gas particle is determined from the chemical abundances,

$$\Lambda = \Lambda_{\rm H,He} + \sum_{i>{\rm He}} \frac{n_i/n_{\rm H}}{(n_i/n_{\rm H})_\odot} \Lambda_{i,\odot}, \tag{2.13}$$

where $\Lambda_{\rm H,He}$ is the cooling rate by H and He, and n_i is the abundance of i-th element. $\Lambda_{i,\odot}$ is the cooling rate of i-th element with the solar abundance, which is tabulated by the Cloudy calculations (Ferland et al., 1998) under the UV background radiation spectrum at $z = 0$ (Haardt & Madau, 2001). The chemical abundances in $z \gtrsim 6$ galaxies are dominated by Type-II SNe, because low- and intermediate-mass stars take $\sim 10^9$ yrs to enter the AGB phases. However, as we will show later, the contribution from AGB stars becomes important for a part of the abundance ratio, such as O/C. In this paper, we consider all of the above chemical sources in our calculations of metal line luminosities (Sec. 2.3).

2.1.4 Supernova feedback

The SN feedback injects thermal energy into neighbor gas particles stochastically (Dalla Vecchia & Schaye, 2012), and the gas temperature increases to $10^{7.5}$ K. The thermal energy is efficiently converted into the kinetic energy against radiative cooling if the gas density is lower than the critical value,

$$n_{\rm H} \sim 100\,{\rm cm}^{-3} \left(\frac{T}{10^{7.5}\,{\rm K}}\right) \left(\frac{m_{\rm g}}{10^4\,{\rm M}_\odot}\right)^{-1/2}. \tag{2.14}$$

The numerical resolution of our simulations is sufficiently high to capture galactic winds and suppresses star formation. We describe more details of this feedback model in Appendix A.3. To investigate the effect of SNe clearly, we further perform simulations without SN energy injection, which is indicated as 'no-SN' in Table 2.1.

Halo ID	$M_{\rm h}$ [h^{-1} M$_\odot$]	$m_{\rm DM}$ [h^{-1} M$_\odot$]	$m_{\rm gas}$ [h^{-1} M$_\odot$]	SNe feedback	A	δ	M_{1500} [mag]
Halo-11	1.6×10^{11}	6.6×10^{4}	1.2×10^{4}	ON	2.5×10^{-3}	1.52	-20.3
Halo-12	6.9×10^{11}	1.1×10^{6}	1.8×10^{5}	ON	2.5×10^{-3}	2.02	-22.1
MHalo-0	2.1×10^{11}	6.6×10^{4}	1.2×10^{4}	ON	2.5×10^{-3}	1.54	-20.4
MHalo-1	1.9×10^{11}	6.6×10^{4}	1.2×10^{4}	ON	2.5×10^{-3}	1.48	-20.4
MHalo-2	1.3×10^{11}	6.6×10^{4}	1.2×10^{4}	ON	2.5×10^{-3}	1.66	-20.2
MHalo-3	1.2×10^{11}	6.6×10^{4}	1.2×10^{4}	ON	2.5×10^{-3}	1.58	-20.3
LHalo-0	1.3×10^{12}	1.0×10^{6}	1.8×10^{5}	ON	2.5×10^{-3}	3.12	-23.2
LHalo-1	9.3×10^{11}	1.0×10^{6}	1.8×10^{5}	ON	2.5×10^{-3}	2.50	-22.5
LHalo-2	7.9×10^{11}	1.0×10^{6}	1.8×10^{5}	ON	2.5×10^{-3}	2.29	-22.0
LHalo-3	5.7×10^{11}	1.0×10^{6}	1.8×10^{5}	ON	2.5×10^{-3}	2.20	-21.0
LHalo-4	8.0×10^{11}	1.0×10^{6}	1.8×10^{5}	ON	2.5×10^{-3}	2.19	-20.3
LHalo-5	4.9×10^{11}	1.0×10^{6}	1.8×10^{5}	ON	2.5×10^{-3}	2.09	-21.2
Halo-11-lowSF	1.5×10^{11}	6.6×10^{4}	1.2×10^{4}	ON	2.5×10^{-4}	1.52	-19.5
Halo-11-noSN	1.6×10^{11}	6.6×10^{4}	1.2×10^{4}	OFF	2.5×10^{-3}	1.52	-21.0
Halo-12-lowSF	8.0×10^{11}	1.1×10^{6}	1.8×10^{5}	ON	2.5×10^{-4}	2.02	-21.7
Halo-12-noSN	6.5×10^{11}	1.1×10^{6}	1.8×10^{5}	OFF	2.5×10^{-3}	2.02	-22.4

Table 2.1: Parameters of our zoom-in cosmological hydrodynamic simulations: (1) $M_{\rm h}$ is the halo mass identified by the friends-of-friends method for dark matter particles at $z = 6.0$. (2) $m_{\rm DM}$ is the mass of a dark matter particle. (3) $m_{\rm gas}$ is the initial mass of a gas particle. (4) A is the amplitude factor in the star formation model based on the Kennicutt–Schmidt law (Schaye & Dalla Vecchia, 2008). The Halo-11-lowSF and Halo-12-lowSF runs have a lower star formation amplitude factor. The Halo-11-noSN and Halo-12-noSN runs have no SN feedback. (5) $\delta \equiv \rho/\rho_{\rm crit}$ is the mass overdensity at $z = 10$ within a sphere of radius 1 cMpc centered on the halo. (6) M_{1500} is the absolute magnitude at $z = 6.0$ in rest-frame 1500 Å, obtained from radiative transfer.

2.2 Radiative Transfer Calculations

To obtain multi-wavelength properties of simulated galaxies, we use a radiative transfer code: the All-wavelength Radiative Transfer with Adaptive Refinement Trees (ART^2, Li et al., 2008; Yajima et al., 2012a). Here we briefly explain the code.

This code is based on the Monte Carlo technique. It tracks propagation of photon packets emitted by stellar particles. The intrinsic SEDs are calculated by the STARBURST99 as a function of the stellar age and metallicity (Leitherer et al., 1999). We assume the Chabier IMF with the mass range of $0.1 - 100\,\mathrm{M}_\odot$. In this paper, the number of photon packets is set to 10^6, which is sufficient to achieve convergence. As an advantage of ART^2, it makes adaptive refinement grids based on the SPH gas structure. It initially constructs a 4^3 base-grid over two times the virial radius of a halo, and if the number of SPH particles in a cell is greater than 16, the grid is further refined by 2^3 cells. Figure 2.3 shows an example of this refinement. We set the maximum refinement level to 12. For Halo-11 at $z = 6$, the minimum scale achieves $2.7\,h^{-1}$ pc, which matches the minimum smoothing length.

Even in the current resolution, it is difficult to resolve the multi-phase ISM accurately. The thermal instability [1] is one of main processes to form multi-phase ISM (Field, 1965; McKee & Ostriker, 1977). Simulating isolated low-metallicity galaxy mergers at $z \sim 10$, Arata et al. (2018) found that the spatial resolution of $\lesssim 0.01$ pc was required to follow the formation of dense cold clumps, which is still difficult to achieve even for the state-of-the-art cosmological zoom simulations. Therefore, ART^2 has the 'two-phase mode', which allows to calculate the radiative transfer with a subgrid multi-phase ISM model based on Springel & Hernquist (2003). It uses the smoothed values over SPH particles within a cell, and computes the physical properties of the cold phase within the hot phase, such as density and volume filling factor, assuming pressure equilibrium. We assume that the cold phase consists of randomly distributed molecular clouds which follow the power-law mass distribution of giant molecular clouds (Andre et al., 1996), and the mass-size relation (Solomon et al., 1987). The propagation of photons in the multi-phase ISM is calculated by statistically sampling these clouds in the ray tracing process. Appendix A.1 describes more details of the modeling.

[1] Instability related to the cooling function. In our Galaxy, main coolant of warm ISM (~ 8000 K) is [C II] radiation, if the background FUV field is strong enough ($\sim G_0$). This satisfies a condition of the instability (Field, 1965), $(\partial\Lambda/\partial T)_p < 0$, where Λ is the cooling rate per volume. This means that a density perturbation in warm ISM rapidly contracts isobaricaly and becomes a cold clump (~ 100 K), which makes two-phase structure.

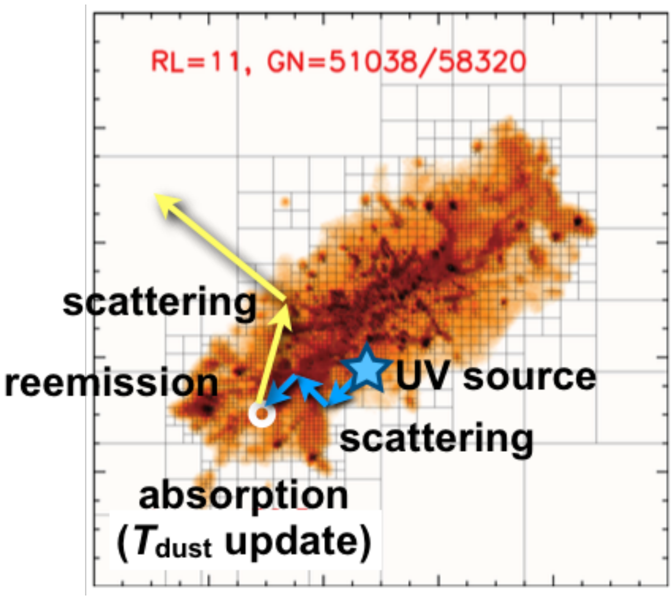

Figure 2.3: Schematic picture of radiative transfer with ART^2, modified from Yajima et al. (2012a). The background picture represents gas density structure in an example galaxy. Grey lines show the boundaries of the AMR grids. Arrows represent propagation track of a photon packet which is emitted from a stellar particle (star symbol) and absorbed by dust at the position of the white circle. The heated dust emits new photon packets with infrared wavelength.

ART^2 also has the 'one-phase mode' which does not use the sub-grid model for multi-phase ISM, but raw gas properties are smoothed over SPH particles within a cell. In this mode, all cells are treated as in the hot phase. We use it in the modeling of metal emission (see the next sub-section).

We assume that the dust-to-gas mass ratio $\mathcal{D}$ in the cold clouds is proportional to the local metallicity as in the local galaxies, $\mathcal{D} = 8 \times 10^{-3}(Z/\mathrm{Z}_{\odot})$ (Draine et al., 2007). On the other hand, $\mathcal{D}$ in the hot phase is scaled by the hydrogen neutral fraction considering the dust destruction in the ionized regions. We adopt the dust size distribution of Todini & Ferrara (2001) for solar metallicity and $M = 22\,\mathrm{M}_{\odot}$ SN model. The dust opacity curve is calculated by combining the size distribution with the cross-section of Weingartner & Draine (2001) (see Fig. 2.4).

To obtain panchromatic SEDs, ART^2 treats the transfer of photons with various frequencies. First, it tracks propagation of ionizing photons. With the obtained ionized structure, it calculates transfer of UV continuum photons and dust absorption/re-emission. When dust absorbs photon packets within a time interval

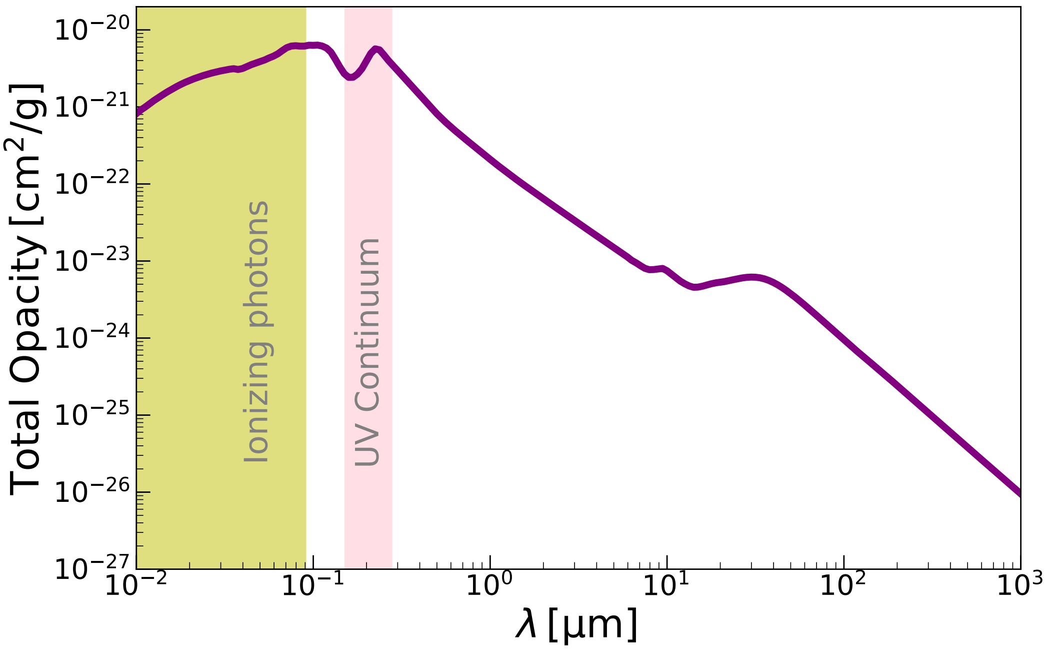

Figure 2.4: The dust opacity curve used in our simulations. The yellow and pink regions show the ranges of hydrogen ionizing photons ($\lambda < 912\,\text{Å}$) and UV continuum photons ($1500 < \lambda < 2800\,\text{Å}$).

Δt, the dust temperature is updated assuming radiative equilibrium:

$$E_{\rm abs} = 4\pi \Delta t \kappa_{\rm P}(T_{\rm d}) B(T_{\rm d}) m_{\rm d}, \tag{2.15}$$

where $\kappa_{\rm P} = \int \kappa_\nu B_\nu d\nu / \int B_\nu d\nu$ is the Planck mean opacity, and B_ν is the blackbody radiation. After the determination of the dust temperature, we calculate radiative transfer of infrared photons from dust. The schematic picture of these processes is presented in Fig. 2.3. Also more detailed formulation is described in Appendix. A.1.

2.3 Modeling of Metal-line Emission

As described in Sec. 1.3.3, metal emission lines are excellent probes for high-z galaxies. These observations allow us to investigate chemical evolution and kinematics in the ISM, which is related to star formation and galaxy evolution. The [C II] radiative cooling produces cold neutral medium (CNM) via thermal instability even at low metallicity (Arata et al., 2018). The confined CNM becomes molecular clouds, and eventually forms stars. The massive stars produce giant H II regions which emit [O III] line. Therefore, combining [C II] and [O III] observations, we can understand physical processes from multi-phase ISM structure to star formation (e.g. Cormier et al., 2012). Here we explain our models for the metal-line emission using ionization structures calculated by ART^2.

2.3.1 [O III] emission model

[O III] emission can be modeled relatively easily compared to [C II] emission (Sec. 2.3.2). Since the ionization potential of $O^+ \to O^{2+}$ is $\Phi_{O^+} = 35.121\,\mathrm{eV}$, O^{2+} ions exist only in H II regions ($\Phi_{H^0} = 13.618\,\mathrm{eV}$). Based on the result of photo-ionization radiative transfer, we can classify the AMR cells into 'H I cells' if the hydrogen neutral fraction is higher than 0.5, otherwise 'H II cells'. We first calculate oxygen abundance in each H II cell assuming ionization equilibrium between O^+ and O^{2+} [2]:

$$\int_{\nu_{\rm min}}^{\infty} n_{\rm O^+} \frac{\sigma_\nu F_\nu}{h\nu} d\nu = \alpha(T) n_{\rm e} n_{\rm O^{2+}}. \tag{2.16}$$

The left hand side represents photo-ionization rate per volume, where $\nu_{\rm min} = 8.492 \times 10^{15}\,\mathrm{Hz}$ is the minimum frequency for ionization. σ_ν is the photo-ionization cross-section for which we use Verner et al. (1996) fitting function (same as CLOUDY, Ferland et al., 1998; Richings et al., 2014a). The total oxygen abundance $n_{\rm O} = n_{\rm O^+} + n_{\rm O^{2+}}$ is estimated from smoothing over particles in the cell. We compute incoming flux F_ν for a H II cell by adding up nearby stellar spectra with assumption of optically thin:

$$F_\nu = \sum_{R_{\rm j} < R_{\rm S}} F_{\nu,\rm j} = \sum_{R_{\rm j} < R_{\rm S}} \frac{L_{\nu,\rm j}}{4\pi R_{\rm j}^2}, \tag{2.17}$$

where $L_{\nu,\rm j}$ is specific luminosity of j-th stellar particle, and $R_{\rm j}$ is the distance from the cell. The distance is limited at the Strömgren radius $R_{\rm S} = (3Q_0/4\pi n_{\rm H}^2 \alpha_{\rm B})^{1/3}$, where Q_0 (s^{-1}) is the ionizing photon rate, and $\alpha_{\rm B}$ is the recombination coefficient in the optically thick limit (case B) [3]. We need this condition to exclude contributions from stellar particles within other H II regions whose ionizing radiation should be interrupted by neutral gas. The right hand side of Eq. (2.16) represents recombination rate per volume, where $\alpha(T)$ is the coefficient as a function of temperature (Nahar & Pradhan, 1997; Nahar, 1999). Figure 2.5 shows the schematic picture describing this photo-ionization model.

The ground energy level of an O^{2+} ion splits into three fine-structure levels of $^3P_0$, $^3P_1$, $^3P_2$ due to the magnetic moment. The [O III] 88 μm FIR forbidden-line is emitted when $^3P_1 \to {}^3P_0$ transition occurs via radiation. There are two ways of

[2] We ignore O I abundance because the ionization potential is similar to that of H I ($\Phi_0 = 13.6181\,\mathrm{eV}$), thus it is natural to consider that all O I atoms are ionized in H II region.

[3] A photon with the energy of 13.6 eV is emitted when a hydrogen and an electron recombine directly to $n = 1$. In the case B, this photons is immediately reabsorbed by another hydrogen atom.

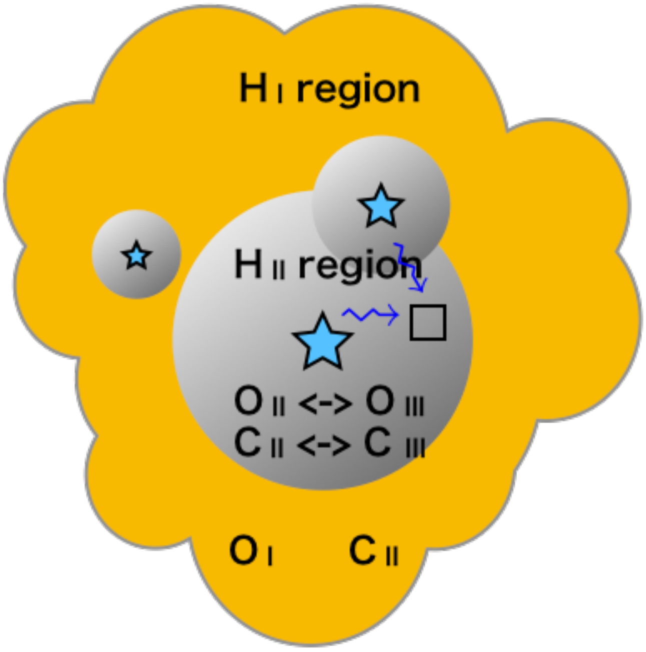

Figure 2.5: Schematic picture of the photo-ionization model for heavy elements. Following ART^2 calculations, we can identify H I regions (yellow) and H II regions (grey). We compute incoming ionizing photons (blue arrows) for O^+ ions (35 eV) from nearby stars (Eq. 2.17). In H II regions, we calculate the abundance ratios between O^+ and O^{2+}, and C^+ and C^{2+} under the assumption of ionization equilibrium. In H I regions, we assume all of oxygen in O I and carbon in C II.

the radiative de-excitation in general: spontaneous emission, $X_u \to X_\ell + h\nu$, and stimulated emission, $X_u + h\nu \to X_\ell + 2h\nu$, where $\nu = (E_u - E_\ell)/h$ is the frequency of the emission, and E_u, E_ℓ represent energies of the upper and lower levels. The rate of stimulated emission depends on the radiation field (J_ν) and the number density of ions in the upper level (n_u), $n_u B_{u\ell} J_\nu$, where $B_{u\ell}$ is called Einstein B coefficient. The spontaneous emission is a random process with a probability per unit time $A_{u\ell}$ that is called Einstein A coefficient. We calculate the rate equations between the three levels (Nussbaumer & Storey, 1981; Aggarwal & Keenan, 1999), and obtain the level population. The [O III] luminosity for a H II cell is

$$L = (C_{\rm lu} n_{\rm l} - C_{\rm ul} n_{\rm u}) \beta h \nu_{\rm ul} V_{\rm cell}, \tag{2.18}$$

where $C_{\rm lu}$ ($C_{\rm ul}$) is the Einstein coefficient of collisional excitation (de-excitation) which depends on electron density. The $V_{\rm cell}$ is the cell volume. The β is escape probability, which we assume optically thin i.e., $\beta = 1$. In addition, if gas temperature is higher than 1.2×10^5 K, we set the luminosity to zero because O^{2+} ions are ionized to more highly ionization states by collisions (Nahar, 1999).

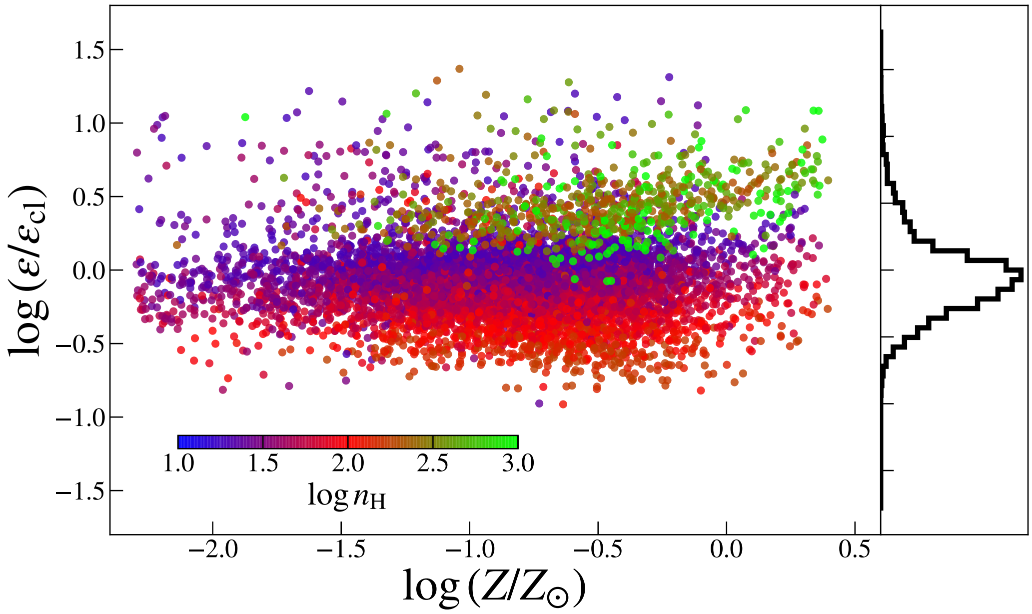

Figure 2.6: Comparison of [O III] emissivity computed by our code (ϵ) and CLOUDY ($\epsilon_{\rm cl}$). Each point shows the ratio of emissivity for a cell in Halo-11 at $z = 6.0$ as a function of metallicity. The color is scaled by gas density. Right panel shows the probably distribution function of $\log(\epsilon/\epsilon_{\rm cl})$ in linear-scale.

We here compare our [O III] 88 μm emissivity with that estimated by CLOUDY. The CLOUDY table[4] has luminosity ratio of [O III] to Hβ lines ($\epsilon_{\rm cl} \equiv (L_{\rm [O\,III]}/L_{\rm H\beta})_{\rm cl}$) as a function of gas density (n), ionization parameter ($U \equiv \Phi({\rm H})/n_{\rm e}c$, where Φ(H) is flux of ionizing photons) and metallicity (Z), which was derived from radiative transfer calculations with assumption of plane-parallel gas structure. The ranges of the parameters are $1 \leq \log(n/{\rm cm}^{-3}) \leq 3$, $-4 \leq \log U \leq -1$ and $-4 \leq \log Z \leq 0.05$. We further estimate Hβ luminosity for each cell as $L_{\rm H\beta} = \alpha^{\rm eff}_{\rm H\beta}(T) n_{\rm p} n_{\rm e} h\nu_{\rm H\beta} V_{\rm cell}$, where $\alpha^{\rm eff}_{\rm H\beta}(T)$ is the effective recombination coefficient (Brocklehurst, 1971), and compute the [O III] emissivity for our model as $\epsilon \equiv L_{\rm [O\,III]}/L_{\rm H\beta}$.

Figure 2.6 presents a distribution of the $\epsilon/\epsilon_{\rm cl}$ ratio. As shown in the right panel, most of cells have $\epsilon/\epsilon_{\rm cl} \sim 1$, thus our model is consistent with CLOUDY. The total [O III] luminosity is mainly contributed from cells with $|\log(\epsilon/\epsilon_{\rm cl})| < 0.5$ ($\sim 72\,\%$). Here we focus on the origin of the differences between our model calculation and CLOUDY. There are two-types of outliers at $\log(\epsilon/\epsilon_{\rm cl}) > 0.5$: low-$U$ cells ($\log U \sim -4$) and high-density cells ($n \gtrsim 500\,{\rm cm}^{-3}$). In the former case, CLOUDY predicts that the weak radiation field ionizes the surface of plane-parallel

[4] We obtained the CLOUDY table from Dr. Inoue in private discussion, which is based on Inoue (2011) and Inoue et al. (2014).

gas ($N \lesssim 10^{19}\,\mathrm{cm^{-2}}$), and [O III] is emitted only from the thin layer. Meanwhile, if the electron fraction of a cell is higher than 0.5, our model calculates optically-thin oxygen ionization equilibrium in the whole cell volume and obtains O^{2+} abundance, which would overestimate [O III] emissivity. In the latter case (indicated by green points), the emissivity in CLOUDY rapidly decreases with increasing density, because the density exceeds the critical density for transition of $^3P_1 \rightarrow {}^3P_0$. Meanwhile, our model predicts that the critical density is higher by a factor of ~ 3 ($1.74 \times 10^3\,\mathrm{cm^{-3}}$ at $T = 10^4\,\mathrm{K}$), thus the emissivity increases with density. The difference probably comes from used references of the collision strength $\Omega_{\rm ul}$ (Aggarwal & Keenan, 1999).

As described above, CLOUDY uses input spectrum assuming a simple stellar population. However, the actual SED would be the sum of various stellar populations with different ages and metallicities, which could be more complex. Also, CLOUDY assumes the solar abundance ratio, but the chemical abundance in high-z galaxies might be very different from our Galaxy. Our model calculates O^{2+} abundance under the complex SEDs, and the oxygen enrichment by SNe and AGB stars is tracked by particles separately. Thus, we argue that, at least for the SED treatment, our model is doing a more appropriate treatment for estimating [O III] emission in high-z galaxies.

2.3.2 [C II] emission model

The [C II] 158 μm FIR line can be radiated from various gas phases i.e. warm ionized medium (WIM), warm neutral medim (WNM), cold neutral medium (CNM) and molecular clouds (e.g. Wolfire et al., 2003), thus the modeling is relatively difficult. The previous theoretical studies constrained each contribution using cosmological hydrodynamic simulations (Vallini et al., 2015; Olsen et al., 2017; Pallottini et al., 2017; Katz et al., 2019). Modeling [C II] emission based on local molecular fraction, Olsen et al. (2017) showed that diffuse ionized gas and molecular clouds were main contributors to [C II] luminosity. Observationally, the constrains of the contributions are also complicated because of the difficulty of determining optical depth for the line (e.g. Neri et al., 2014).

The [C II] emission model is almost the same with that of the [O III] emission described in the previous sub-section. The main different point is that we allow both H I and H II cells to radiate the [C II] line. For H II cells, we calculate ionization equilibrium between C^+ and C^{2+} under the stellar radiation field (Eq. 2.16). Meanwhile, we assume that all carbons are in C^+ ions for H I cells. In our Galaxy, carbons are almost completely in C^+ ions under FUV ($G_0 = 0.6\,$Habing) and cosmic ray backgrounds which are radiated by nearby star-forming regions and external galaxies (e.g. Webber, 1998; Seon et al., 2011). Thus our assumption is valid for main sequence galaxies, or at least gives us upper limit of the [C II] luminosity.

The [C II] 158 μm FIR line is radiated when transition occurs in the fine-structure levels $^2\mathrm{P}_{3/2} \rightarrow {}^2\mathrm{P}_{1/2}$. We calculate the luminosity with the same manner as the [O I II] emission (Eq. 2.18). If temperature of a cell is higher than 4.0×10^4 K, we set the luminosity to zero considering collisional ionization of $\mathrm{C}^+ \rightarrow \mathrm{C}^{2+}$ (Nahar & Pradhan, 1997). In this paper, we assume optically thin emission ($\beta = 1$). Note that, however, Neri et al. (2014) suggested that the optical depth for an observed $z \sim 5.2$ galaxy could be $\tau_{[\mathrm{C\,II}]} \gtrsim 1$. If this property is common for high-z galaxies, our model predicts a further upper limit of the [C II] luminosity. In addition, we note that the cosmic microwave background (CMB) can affect the [C II] emission (e.g. Goldsmith et al., 2012; da Cunha et al., 2013). As redshift increases, the CMB temperature ($T_{\mathrm{CMB}} = 2.73(1 + z)$ K) approaches to the equivalent temperature of the [C II] emission ($T_{\mathrm{eq}} = 91.2$ K). Thus stimulated emission/absorption can be significant for $z \gtrsim 6$ galaxies (Vallini et al., 2015; Lagache et al., 2018).

Here we estimate the CMB effect onto [C II] 158 μm luminosity (e.g. Goldsmith et al., 2012). The population for two energy levels is determined by the rate equation:

$$n_u(A_{u\ell} + B_{u\ell}J_\nu + C_{u\ell}) = n_\ell(B_{\ell u}J_\nu + C_{\ell u}), \tag{2.19}$$

where $n_u(n_\ell)$ is the number density of C^+ ions at upper (lower) level, and J_ν is the mean intensity of the background radiation at 158 μm. We assume $\beta = 1$ and the black-body spectra $J_\nu = B_\nu(T_{\mathrm{CMB}})$. The $C_{\ell u}$ term is the sum of the collision rates with electrons (e^-), hydrogen atoms (H^0) and hydrogen molecules (H_2) (Glover & Jappsen, 2007). The $C_{\ell u}$ and $C_{u\ell}$ are related by detailed balance.The emergent luminosity is computed from Eq. (2.18). In diffuse ISM, the stimulated absorption rate ($n_\ell B_{\ell u} J_\nu$) is higher than stimulated emission rate ($n_u B_{u\ell} J_\nu$), thus the CMB increases n_u/n_ℓ ratio, and reduces the [C II] luminosity.

Figure 2.7 presents how much [C II] emission is suppressed by CMB at $z = 7.0$. For low temperature gas ($T \lesssim 100$ K), the CMB effect becomes significant compared to the collisional excitation, resulting in reduction of the luminosity by $\gtrsim 3$ %. At temperature of $T \sim 10^4$ K, densities of e^- and H^0 dramatically change due to hydrogen recombination, thus the collision partner for C^+ ions switches. If the gas density is higher than the critical density of the collision partner, the rate equation is dominated by the collision terms, resulting in that the CMB effect becomes negligible. Note that, as described later, the gas temperature in our simulations is higher than 10^3 K, thus the CMB effect affects the [C II] luminosity only by a few percent.

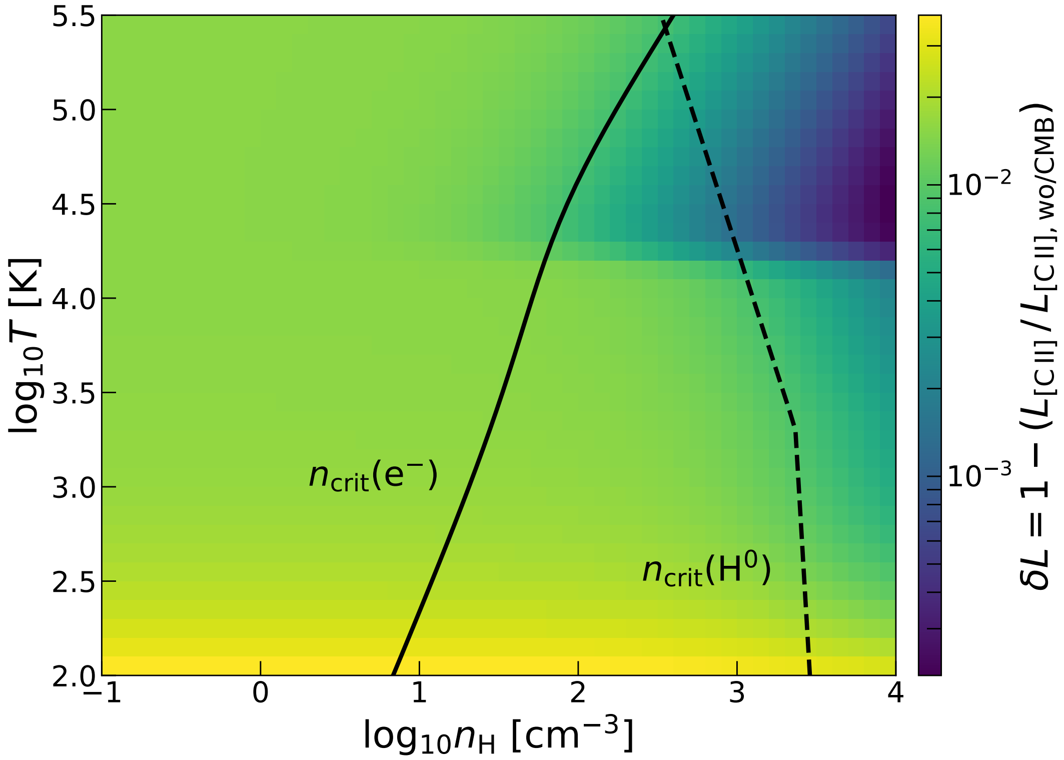

Figure 2.7: The CMB effect to [C II] luminosity for a specific gas phase. The color is scaled by the strength of the CMB attenuation, where $L_{[\mathrm{C\,II}],\mathrm{wo/CMB}}$ is [C II] luminosity neglecting the stimulated absorption/emission by CMB at $z = 7$, as a function of the gas density (n) and temperature (T). Black solid and dashed lines represent the critical density for electrons (e^-) and hydrogen atoms (H^0), respectively. The collision partner for C^+ changes at $T \sim 10^4\,\mathrm{K}$ due to hydrogen recombination.

Chapter 3

Results of Multi-wavelength Analysises

The contents of this chapter is based on two papers; 1) "Radiative properties of the first galaxies: rapid transition between UV and infrared bright phases", Arata, S., Yajima, H., Nagamine, K., Li, Y., Khochfar, S., Monthly Notices of the Royal Astronomical Society (MNRAS), vol. 488, pp. 2629-2643, 2019. 2) "Starbursting [O III] emitters and quiescent [C II] emitters", Arata, S., Yajima, H. Nagamine, K., Abe, M., Khochfar, S., MNRAS, submitted (arXiv: 2001.01853 [astro-ph.GA]).

3.1 Projected Images and Spectral Energy Distribution

Figure 3.1 presents the projected images of surface density of gas, stars and dust, dust temperature, and surface brightness in rest-frame UV, FIR, [O III] and [C II] wavelength in Halo-11 at $z = 6.0$. The total gas mass, stellar mass, and dust mass are $M_{\rm gas} = 1.1 \times 10^{10}\, h^{-1}{\rm M}_{\odot}$, $M_{\star} = 2.2 \times 10^{9}\, h^{-1}{\rm M}_{\odot}$ and $M_{\rm dust} = 1.9 \times 10^{7}\, h^{-1}{\rm M}_{\odot}$.

Left panel in the top row shows gas column density extending about 20 kpc in physical scale, which has filamentaly structures (pink). The main galaxy resides at the center, and there are some clumpy satellite galaxies. Stars form in very high-density regions (white). The tiny shell structures are created by SN winds. The middle panel shows stellar distribution reflecting old stellar population. The right panel shows dust mass which concentrates at the central star-forming regions.

In the middle row, left panel shows dust temperature after computing radiative transfer. At the star-forming regions, dust is efficiently heated to $\gtrsim 60\,{\rm K}$ by strong stellar irradiation. Note that cool dust component ($\sim 30\,{\rm K}$) also exists with similar amount to hot dust. We argue that previous observations of $z \sim 6$ galaxies in

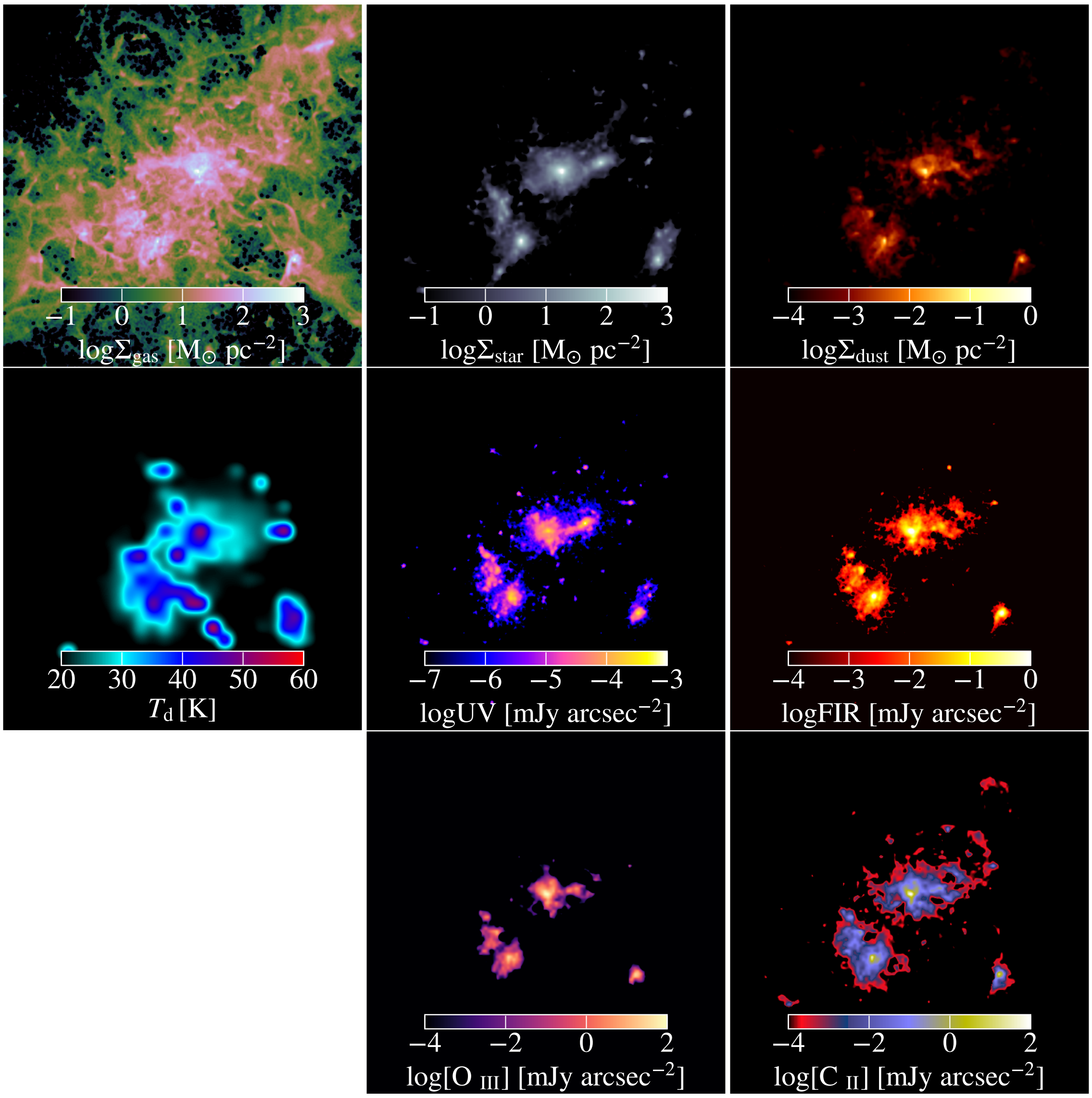

Figure 3.1: Projected images of Halo-11 at $z = 6.0$. Top panels show surface density of gas (left), stars (middle) and dust (right) in the unit of $\mathrm{M_\odot\ pc^{-2}}$. The spatial scale is ~ 51 physical kpc. Middle panels show dust temperature and surface brightness of rest-UV and rest-FIR continuum in the unit of mJy $\mathrm{arcsec^{-2}}$. The pixel size is ~ 0.02 arcsec. Bottom panels show surface brightness in [O III] 88 μm and [C II] 158 μm wavelength. The pixel size is ~ 0.07 arcsec, corresponding to ~ 0.4 kpc.

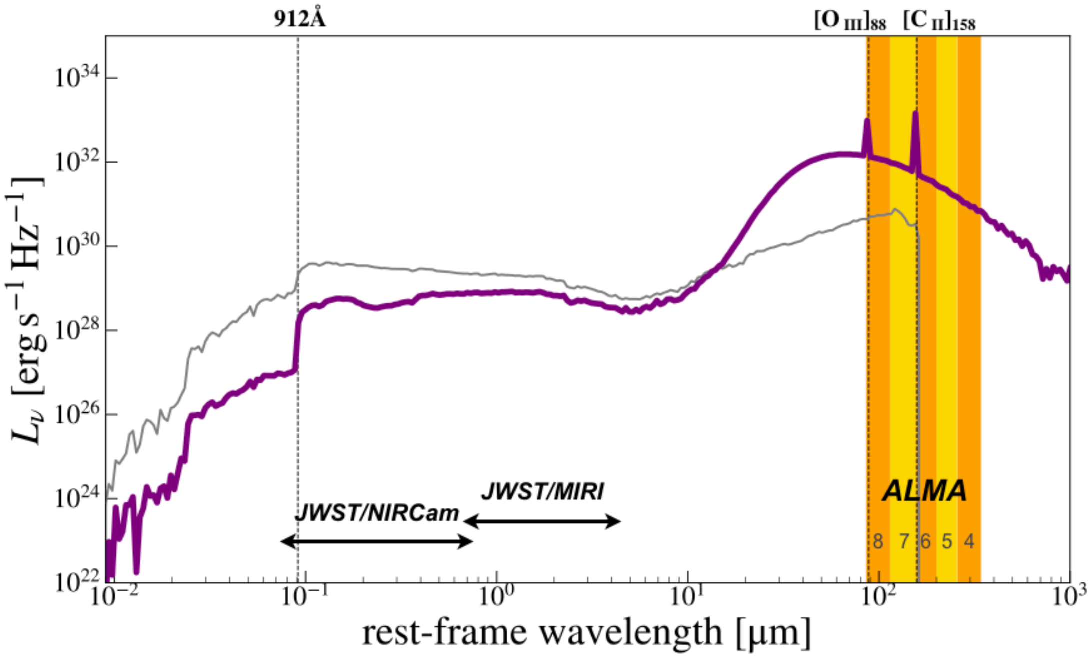

Figure 3.2: Spectral energy distribution of Halo-11 at $z = 6$. Gray and purple lines show the intrinsic and emergent spectra, respectively. Dotted line indicate wavelengths of Lyman-limit (912 Å), [O III] 88.3 μm and [C II] 157.8 μm. The ALMA bands for $z = 6$ galaxies are shown by orange and yellow colors. The ranges of JWST/NIRCam and JWST/MIRI are also shown.

sub-mm (850 μm) wavelength have taken the hot component, but longer wavelength observation (1.1 mm) will reveal abundant cold dust.

The middle and right panels show surface brightness in rest-UV and FIR wavelength. The UV map represents distribution of young stars, and dust distribution for FIR map. Some stars are not covered by dust screen due to SN feedback, which results in differences between the two maps.

The bottom panels show surface brightness of [O III] 88 μm and [C II] 158 μm wavelength. The [O III] map represents H II regions formed by massive stars, while extended neutral gas for [C II] map. We find that deep [C II] observation ($\lesssim 10^{-2}$ mJy arcsec^{-2}) would reveal the ~ 20 kpc extended gas structure.

3.2 Physical Properties of Gas

Top panel of Figure 3.3 shows gas phase diagram of Halo-11. The accreting gas is heated by shocks to $\sim 10^6 - 10^7$ K, and radiatively cools down to $\sim 10^4$ K with

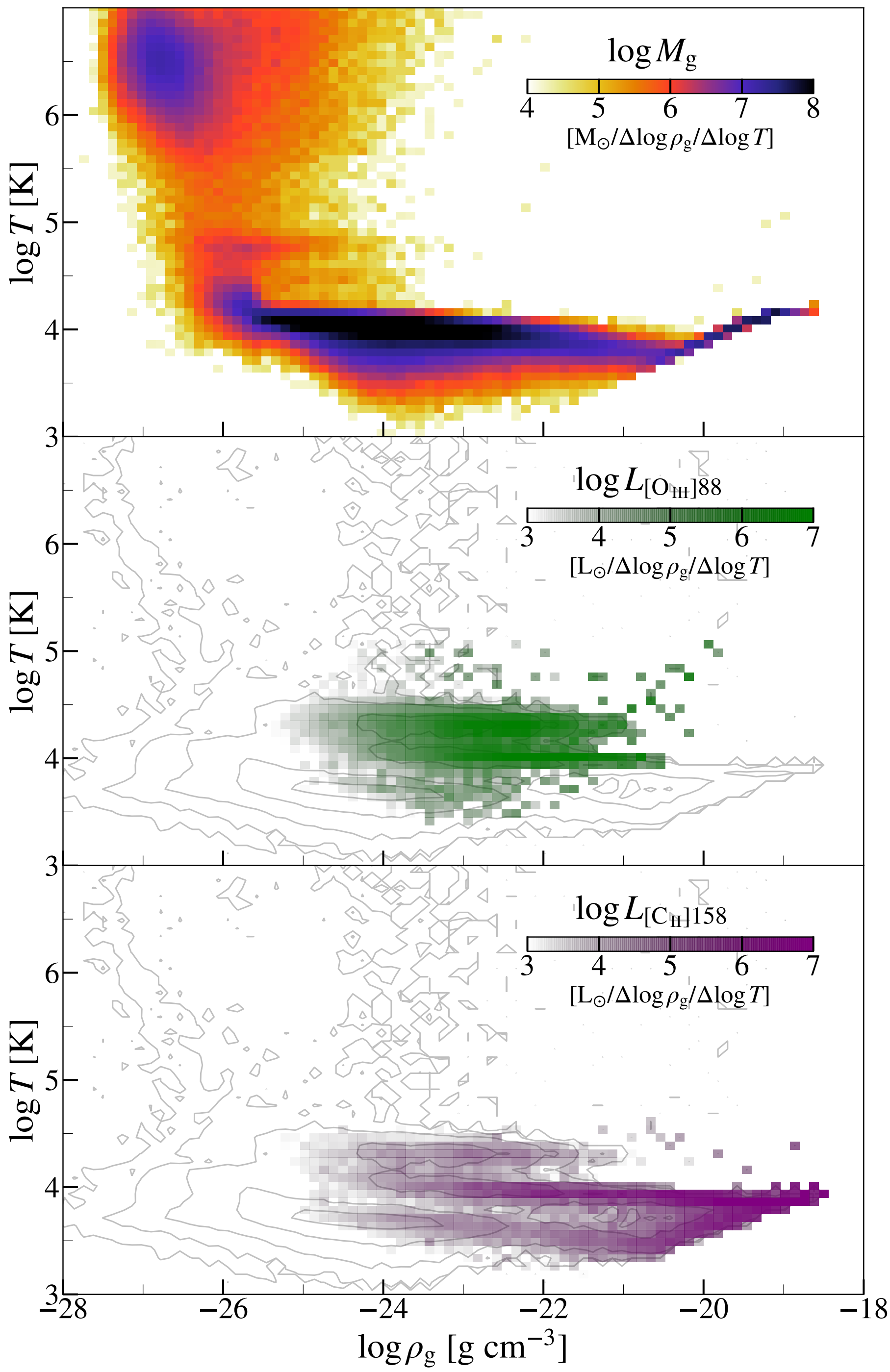

Figure 3.3: *(Top panel)* Phase diagram of gas in Halo-11 at $z = 6$. *(Middle and bottom panels)* [O III] 88 μm and [C II] 158 μm emitting gas phases, respectively. Grey contours represent phase diagram after calculating radiative transfer. This figure is modified from Arata et al. (2020).

increasing density. When gas density exceeds $10\,\mathrm{cm^{-3}}$, the gas starts to form stars with the effective equation of state ($\gamma = 4/3$). Very high-density gas ($\gtrsim 10^3\,\mathrm{cm^{-3}}$) follows the pressure floor to avoid artificial fragmentation. SN feedback returns gas to hot ionized phase.

The [O III] and [C II] emitting gas phases are presented in the middle and bottom panels. After radiative transfer (grey contours), temperature of completely ionized gas ($x_\mathrm{e} > 0.99$) becomes $\sim 2 \times 10^4\,\mathrm{K}$. On the other hand, partially ionized gas has lower temperature ($\lesssim 10^4\,\mathrm{K}$). We do not consider the UV background in RT calculations, which could be important for ionization state of IGM. However, we focus on gas evolution whose density is higher than the self-shielding threshold density ($n_\mathrm{th} \sim 10^{-2}\,\mathrm{cm^{-3}}$, Nagamine et al., 2010; Altay et al., 2011; Yajima et al., 2012b; Bird et al., 2013; Rahmati et al., 2013). The total luminosity of [O III] line is $2.26 \times 10^{42}\,\mathrm{erg\ s^{-1}}$, and the half of it is contributed from completely ionized regions. The total [C II] luminosity is $2.0 \times 10^{42}\,\mathrm{erg\ s^{-1}}$, and neutral phase ($x_\mathrm{e} < 0.5$) contribute to it (99 %). Especially, high-density clouds ($> 10^3\,\mathrm{cm^{-3}}$) is the main contributor (88 %) to the total luminosity. Observationally, Croxall et al. (2017) studied the contribution from neutral gas using the local star-forming galaxies, and showed that it decreased from $\sim 90\,\%$ to $\sim 60\,\%$ as gas metallicity increased from $12+\log(\mathrm{O/H}) \sim 8.0$ to 8.6. The metallicity of Halo-11 at $z = 6.0$ is $12+\log(\mathrm{O/H}) \approx 8.1$. Thus our simulations are consistent with the observational result.

3.3 Redshift Evolution of First Galaxies

3.3.1 SFR and UV Continuum Escape Fraction

Here we focus on physical processes affecting evolution of first galaxies using our fiducial runs (Halo-11 and Halo-12). The top panel of Figure 3.4 shows redshift evolution of SFRs at $z = 6 - 15$. We observe that star formation proceeds intermittently. Star-burst occurs at the central high-density regions, however massive stars explode as SNe and evacuate gas in $\sim 10\,\mathrm{Myr}$ later which corresponds to the life-time of massive stars. The ejected gas will accrete onto the center due to gravitational potential, and stars form again. Thus, evolution of first galaxies has two phases of star-burst and outflowing, as described in Yajima et al. (2017b) (see also, Kimm & Cen, 2014). The SFRs of Halo-11 and Halo-12 reach to $35\,\mathrm{M_\odot\ yr^{-1}}$ and $\sim 203\,\mathrm{M_\odot\ yr^{-1}}$ at $z = 6$, respectively. These values are close to observed SFR in LAEs and LBGs estimated from their UV luminosity (e.g. Ouchi et al., 2009; Ono et al., 2012; Watson et al., 2015).

The second panel shows escape fraction of UV continuum photons (1500 −

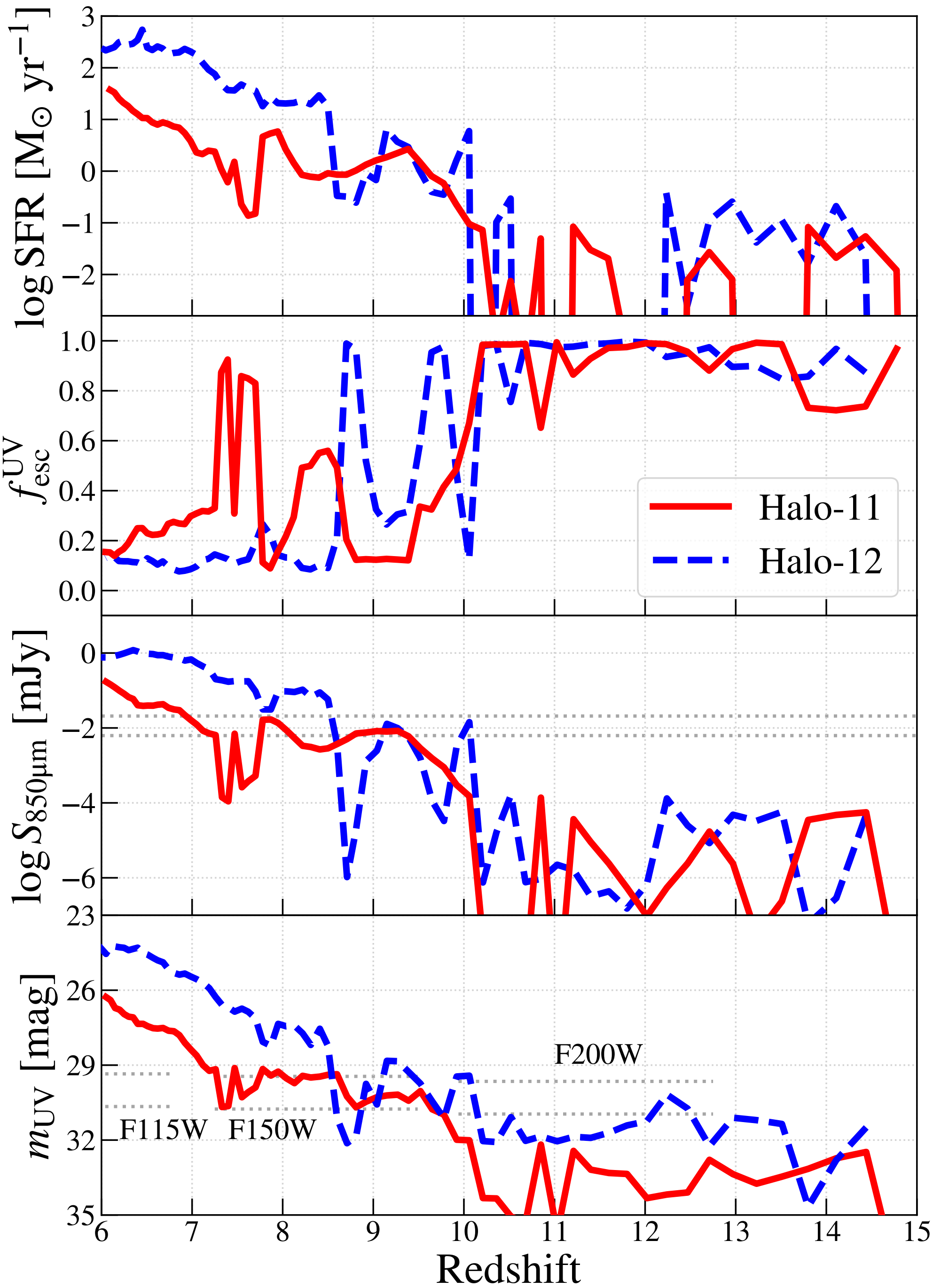

Figure 3.4: Redshift evolution of star formation rate (top panel), escape fraction of UV photons (second panel), observed sub-mm flux (third panel) and apparent AB magnitude at rest-frame 1500 Å (bottom panel) for Halo-11 (red solid line) and Halo-12 (blue dashed line). The gray horizontal lines in the third and forth panels show 3σ (lower line) and 10σ (higher line) detection thresholds for ALMA (full operation) and JWST with 10 hours time integration, which are obtained from the sensitivity calculator in each observatory. (Modified from Arata et al., 2019)

2800 Å). We define escape fraction as

$$f_{\rm esc}^{\rm UV} \equiv \frac{L_{\rm out}^{\rm UV}}{L_{\rm int}^{\rm UV}}, \tag{3.1}$$

where $L_{\rm int}^{\rm UV}$ is intrinsic luminosity, and $L_{\rm out}^{\rm UV}$ is dust-attenuated emergent luminosity measured at the virial radius. The intrinsic SED is computed from integrating stellar spectra calculated by STARBURST99 using their metallicities and ages (see Sec. 2.2). At very high-redshift ($z > 10$), escape fraction is very high ($f_{\rm esc}^{\rm UV} \sim 0.7 - 1.0$) in both cases of Halo-11 and Halo-12, because the galaxies do not have significant amount of dust. For example, dust mass in Halo-11 at $z = 12$ is $1.5 \times 10^4\,{\rm M_\odot}$, which is only 0.29 % compared to the stellar mass. At lower redshift ($z < 10$), escape fraction of Halo-11 largely fluctuates between $f_{\rm esc}^{\rm UV} \sim 0.2 - 0.8$. In star-burst phase, dusty gas concentrates on the galactic center and absorbs UV photons efficiently, resulting in decreasing escape fraction. Meanwhile, UV photons easily escape from the halo through holes of the ejected gas, and escape fraction increases.

To confirm these processes, we measure dust distribution and optical depth to UV photons (τ_{1500}) for Halo-11 at $z = 9.0$ and 8.5 (Figure 3.5a). The two redshift corresponds to star-burst and outflowing phases, respectively (see Fig. 3.4). We compute mean dust density for each spherical shell centering on the star-forming region, and integrate the optical depth $\tau_{1500} = \sum \kappa_{1500}\rho_{{\rm dust},i}\Delta r_i$, where κ_{1500} is opacity in 1500 Å, and Δr_i is width of i-th shell. As expected, dust concentrates at the central region and the system is optically thick ($\tau_{1500} \sim 1$) at $z = 9.0$, and becomes optically thin ($\tau_{1500} \sim 10^{-2}$) at $z = 8.5$ because dusty gas is ejected by SNe to outside in outflowing phase. Therefore, we conclude that changes of dust distribution with intermittent star formation are the cause of the fluctuation of UV escape fraction. Note that increment of $f_{\rm esc}^{\rm UV}$ in outflowing phases has varieties due to three-dimensional dust distributions. The dust opacity to IR photons is $\sim 10^3$ times lower than that of UV (Fig. 2.4), thus most of re-emitted photons would not be re-scattered and escape from the halo.

Next we consider time-scale of the phase transitions based on a simple spherical shell model. The total SNe energy released by single starburst is

$$E_{\rm SNe} \sim 10^{55} \left(\frac{\rm SFR}{0.1\,{\rm M_\odot\ yr^{-1}}}\right)\left(\frac{t_{\rm life}}{10\,{\rm Myr}}\right)\ {\rm erg}, \tag{3.2}$$

where $t_{\rm life}$ is the lifetime of massive stars and we set the energy of each SN as 10^{51} erg. It easily exceeds the gravitational binding energy of a star-forming gas cloud considering the Jeans instability

$$E_{\rm b,g} \sim GM_{\rm Jeans}^2/2L_{\rm Jeans} \sim 10^{53}\,{\rm erg}. \tag{3.3}$$

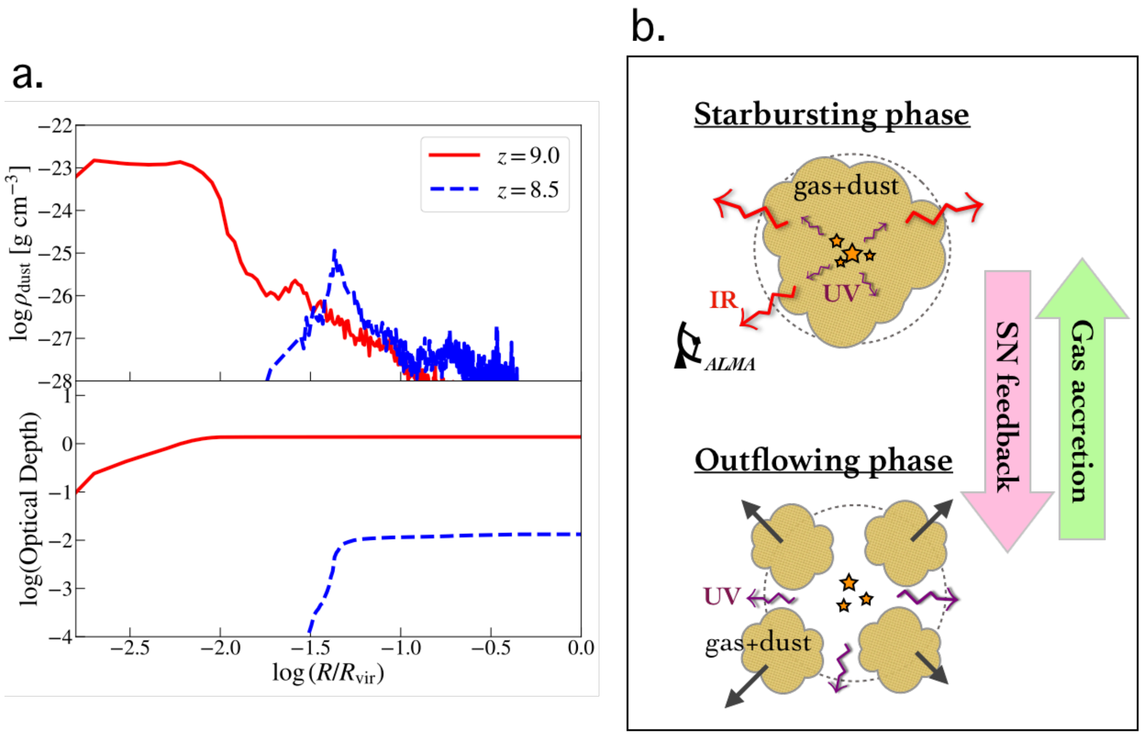

Figure 3.5: (a) Radial profiles of dust density (top panel) and the optical depth to rest-frame 1500 Å (bottom panel) in Halo-11 at $z = 9.0$ (red line) and $z = 8.5$ (blue line) which represent star-burst phase and outflow phase, respectively. (Modified from Arata et al., 2019) **(b)** Schematic picture of relation between intermittent star formation and the radiative properties. In star-burst phase, UV light is efficiently converted into IR photons by dust absorption/re-emission, which is possible to be the ALMA source. After ~ 10 Myr later, SNe evacuate dusty gas and UV photons can escape easily. The outflowing gas will accrete onto the center in ~ 100 Myr if gravitational potential is deep enough to retain gas within the halo. Thus, galaxies rapidly change their colors between blue and red.

On the other hand, it is difficult to exceed biding energy of the host halo,

$$E_{\rm b,h} \sim 10^{56} \left(\frac{M_{\rm h}}{10^{10}\,{\rm M}_{\odot}}\right)^{5/3} \left(\frac{1+z}{10}\right) \left(\frac{\Omega_{\rm b}/\Omega_{\rm m}}{0.16}\right) \,{\rm erg}. \tag{3.4}$$

Thus, SNe can evacuate gas from the galactic center but not from the halo. Therefore, outflowing shell will stall at some radius and fall back to the centre within a free-fall time. If the shell falls from the virial radius, the free-fall time is

$$t_{\rm ff} \sim \left(2r_{\rm vir}^3/GM_{\rm h}\right)^{1/2} \sim 100 \left(\frac{1+z}{10}\right)^{-3/2} \,{\rm Myr}. \tag{3.5}$$

This is consistent with our simulation results because the transitions occur a few times within 450 Myr ($z = 6 - 10$).

In addition, the fluctuation of escape fraction stops at $z \sim 7$ ($z \sim 8.5$) and gradually decreases to $f_{\rm esc}^{\rm UV} \sim 0.1$ in the case of Halo-11 (Halo-12). At the redshift, gas mass within the central 200 pc region becomes $\gtrsim 10^{10}\,{\rm M_\odot}$, and the binding energy exceeds the injected energy by SNe even in an intense star-burst of SFR $\gtrsim 10\,{\rm M_\odot\ yr^{-1}}$. This results in retaining dusty gas at the center, and $f_{\rm esc}^{\rm UV}$ keeps low value. We find that more massive galaxies have lower escape fraction due to earlier gas accumulation. The varieties of $f_{\rm esc}^{\rm UV}$ are closely related to observed UV LF. For example, if the UV apparent magnitude of $m_{\rm UV} \sim 30$ fluctuates by a factor of 2 at $z = 7-8$, it could make flatter LF at the faint-end.

3.3.2 Sub-millimeter Flux and UV Magnitude

When dust efficiently absorbs UV light, the galaxy becomes bright in rest-frame FIR and could be detected by sub-millimeter observations (e.g., Riechers et al., 2013; Watson et al., 2015). The third panel of Fig. 3.4 shows fluxes of observed-frame 850 μm [1]. We find that sub-mm flux at $z < 10$ fluctuates about 1 order magnitude with intermittent star formation. In star-burst phases, the flux of Halo-11 (Halo-12) reaches $S_{850\,\mu{\rm m}} \sim 0.1$ mJy (1 mJy) at $z \sim 6-7$, which has a good agreement with an observed galaxy at $z = 7.5$ (A1689-zD1, Watson et al., 2015). This galaxy was gravitationally lensed by a foreground galaxy cluster, and the sub-mm flux was 0.61 ± 0.12 mJy. Correcting the lens effect, estimated SFR and dust mass were $\sim 12\,{\rm M_\odot\ yr^{-1}}$ and $\sim 4 \times 10^7\,{\rm M_\odot}$. The dust mass of Halo-11 and Halo-12 at $z = 7.5$

[1] Let us consider luminosity in the range of $[\nu_s,\ \nu_s + \delta\nu_s]$ when the radiation is emitted from the source, which is written as $L_{\nu_s}\delta\nu_s$. The released energy during $[t_s,\ t_s + \delta t_s]$ is $\delta E = L_{\nu_s}\delta\nu_s\delta t_s$. The number of photons is obtained by dividing energy of a photon,

$$\delta N = \frac{\delta E}{h\nu_s} = \frac{L_{\nu_s}}{h\nu_s}\delta\nu_s\delta t_s. \tag{3.6}$$

During travel of the photons from the source at redshift z to observer, the frequency becomes $\nu_o = \nu_s/(1+z)$ due to the effect of cosmic expansion. Also the time-interval of receiving the photons becomes $\delta t_o = (1+z)\delta t_s$. The number of photons is conserved, thus equation (3.6) is rewritten as

$$\delta N = \frac{L_{\nu_o(1+z)}}{h\nu_o(1+z)}\delta\nu_o\delta t_o. \tag{3.7}$$

The received energy per unit area and unit time is

$$F_{\nu_o}\delta\nu_o = \frac{h\nu_o\delta N}{4\pi r^2\delta t_o} = \frac{L_{\nu_o(1+z)}}{4\pi r^2(1+z)}\delta\nu_o, \tag{3.8}$$

where r is physical distance to the source, which is related to the luminosity distance, $d_{\rm L} = (1+z)r$. Finally, we obtain the equation for converting intrinsic specific luminosity to observed flux,

$$F_{\nu_o} = \frac{(1+z)L_{\nu_s}}{4\pi d_{\rm L}^2}. \tag{3.9}$$

are $\sim 5 \times 10^6$ and $\sim 8 \times 10^7\,\mathrm{M}_\odot$, respectively, thus A1689-zD1 is intermediate among Halo-11 and Halo-12. We also show the observational sensitivity of ALMA as dotted lines. Our simulations suggest that a reasonable time-integration (~ 1 hour) could observe $z \lesssim 8$ galaxies, which is consistent with recent detections of dust emission ar $z > 6$. Also we expect that galaxies at $z \sim 9$ would be detected with > 10 hours integration.

On the other hand, SED of the galaxy becomes blue in outflowing phases. The bottom panel of Fig. 3.4 shows the evolution of apparent UV (1500 Å) magnitude. When $f_{\rm esc}^{\rm UV}$ is high, star formation is quenched and intrinsic UV emission becomes weak. Thus the fluctuation amplitude of UV magnitude is moderate comparing to sub-mm flux. Present observational detection limit is $m_{\rm UV} \sim 30$ (see Sec. 1.3.1). Our simulations are consistent with the observed LBG samples at $z < 10$. For reference, we also show the sensitivity of JWST in the figure. This comparison suggests that the detection of Halo-11 at $z > 10$ is very difficult, whereas the Lyα flux from the first galaxies can be detected even at $z \gtrsim 10$. Lyα photons are produced via recombination or collisional excitation processes in cold gas flows (Yajima et al., 2015b). Also the strong ionizing flux of a massive galaxy forms huge H II bubbles ($\gtrsim 100$ kpc) which increases the IGM transmission of Lyα photons (Yajima et al., 2018). Therefore, we argue that Lyα is the best tool for searching most distant galaxy by JWST.

3.3.3 Lyman-Continuum Escape Fraction and Metal-line Luminosity

Figure 3.6a shows redshift evolution of Halo-11 focused on metal-line emission. The top panel shows SFR again.[2] The middle panel shows escape fraction of LyC photons $f_{\rm esc}^{\rm LyC}$ which is defined as the same form of $f_{\rm esc}^{\rm UV}$ (Eq. 3.1) but in different wavelength (≤ 912 Å). Similarly with $f_{\rm esc}^{\rm UV}$, escape fraction of LyC photons also rapidly fluctuates, but takes lower value ($\sim 0.01 - 0.2$) with time-averaged value of ~ 0.06 at $z = 6 - 10$. As the halo mass increases, $f_{\rm esc}^{\rm LyC}$ decreases due to accumlating dusty gas, which implies that abundant low-mass galaxies might be crucial to reionize Universe although production rate of ionizing photons per one halo had small contribution (Wise et al., 2012b,a). Also the halo mass dependence is consistent with previous numerical results (Yajima et al., 2011; Paardekooper et al., 2015). Note that high numerical resolution of simulations can resolve high-density gas clumps

[2]The SFR evolution in Fig. 3.6 is slightly different from that seen in Fig. 3.4. Our simulation code Gadget-3 uses the number of processors as seed of generating random number to compute stochastic events. The Halo-11 runs in Fig. 3.4 and 3.6 were conducted with 32 and 256 processors, resulting in the slight difference. However, it does not change qualitative arguments.

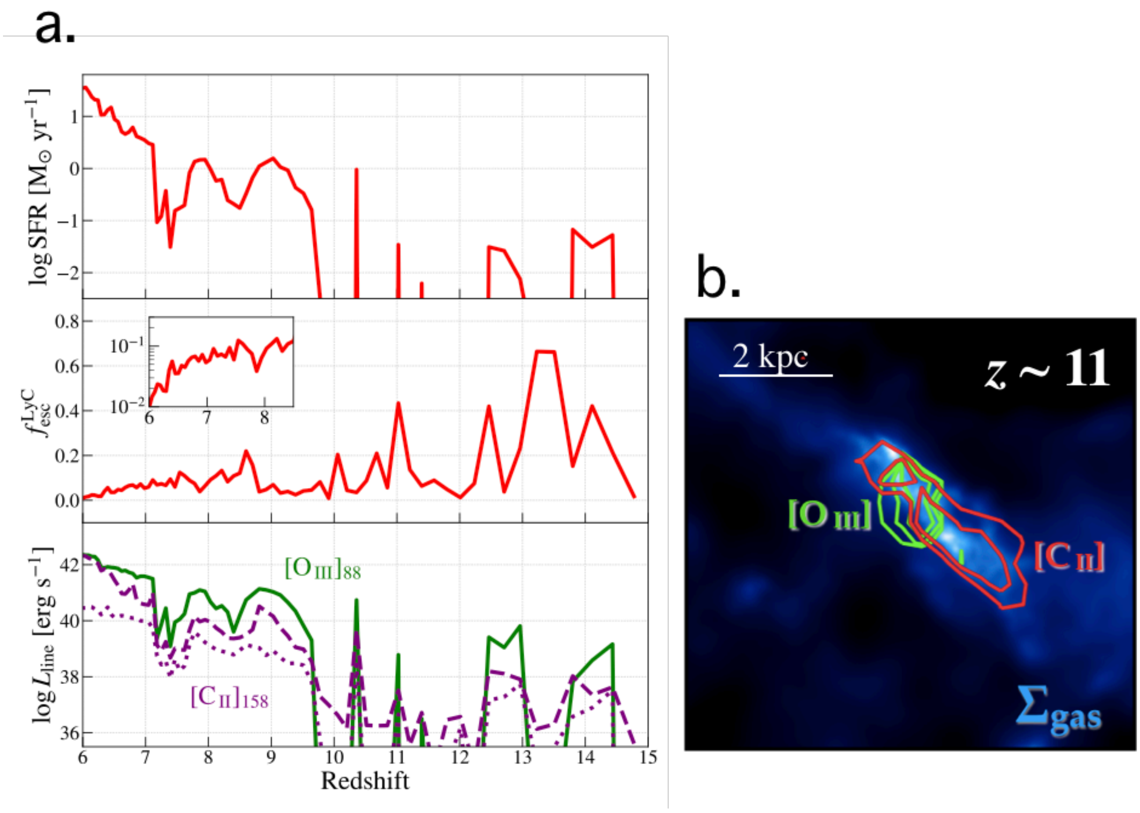

Figure 3.6: **(a)** Redshift evolution of star formation rate (top panel), escape fraction of LyC photons (middle panel) and luminosities of [O III] 88 μm and [C II] 158 μm lines (bottom panel) for Halo-11. Inserted figure in the middle panel closes up $f_{\rm esc}^{\rm LyC}$ at $z = 6 - 8.5$ in log-scale. The dotted line in the bottom panel represents the contribution from H II regions. **(b)** Composite maps of gas surface density (blue), [O III] and [C II] surface brightness (green and red) for Halo-11 at $z \sim 11$. (Modified from Arata et al., 2020)

that efficiently absorb LyC photons, resulting in low escape fraction. Ma et al. (2015) suggested that the escape fraction of LyC photons could be overestimated if the threshold density for star formation was $n_{\rm th} < 1\,{\rm cm^{-3}}$. Our threshold density ($n_{\rm th} = 10\,{\rm cm^{-3}}$) satisfies this condition.

The bottom panel shows evolution of metal-line luminosities of [O III] 88 μm and [C II] 158 μm lines. The [O III] line is emitted only in star-burst phases, because O^{2+} ions exist in H II regions formed by massive stars. $L_{[O\,III]}$ fluctuates between $\sim 10^{40} - 10^{42}\,{\rm erg\ s^{-1}}$ at $z = 6 - 10$. Meanwhile, [C II] is continuously emitted from H I regions even in outflowing phases. The contribution from H II regions to total luminosity (dotted line) increases in star-burst phases, but does not exceed 50 % over all redshift.

At $z = 11$, gas structure of Halo-11 becomes filamentary, and star formation occurs in the knots as shown in Fig. 3.6b. The propagation of LyC photons is interrupted in parallel direction to the filament, but efficiently escape from perpendicular direction ($f_{\rm esc}^{\rm LyC} \sim 40\,\%$). As described above, the [O III] and [C II] lines are emitted from ionized regions (knots) and neutral gas (filament), respectively. Thus we suggest that combining [O III] and [C II] observations, we will obtain the neutral and ionized gas distribution in sources of reionization.

3.4 Comparison with Observations

3.4.1 Duty Cycle and Observability

As described above, the SED of a high-z galaxy rapidly changes UV- and IR- bright phases. Here we discuss detection probability for the first galaxies in sub-mm wavelength, which is directly related to the duration of IR-bright phases. As a relevant work, Jaacks et al. (2012b) studied observability of high-z galaxies in UV wavelength with cosmological hydrodynamic simulations. They defined the *'duty cycle'* as a ratio of timescale in which a galaxy is brighter than the detection limit of HST to total timescale of bursty star formation history.

We define the duty cycle ($f_{\rm duty}$) as a ratio of the number of galaxies whose sub-mm fluxes are higher than the detection threshold ($S_{\rm th}$) to the total number:

$$f_{\rm duty} \equiv \frac{N(S > S_{\rm th})}{N_{\rm tot}}. \qquad (3.10)$$

We use galaxy samples of Halo-11, Halo-12 and the satellite galaxies in their zoom-in boxes. We set mass limits of the satellites to $M_{\rm h} > 10^8\,{\rm M_\odot}$ for Halo-11 and $M_{\rm h} > 10^9\,{\rm M_\odot}$ for Halo-12, respectively, corresponding to $\sim 10^3$ DM particles to identify as a halo. The number of galaxies at each snapshot are 613, 593, 564 & 351 at $z \approx 6,\ 7,\ 8$ & 10, respectively.

We first present the distribution of sub-mm fluxes for all samples as a function of the halo masses in left of Figure 3.7. As redshift decreases, the haloes associate each other and grow in their masses, resulting in that the massive end of the distribution shifts to right. The sharp cut-off at the low-mass end of the distribution of yellow triangles (satellite galaxies in Halo-12 zoom box) are due to the halo mass limit described above. The sub-mm flux steeply increases with halo mass, because more massive haloes tend to have higher SFRs and lower $f_{\rm esc}^{\rm UV}$. At a specific halo mass of $M_{\rm h} \sim 10^{10}\,{\rm M_\odot}$, there is a large scatter in sub-mm fluxes due to the varieties of dust distribution affected by SNe. However, the scatter becomes small with increasing halo mass because SNe become inefficient to eject gas from the central regions.

Fig. 3.7b shows $f_{\rm duty}$ as a function of halo mass. At each redshift, we separate the galaxies into halo mass bins with the bin size of $\Delta \log{(M_{\rm h}/{\rm M_\odot})} = 0.5$ and derive $f_{\rm duty}$ for 850 μm in each bin. Upper and lower panels present $f_{\rm duty}$ for the detection thresholds of $S_{\rm th} = 0.1$ and 0.01 mJy (upper and lower dashed lines in Fig. 3.7a), which corresponds to 10σ detection with 20 min and 40 h observations by ALMA Band-7 full operation, respectively. In the case of $S_{\rm th} = 0.1$ mJy, $f_{\rm duty}$ exceeds 0.5 only for massive haloes with $\log{(M_{\rm h}/{\rm M_\odot})} \geq 11$ at $z \leq 7$, and it changes with redshift only at the massive end. This result is consistent with the observational facts (e.g. Hashimoto et al., 2019). Note that, however, we have small number of samples at $M_{\rm h} > 10^{11}\,{\rm M_\odot}$ ($N \lesssim 10$), thus the estimation of $f_{\rm duty}$ at the massive end is likely to contain large uncertainties. In the case of $S_{\rm th} = 0.01$ mJy, $f_{\rm duty}$ steeply increases at lower halo mass and becomes 0.5 at $\log{(M_{\rm h}/{\rm M_\odot})} \approx 10.5$ at $z \lesssim 8$. Therefore deep observations that can observe down to 0.01 mJy will be able to detect the sub-mm fluxes from low-mass galaxies. (Jaacks et al., 2012b) also showed rapid increase of $f_{\rm duty}$ for UV observations, and it shifted to higher mass side by $\log{M_\star/{\rm M_\odot}} = 0.5$ due to dust attenuation. Our results suggest that sub-mm observations compensate undetected dust-obscured galaxies in UV wavelength.

Using results of $f_{\rm duty}$, we predict the number density of observable sub-mm sources at high-z. By integrating the Sheth & Tormen (2002) halo mass function multiplied by $f_{\rm duty}(z, M_{\rm h})$, we can roughly estimate it with a certain threshold value of observed flux $S_{\rm th} = 0.1,\ 0.01$ mJy, as shown in Figure 3.8. In the case of $S_{\rm th} = 0.01$ mJy, the number density increases with decreasing redshift, and becomes $5.4 \times 10^{-3}\,{\rm cMpc^{-3}}$ at $z \sim 6$, which is close to that of LBGs identified by UV photometric survey at the same redshift (Ouchi et al., 2010; Bouwens et al., 2015). Therefore, we suggest that deep sub-mm observations can detect even typ-

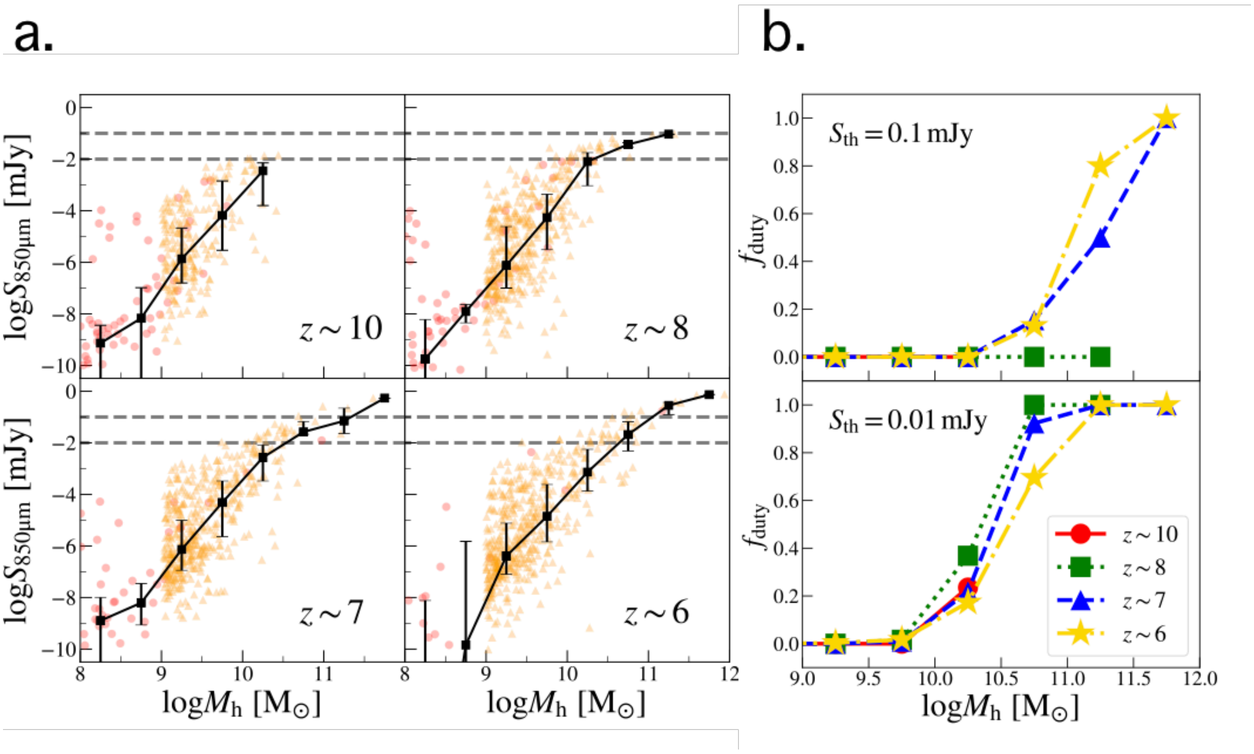

Figure 3.7: (a) The sub-mm fluxes for all main and satellite galaxies in Halo-11 (red circles) and Halo-12 (yellow triangles) at $z \approx 10,\ 8,\ 7$ & 6. Black squares and errorbars shows the medians and quantiles with the bins of $\Delta \log{(M_{\rm h}/{\rm M}_{\odot})} = 0.5$. Dashed lines represent the detection thresholds of 0.1 mJy and 0.01 mJy at 850 μm. **(b)** Duty cycle ($f_{\rm duty}$), which is defined by number fraction of observable galaxies to the total samples in each mass bin, is plotted against the halo mass. The top panel shows $f_{\rm duty}$ for the detection threshold of 0.1 mJy at 850 μm. This corresponds to 10σ detection by the ALMA observation with 20 min integration with full operation. The bottom panel represents the case of $S_{\rm th} = 0.01$ mJy which corresponds to 10σ detection with 40 hours integration. (Modified from Arata et al., 2019)

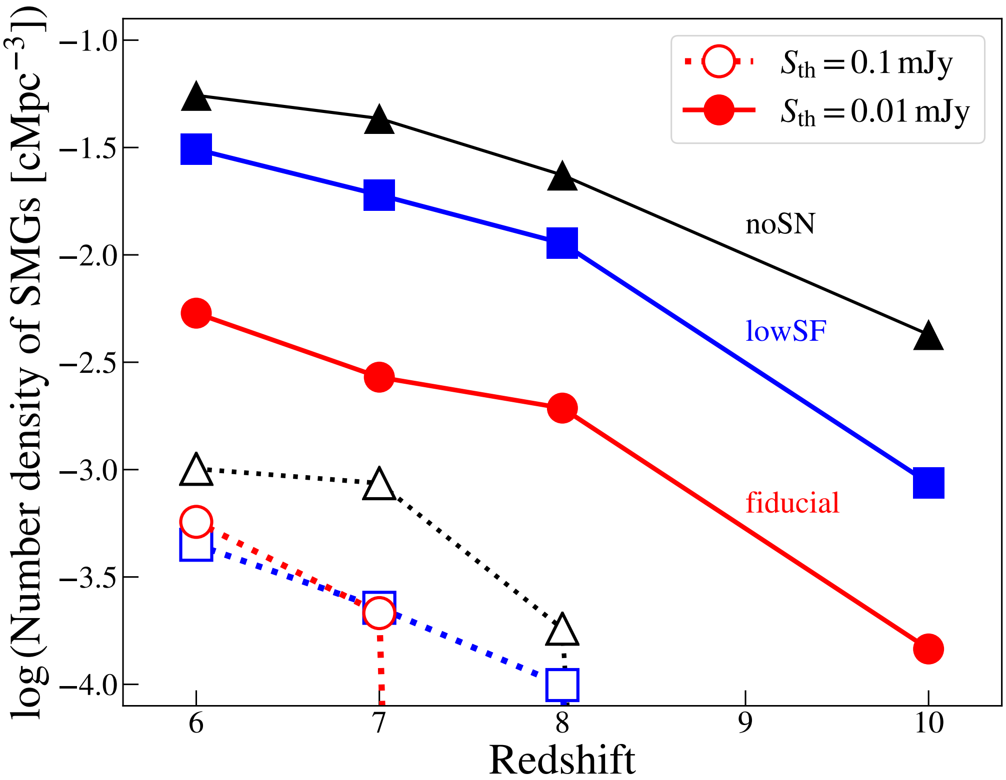

Figure 3.8: Number density (comoving unit) of observable sub–mm sources as a function of redshift, which is estimated by integrating the halo mass function of Sheth & Tormen (2002) multiplied by $f_{\rm duty}$. The solid and dotted lines represent the predicted number density for the detection thresholds of $S_{\rm th} = 0.01$ and 0.1 mJy at 850 μm, respectively. Different colors represent different models: fiducial runs (red circles), low–SF runs (blue squares) and no–SN runs (black triangles). (Modified from Arata et al., 2019)

ical LBGs. The gravitational lensing effect magnifies observed luminosity about factor of 10 (Watson et al., 2015; Hashimoto et al., 2018), which might increase our prediction. On the other hand, the number density is $\sim 6 \times 10^{-4}\,{\rm cMpc}^{-3}$ in the case of $S_{\rm th} = 0.1$ mJy. As shown in Fig.3.7a, there is no galaxies with the flux of > 0.1 mJy at $z \gtrsim 8$. Note that again, our simulation sample is quite limited, and more precise prediction needs larger box-size simulations.

Here we compare the results of the cases with a lower star-formation efficiency parameter (Halo-11-lowSF and Halo-12-lowSF) and without SN feedback (Halo-11-noSN and Halo-12-noSN), and study how the observability prediction changes with sub-grid models. In the low-SF case, we set a lower value for coefficient of the

Kennicutt–Schmidt relation (A) than that of the fiducial case, which induces higher gas density (see also, Yajima et al., 2017b). More details of comparison between sub-grid models are described in Section 3.7. In the no-SN runs, galaxies are not suffered from energy release of SNe, and SFR proceeds continuously. Dusty gas heavily covers the central star-forming regions, resulting in a lower escape fraction than that of fiducial run. The rapid increase of $f_{\rm duty}$ with the detection threshold of $S_{\rm th} = 0.01\,{\rm mJy}$ exceeds 0.5 at $\log(M_{\rm h}/{\rm M}_\odot) = 9.5$ at $z \sim 7$. The number density of sub-mm sources is much high and reaches $5.5 \times 10^{-2}\,{\rm cMpc}^{-3}$ at $z = 6$. In low-SF cases, gas density tends to be higher than fiducial runs, which induces rapid cooling of released energy of SNe. As a result, star formation proceeds continuously and becomes bright in sub-mm wavelength. The point of $f_{\rm duty} = 0.5$ with $S_{\rm th} = 0.01\,{\rm mJy}$ appears at $\log(M_{\rm h}/{\rm M}_\odot) = 10$ which is intermediate value between fiducial and no-SN cases. Also the number density is $3.2 \times 10^{-2}\,{\rm cMpc}^{-3}$ at $z = 6$. We suggest that a future deep survey of sub-mm galaxy with a detection threshold of $S_{\rm th} = 0.01\,{\rm mJy}$ could be able to constrain the models of star formation and stellar feedback by comparing observations with theoretical models.

The impact of sub-grid models on star formation and feedback has also been studied by comparing with the observations of local galaxies (e.g., Okamoto et al., 2014; Schaye et al., 2015; Pillepich et al., 2018). They showed that the SN feedback model should be tuned to reproduce the stellar mass function (Crain et al., 2015). On the other hand, the star formation model may not change the star formation history significantly. Schaye et al. (2010) showed that the cosmic SFR density was insensitive to the star formation parameter 'A' in equation (2.9). As in Fig. 3.19, our simulations also showed that the difference of SFR between Halo-11 and Halo-11-lowSF becomes small at $z \lesssim 8$. Note that, however, the number density of faint sub-mm sources of low-SF runs is higher than that of fiducial runs by a factor $\sim 2-3$ even at $z \lesssim 8$ due to different distribution of dusty gas. Therefore, we suggest that the comparisons between theoretical models and the observations of sub-mm sources can be a complementary tool to study the validity of star formation models.

3.4.2 IR Luminosity vs. SFR

In general, the IR luminosity increases with SFR because young stars dominantly generate the UV photons which are absorbed and reprocessed by dust. Figure 3.9 shows the relation between IR luminosity and SFR at $z \sim 7$ using all of galaxies in Halo-11 and Halo-12 zoom-in boxes. We find that the distribution of our samples has a large dispersion at low SFR (SFR $\lesssim 0.1\,{\rm M}_\odot\ {\rm yr}^{-1}$) due to the fluctuation of $f_{\rm esc}^{\rm UV}$. Meanwhile, the massive galaxies have low $f_{\rm esc}^{\rm UV}$ (see Fig. 3.4), resulting in the small dispersion at higher SFR. Using the least-square fitting, we derive the power-law fit for $z \sim 7$ galaxies with $-4 < \log_{10} \mathrm{SFR}\,[\mathrm{M}_\odot\ \mathrm{yr}^{-1}] < 3$:

$$\log\left(L_{\mathrm{IR}}\,[\mathrm{L}_\odot]\right) = 9.5 + 1.21 \log\left(\mathrm{SFR}\,[\mathrm{M}_\odot\ \mathrm{yr}^{-1}]\right). \tag{3.11}$$

If UV light is completely absorbed by dust, the slope must be unity because UV luminosity relates to SFR linearly (Kennicutt, 1998). For low-mass galaxies, the escape fraction tends to be high due to SN feedback, resulting in the steep slope. The relation can reproduce the observed LBGs at $z \sim 7-8$ remarkably well, whose SFRs were measured from the UV and IR luminosities. As the detection limit becomes lower, we should take care that the detection is biased to low-$f_{\mathrm{esc}}^{\mathrm{UV}}$ galaxies. In addition, non-star-forming galaxies (which do not appear in this figure) also have large dispersion due to the dust absorption of UV photons emitted by residual young stars.

3.4.3 Metal-line Luminosity vs. SFR

In Section 3.3.3, we showed that metal-line luminosity fluctuates with intermittent star formation using our fiducial run. Here we focus on the statistical trend. Figures 3.10 present relations between [O III] and [C II] luminosities and SFR for Halo-11 (red circles), Halo-12 (blue squares), MHaloes and LHaloes (green stars) at $z = 9$, 8, 7 & 6 (lighter to darker). Our simulations have a good agreement with observed galaxies at $z \gtrsim 6$. In particular, Halo-12 shows $L_{[\mathrm{O\,III}]} = 2.3 \times 10^9\,\mathrm{L}_\odot$, $L_{[\mathrm{C\,II}]} = 1.7 \times 10^9\,\mathrm{L}_\odot$, and $L_{\mathrm{IR}} = 6.9 \times 10^{11}\,\mathrm{L}_\odot$ at $z = 7$, which are remarkably consistent with B14-65666 at $z = 7.15$ ($L_{[\mathrm{O\,III}]} = 2.9 \times 10^9\,\mathrm{L}_\odot$, $L_{[\mathrm{C\,II}]} = 1.3 \times 10^9\,\mathrm{L}_\odot$, and $L_{\mathrm{IR}} = 6.2 \times 10^{11}\,\mathrm{L}_\odot$) as reported by Hashimoto et al. (2019). Also we compare our results with the relation of local galaxies derived in De Looze et al. (2014). They investigated low-metal galaxies in the range of $-3 \lesssim \log \mathrm{SFR}\,[\mathrm{M}_\odot\ \mathrm{yr}^{-1}] \lesssim 2$ from the *Herschel* Dwarf Galaxy Survey. Our simulations are similar to metal-poor dwarf galaxies (dot-dashed line) rather than local starburst galaxies (dotted line). This is opposite argument against other simulation studies (Olsen et al., 2017; Katz et al., 2019), but similar with Moriwaki et al. (2018). The chemical abundance pattern of galaxies at $z > 6$ is dominated by Type-II SNe, and quite different from solar-neighbourhood (Maiolino et al., 2004). In the calculation of [O III] luminosity, we use oxygen abundance of each gas particle, which is the same as Moriwaki et al. (2018) but not Olsen et al. (2017) and Katz et al. (2019). The oxygen abundance (mass-weighted mean) of Halo-12 evolves from $12 + \log(\mathrm{O/H}) = 6.6$ at $z = 9$ to 8.9 at $z = 6$, and the range is close to that of local relation of $12 + \log(\mathrm{O/H}) = 7.14 - 8.43$ (De Looze et al., 2014). Thus we suggest that the physical state of ISM in the first galaxies might be similar to that of local dwarf galaxies.

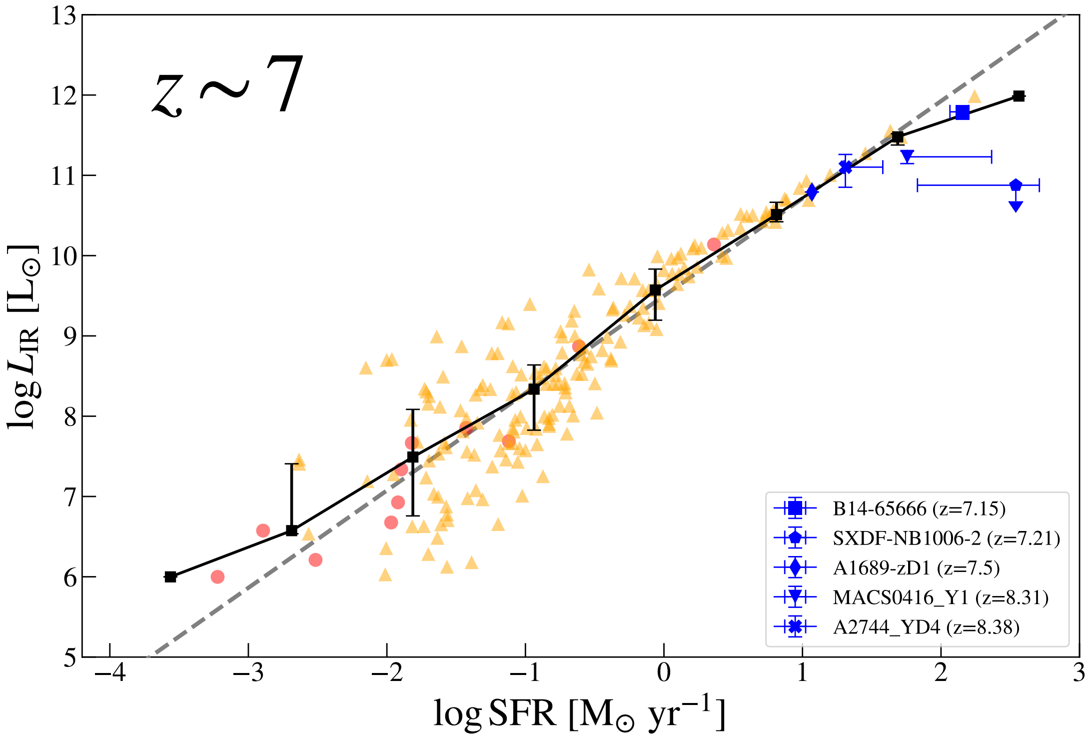

Figure 3.9: Relation between bolometric IR luminosity and SFR. The red circles and yellow triangles represent main galaxies and the satellites in Halo-11 and Halo-12 zoom-in boxes at $z \sim 7$, respectively. The black squares and errorbars shows the medians and quantiles with the bins of $\Delta \log(\mathrm{SFR}/\mathrm{M}_\odot\ \mathrm{yr}^{-1}) = 1.0$. The gray dashed line shows the fitting function for galaxies with $-4 < \log(\mathrm{SFR}/\mathrm{M}_\odot\ \mathrm{yr}^{-1}) < 3$. The blue symbols represent high-z observations (Watson et al., 2015; Inoue et al., 2016; Laporte et al., 2017; Hashimoto et al., 2019; Tamura et al., 2019). (Modified from Arata et al., 2019)

From the least-square fitting to all samples (Halo-11, Halo-12, MHaloes, LHaloes) at $z = 6 - 9$, we derive the following relations:

$$\log(L_{[\mathrm{O_{III}}]}\,[\mathrm{L}_\odot]) = 7.23 + 1.04 \log(\mathrm{SFR}\,[\mathrm{M}_\odot\ \mathrm{yr}^{-1}]), \tag{3.12}$$

$$\log(L_{[\mathrm{C_{II}}]}\,[\mathrm{L}_\odot]) = 6.38 + 1.47 \log(\mathrm{SFR}\,[\mathrm{M}_\odot\ \mathrm{yr}^{-1}]). \tag{3.13}$$

We find that [O III] luminosity is linearly proportional to SFR, because most of ionizing photons are absorbed by gas ($f_{\rm esc}^{\rm LyC} \lesssim 0.1$) for all of the galaxies. These fittings nicely match the observed results of Harikane et al. (2019). They showed the slope of the $L_{[\mathrm{O_{III}}]}$–SFR relation for $z = 6-9$ galaxies is 1.1, and 1.5 for the $L_{[\mathrm{C_{II}}]}$. The simulated $L_{[\mathrm{O_{III}}]}$–SFR relation at high-z is very close to the relation for local metal-poor dwarf galaxies, while the slope of $L_{[\mathrm{C_{II}}]}$–SFR relation is steeper than

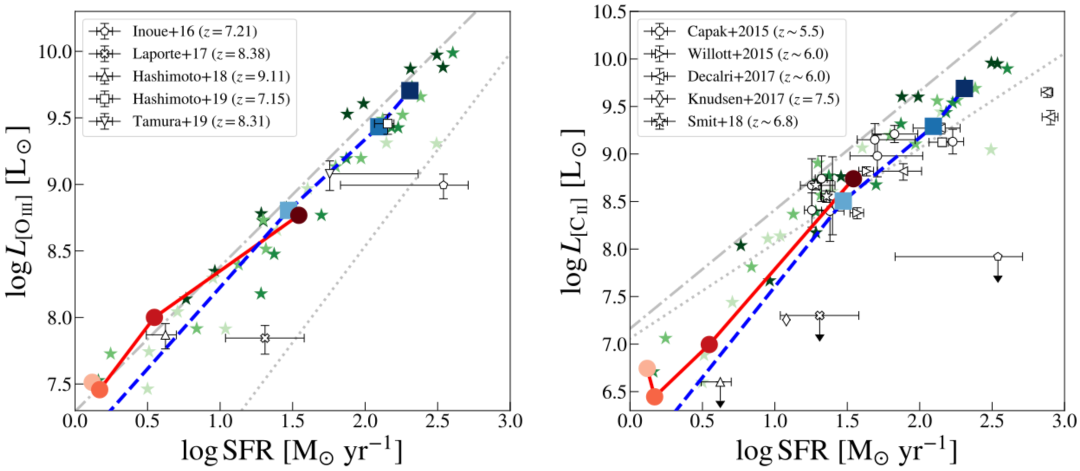

Figure 3.10: Relation between SFR and [O III] luminosity (left panel) or [C II] luminosity (right panel). Red circles and solid line represent evolution of Halo-11 at z = 9, 8, 7 & 6 (lighter and darker), and blue squares and dashed line are for Halo-12. Green stars represent MHaloes and LHaloes at $z = 6 - 9$. The Open symbols represent observed high-z galaxies. Gray dotted line and dot-dashed line show the relation for local starburst galaxies and metal-poor dwarf galaxies, respectively. (Modified from Arata et al., 2020)

local ones (1.0 for starburst galaxies and 1.25 for metal-poor galaxies, De Looze et al., 2014). The physical reason of the steepness is described below. In addition, these results are also supported by a more statistical study using semi-analytical simulations (Lagache et al., 2018).

3.4.4 [O III] and [C II] Luminosity Ratio

Here we focus on the luminosity ratio of [O III] to [C II] lines. Hashimoto et al. (2019) suggested the negative correlation between $L_{[\mathrm{O\,III}]}/L_{[\mathrm{C\,II}]}$ and bolometric luminosity L_{bol} for galaxies at $z > 6$, in range of $10^{10}\,\mathrm{L}_\odot < L_{\mathrm{bol}} < 10^{14}\,\mathrm{L}_\odot$ (see also Marrone et al., 2018). These lines are emitted from different gas phases, thus the luminosity ratio can reflect the multi-phase ISM structure (e.g. Cormier et al., 2012). Cormier et al. (2015) found the same trend in local star-forming galaxies, and suggested that it depended on gas metallicity. We here suggest that the origin of the negative correlation of high-z galaxies is the carbon enrichment by AGB stars.

Figure 3.11 shows the $(L_{[\mathrm{O\,III}]}/L_{[\mathrm{C\,II}]})$–$L_{\mathrm{bol}}$ relation for all samples (Halo-11, Halo-12, MHaloes and LHaloes) at $z = 6 - 9$, where L_{bol} is measured from $L_{\mathrm{UV}} + L_{\mathrm{IR}}$. We find that $L_{[\mathrm{O\,III}]}/L_{[\mathrm{C\,II}]}$ ratio decreases from $\sim$ 10 to $\sim$ 1 in the range of $10 \lesssim \log\,(L_{\mathrm{bol}}\,[\mathrm{L}_\odot]) \lesssim 12$ with increasing metallicity from $\sim 0.1\,\mathrm{Z}_\odot$ to $\sim 1\mathrm{Z}_\odot$. Also

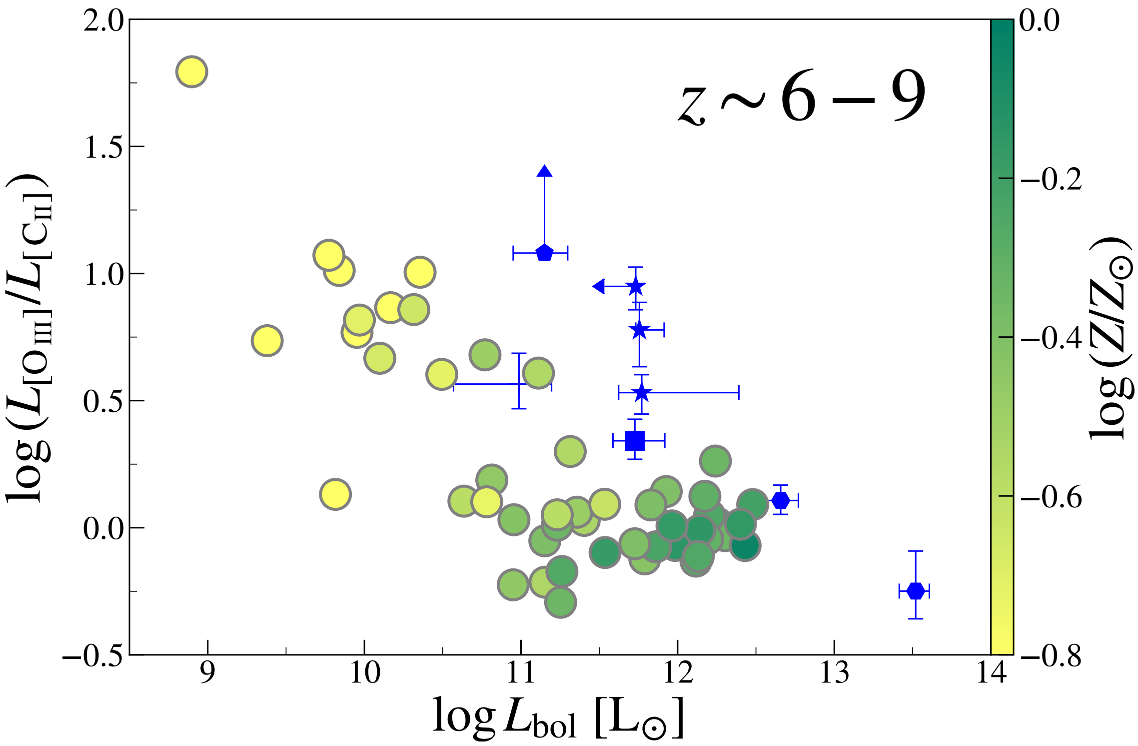

Figure 3.11: Relation between the bolometric luminosity ($L_{\mathrm{bol}} = L_{\mathrm{UV}} + L_{\mathrm{IR}}$) and the line luminosity ratio. The filled circles represent simulated galaxies at $z = 6-9$ colored by their gas metallicity. The blue symbols represent high-z observations (Inoue et al., 2016; Carniani et al., 2017; Marrone et al., 2018; Hashimoto et al., 2019; Harikane et al., 2019).

the $\log(L_{[\mathrm{C_{II}}]}/\mathrm{SFR}\,[\mathrm{L_\odot/M_\odot\ yr^{-1}}])$ increases from 6.1 to 7.8, while $\log(L_{[\mathrm{O_{III}}]}/\mathrm{SFR})$ is constant ($\sim 7.25 \pm 0.25$). The chemical abundance in the first galaxies is initially dominated by Type-II SNe which efficiently enriches oxygen more than carbon, and has higher O/C ratio. As the galaxy evolves, low- and intermediate-mass stars begin to eject carbon-rich winds by dredge-up events of AGB phases (see also, Berg et al., 2019). As a result, the $\log(\mathrm{O/C})$ decreases from ~ 0.9 to ~ 0.5 when metallicity increases from $\sim 0.1\,\mathrm{Z_\odot}$ to $\sim 1\mathrm{Z_\odot}$, and $L_{[\mathrm{O_{III}}]}/L_{[\mathrm{C_{II}}]}$ ratio decreases. To confirm the validity of this scenario, we use the Chemical Evolution Library (CELib, Saitoh, 2017), and compute $\log(\mathrm{O/C})$ in a star-forming cloud with $Z = 0.1\,\mathrm{Z_\odot}$ assuming the Chabrier IMF. The $\log(\mathrm{O/C})$ decreases from ~ 1.0 to ~ 0.5 when the age exceeds ~ 0.5 Gyr which corresponds to half of the cosmic time at $z \sim 6$. This result supports our simulation results.

Our simulations are in good agreement with high-z observations (Inoue et al., 2016; Carniani et al., 2017; Marrone et al., 2018; Hashimoto et al., 2019; Harikane et al., 2019). Note that our treatment of [C II] emission predicts the upper limit of the luminosity (Sec. 2.3.2), thus the simulated luminosity ratio might somewhat increase in more sophisticated models. The dependence on metallicity is also consistent with the local trend (Cormier et al., 2015), however our $L_{[\mathrm{O_{III}}]}/L_{[\mathrm{C_{II}}]}$ ratio at a specific L_{bol} is ~ 10 times higher than the local relation. Our samples have high ionization parameter ($-2.2 \lesssim \log U \lesssim -1.5$) and high volume fraction of H II regions ($0.64 \lesssim f_{\mathrm{H_{II}}} \lesssim 1.0$). Using CLOUDY models, Harikane et al. (2019) suggested that galaxies with high-U and low-C_{PDR} (covering fraction of PDR) can explain higher $L_{[\mathrm{O_{III}}]}/L_{[\mathrm{C_{II}}]}$ ratio than local galaxies. Our results are consistent with their picture of first galaxies.

Figure 3.12 describes more details of redshift evolution of $L_{[\mathrm{O_{III}}]}/L_{[\mathrm{C_{II}}]}$ ratio. The top panel shows that $L_{[\mathrm{O_{III}}]}/L_{[\mathrm{C_{II}}]}$ ratio largely fluctuates with intermittent star formation in case of Halo-11 (blue line). But it gradually decreases with decreasing redshift mainly due to carbon enrichment by AGB stars (second panel). The third panel shows volume fraction of H II regions, which relates to fluctuation of $f_{\mathrm{esc}}^{\mathrm{LyC}}$. In star-burst phases, $f_{\mathrm{H_{II}}}$ increases to $\gtrsim 0.7$. The bottom panel shows that the gas metallicity in the halo gradually increases from $z \sim 10$, because a part of metal-enriched gas ejected by SN feedback can fall back due to gravitational potential.

We also compare $L_{[\mathrm{O_{III}}]}/L_{[\mathrm{C_{II}}]}$ ratio with that of low-SF (green dotted) and no-SN (red dashed) cases. The SFR in low-SF case is similar to fiducial case by the self-regulation due to SN feedback, but gas density tends to be higher. The rapid recombination suppresses extending H II regions, resulting in lower $f_{\mathrm{H_{II}}}$. The high density also makes SN feedback inefficient due to radiative cooling, thus the metal enrichment proceeds earlier. These factors lead to very low $\log(L_{[\mathrm{O_{III}}]}/L_{[\mathrm{C_{II}}]})$ (~ -2 at $z < 10$) in low-SF case. On the other hand, the no-SN case has similar gas density to fiducial case, thus $f_{\mathrm{H_{II}}}$ takes similar value. However, SN feedback does not evacuate gas from the halo in no-SN case, resulting in rapid growth of metals. As a result, $\log(L_{[\mathrm{O_{III}}]}/L_{[\mathrm{C_{II}}]})$ takes stably lower value (~ -0.5).

3.4.5 $(L_{\mathrm{line}}/L_{\mathrm{IR}}) - L_{\mathrm{IR}}$ Relations

In addition to the ionization of hydrogen and metals, UV radiation from young stars also heats up dust, resulting in IR thermal emission. Therefore, both metal-line and IR luminosities are likely to be related with SFR. The luminosity ratio reflects the ratio of absorbed energy of ionizing photons between gas and dust. The local observations showed that $L_{[\mathrm{O_{III}}]}/L_{\mathrm{IR}}$ and $L_{[\mathrm{C_{II}}]}/L_{\mathrm{IR}}$ decreased as L_{IR} increased (De Looze et al., 2014; Cormier et al., 2015; Díaz-Santos et al., 2014). Cormier et al. (2015) pointed out that extended dwarf galaxies had higher $L_{[\mathrm{O_{III}}]}/L_{\mathrm{IR}}$ and suggested the larger volume fraction of ionized regions. In addition, recent observations suggested

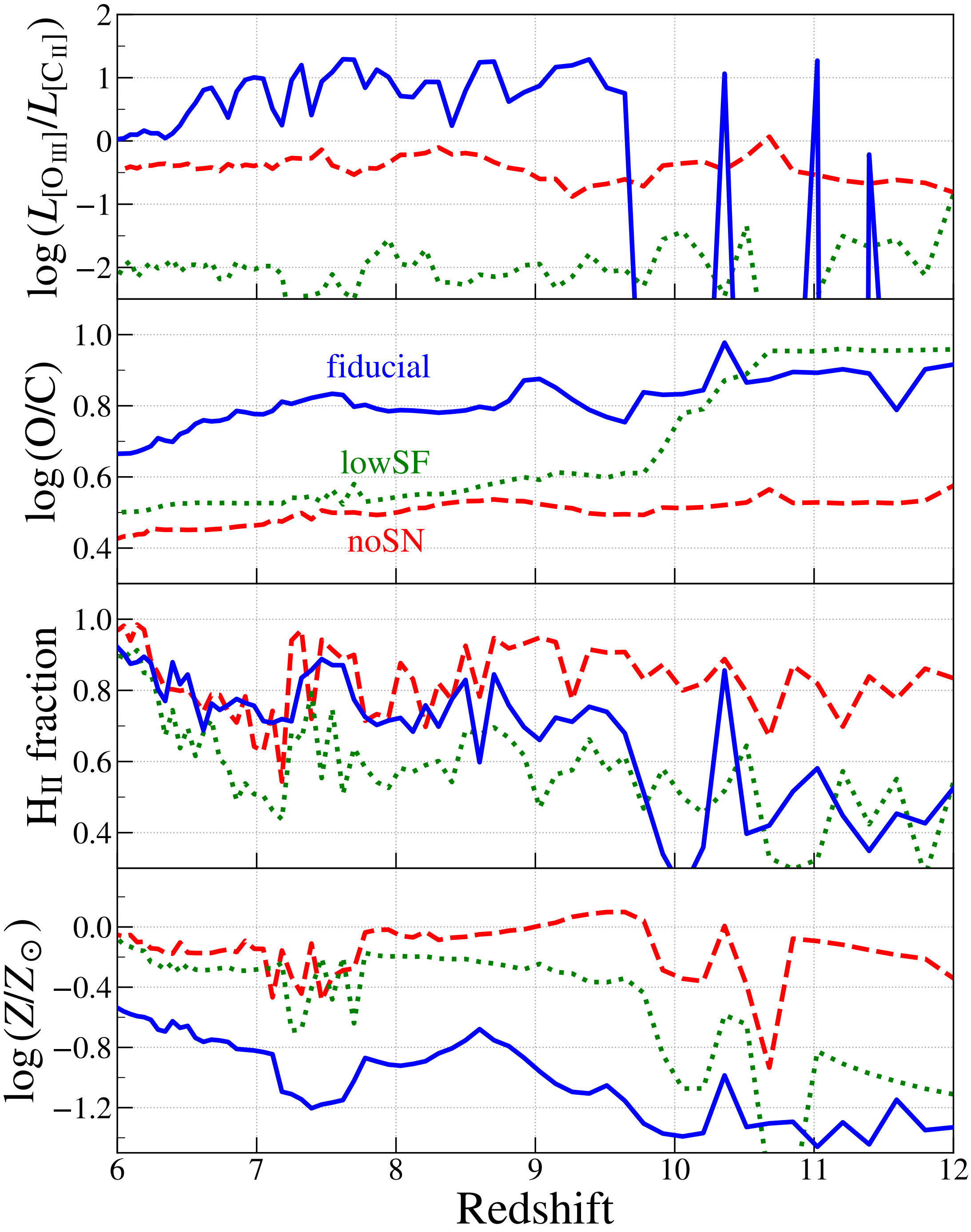

Figure 3.12: Redshift evolution of line luminosity ratio (top), O/C abundance ratio (second), volume fraction of H II regions (third), and total gas metallicity (bottom) in Halo-11 (blue solid), Halo-11-lowSF (green dotted) and Halo-11-noSN (red dashed) runs.

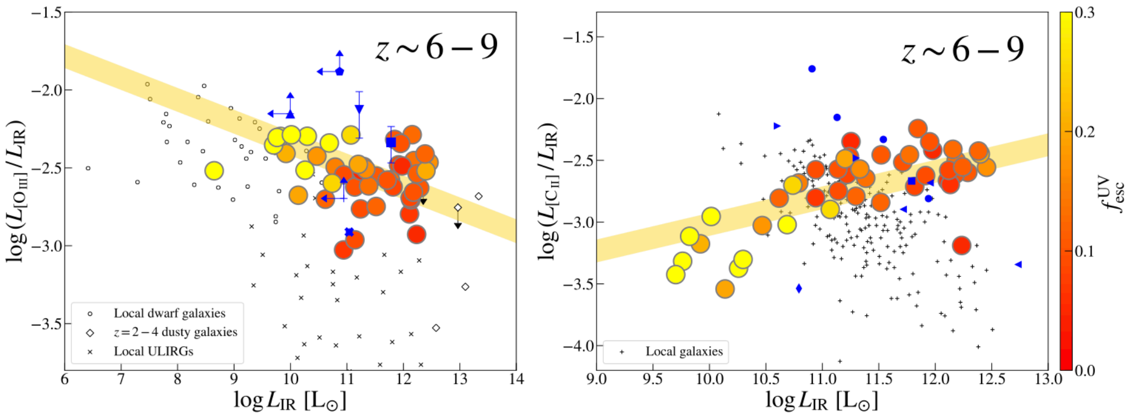

Figure 3.13: Relation between luminosity ratio $L_{[\mathrm{O_{III}}]}/L_{\mathrm{IR}}$ and total IR luminosity L_{IR}. Filled circles represent our simulation samples at $z = 6 - 9$. The color is scaled by escape fraction of UV photons. Thick yellow line shows combination of our fitting functions (Eq. 3.11, 3.12 and 3.13). Open small circles represent local dwarf galaxies (Madden et al., 2013; Cormier et al., 2015). Open diamonds are for dusty star-forming galaxies at $z \sim 2 - 4$ (Ferkinhoff et al., 2010; Ivison et al., 2010a; Valtchanov et al., 2011; Vishwas et al., 2018). Small crosses are for from local spiral galaxies to ULIRGs (Herrera-Camus et al., 2018a,b). Blue symbols are for $z \gtrsim 6$ galaxies

the similar trend but a factor of higher value in high-z galaxies (e.g. Tamura et al., 2019). Here we study the origin of the correlations in $(L_{\mathrm{line}}/L_{\mathrm{IR}})$–$L_{\mathrm{IR}}$ relations.

Left panel of Figure 3.13 shows the relation between $L_{[\mathrm{O_{III}}]}/L_{\mathrm{IR}}$ and L_{IR} at $z \approx 6 - 9$. There is a weak negative correlation that is consistent with local star-forming galaxies, $z \sim 2 - 4$ dusty star-forming galaxies and ultra-luminous infrared galaxies (ULIRGs). At $z < 10$, most of the ionizing photons are absorbed by the gas even in less massive galaxies, resulting in a low escape fraction ($f_{\mathrm{esc}}^{\mathrm{LyC}} \lesssim 0.1$, see Fig. 3.6) and a linear $L_{[\mathrm{O_{III}}]}$–SFR relation (equation 3.12). Meanwhile, UV continuum photons can escape through the direction of low dust column density in the outflowing phases ($\tau_{\mathrm{UV}} \lesssim 1$). We find that the negative correlation is closely related to the escape fraction of UV photons. Combining Eq. (3.12) and (3.11), we plot the thick yellow band on the figure. It reproduces our simulation results and observations of high-z galaxies. In addition, our galaxies have high volume fraction of H II regions ($0.7 < f_{\mathrm{H_{II}}} < 1$), which is responsible for higher $L_{[\mathrm{O_{III}}]}/L_{\mathrm{IR}}$ than in local star-forming galaxies at a specific L_{IR}.

Right panel of Fig. 3.13 shows $(L_{[\mathrm{C_{II}}]}/L_{\mathrm{IR}})$–$L_{\mathrm{IR}}$ relation. The thick yellow band indicates the combination of Eq. (3.13) and (3.11). It increases with L_{IR} because

$L_{[\mathrm{C\,II}]}$–SFR relation has the steeper slope (~ 1.5) than that of the L_{IR}–SFR relation (~ 1.2). Our simulations match the model nicely. However, the luminosity ratios of observed galaxies decreases with increasing L_{IR} unlike in our simulations. This discrepancy can be explained by the dust effect. Luhman et al. (2003) suggested that dust in H II regions efficiently absorbs UV photons, resulting in inefficient photo-electric heating of polycyclic aromatic hydrocarbons (PAHs) in PDRs (so-called 'dust-bounded model'). The [C II] cooling whose function monotonically increases with temperature and thermally balances with the heating [3] also becomes inefficient. Also, if the dust is positively charged, the photo-electric heating and [C II] cooling can be suppressed (Wolfire et al., 1990; Luhman et al., 2003). Combining [C II] 158 μm and CO (3-2) observations at $z \sim 3$, Rybak et al. (2019) suggests that C^+ level populations are saturated in high-temperature ISM due to a strong UV radiation field, which induces the [C II] deficit (Muñoz & Oh, 2016). As described in Sec. 2.2, we assume the low dust-to-gas mass ratio in H II cells considering dust destruction in ionized gas. Also, our model does not consider the dust charge. These can be the reasons for differences between our simulations and observations.

3.5 Dust Properties

3.5.1 Typical Dust Temperature at High-redshift

The dust temperature is an important for estimating the bolometric infrared luminosity, but it has not been estimated well for the first galaxies due to limited observational data so far (e.g. Harikane et al., 2019). In observations of local galaxies in infrared wavelength, the fluxes at some different frequencies can be detected, and the dust temperature is determined from the peak wavelength of modified black-body spectrum (e.g. Hwang et al., 2010). On the other hand, most of the ALMA observations of high-z galaxies have obtained the flux only at one wavelength (Tamura et al., 2019). Therefore, the physical properties e.g., the dust mass or SFR have been estimated based on the assumed dust temperature referring local galaxies (e.g. ~ 40 K, Watson et al., 2015). Here we investigate the typical dust temperature of first galaxies.

We showed the projected map of dust temperature in Fig. 3.1. To describe it

[3] The cooling function of [C II] and O I radiation is given by (Koyama & Inutsuka, 2002; Arata et al., 2018)

$$\frac{\Lambda(T)}{\Gamma} = 1.4 \times 10^{-2} \sqrt{T} \exp\left(\frac{-92}{T}\right) \mathrm{cm}^3, \tag{3.14}$$

where $\Gamma = 2.0 \times 10^{-26}$ erg s^{-1} is the photo-electric heating rate of PAHs.

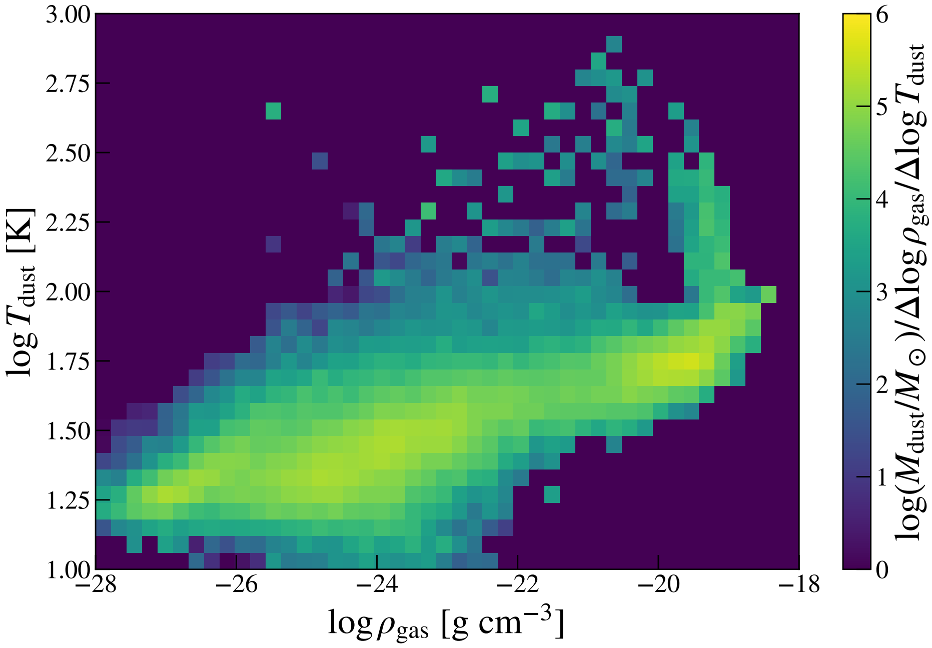

Figure 3.14: Phase diagram of dust in Halo-11 at $z = 6.0$. The cool dust ($T_{\rm dust} < 40\,{\rm K}, \sim 1.2 \times 10^7\,{\rm M}_\odot$) exists in outer low-density regions, while the hot dust ($\gtrsim 40\,{\rm K}, \sim 5 \times 10^6\,{\rm M}_\odot$) is in the central regions and heated by stellar radiation.

more physically, Figure 3.14 presents the phase diagram of dust in Halo-11. Dust temperature increases with increasing gas density (closing the center). At the galactic center, dust temperature is very high ($\sim 100\,$K) due to strong irradiation of stellar UV photons. On the other hand, there is a large amount of cool dust ($\sim 30\,$K) in the outer low-density regions, which is similar with the CMB temperature.

Figure 3.15 shows statistical result of dust temperature using all of galaxies in Halo-11 and Halo-12 boxes at $z = 10,\ 8,\ 7\ \&\ 6$. The dust temperature is measured from the peak wavelength of modified IR spectrum. We find that typical dust temperature for galaxies of $L_{\rm IR} \gtrsim 10^{10}\,{\rm L}_\odot$ is $\sim 60\,$K at all the redshift, which is 2-3 times higher than that of local star-forming galaxies for a specific IR luminosity (Hwang et al., 2010). In addition, dust temperature for high-z galaxies is significantly higher than that of extraordinary dusty starbursts i.e., local ULIRGs (Yang et al., 2007; Younger et al., 2009), and SMGs at $z \sim 1-3$ (Chapman et al., 2005; Kovács et al., 2006). As described below, the compactness of high-z galaxies induces formation of high-density dusty clumps and absorption of UV photons, resulting in the efficient heating of dust grains.

Galaxy size is approximated as ~ 10 per cent of virial radius (see Sec. 3.6), and

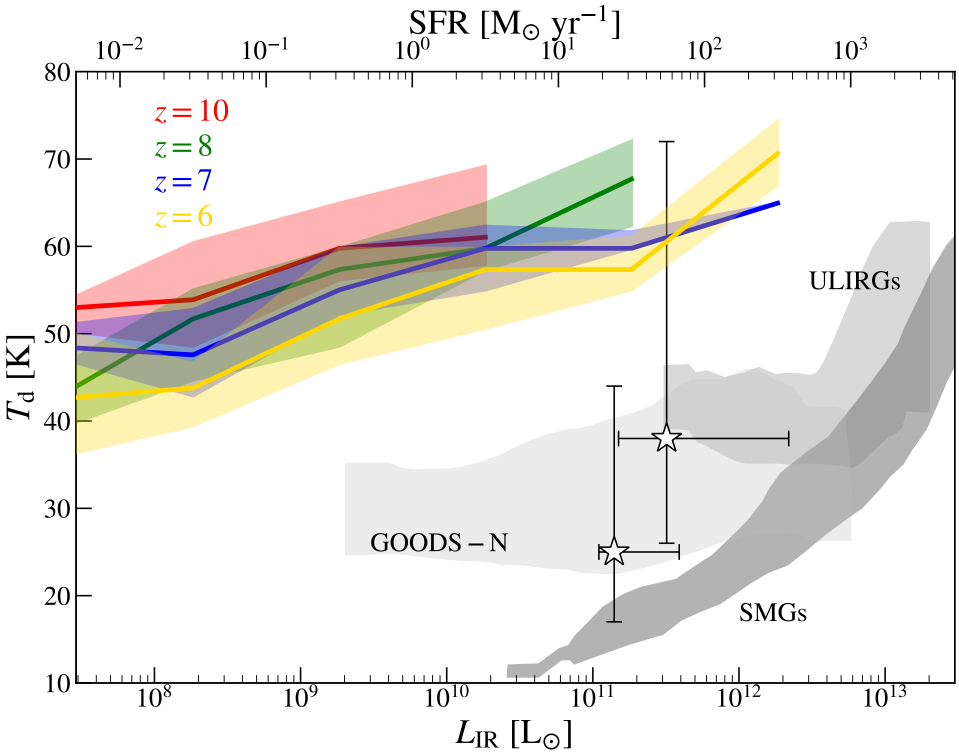

Figure 3.15: Relation between dust temperature and bolometric IR luminosity. The upper horizontal axis indicates SFR derived from equation (3.11). The dust temperature is measured from the peak wavelength of modified SEDs. Different colors mean different redshift: $z = 6$ (yellow), $z = 7$ (blue), $z = 8$ (green), and $z = 10$ (red). The line and shade for each redshift show the median and quantiles of dust temperature for all main and satellite galaxies. Gray shaded regions represent the range of dust temperatures of observed sub-mm galaxies (SMGs) at $z \sim 1-3$ (Chapman et al., 2005; Kovács et al., 2006), ultra-luminous infrared galaxies (ULIRGs) at $z < 1$ (Yang et al., 2007; Younger et al., 2009), and typical star-forming galaxies at $z \sim 0.1-2.8$ (Hwang et al., 2010). The star symbols represent $z \sim 6$ galaxies whose IR spectra were measured in two wavelengths (Harikane et al., 2019). (Modified from Arata et al., 2019)

becomes more compact as redshift increases. Therefore we expect that dust also distribute compactly, resulting in efficient heating of dust by intense stellar UV flux. We estimate the typical distance of dusty clouds from star-forming regions under the assumption of radiative equilibrium as

$$R = \left(\frac{L_{\rm UV}}{16\pi^2 \int Q_\nu B_\nu(T_{\rm d}) d\nu} \right)^{1/2}, \tag{3.15}$$

where Q_ν is the absorption efficiency to the geometrical cross section of dust. Here we use Q_ν estimated in Laor & Draine (1993). In the case of our simulated dust temperature $T_{\rm d} \sim 50 - 70$ K and $L_{\rm UV} = L_{\rm IR} = 10^{11}$ $\rm L_\odot$, the typical distance is $1 - 3\,$kpc, which is similar to the disk sizes of high-z galaxies.

Note that, however, the dust temperature depends on not only the compactness, but also the size distribution of dust grains. Nozawa et al. (2007) suggested that the dust size should be limited in $a \gtrsim 0.1\,\mu$m because small dust grains with $<$ 0.1 μm were destroyed by the reverse shocks in supernova remnants. In addition, Yajima et al. (2014a) studied typical dust size for LBGs at $z \sim 3$ using cosmological simulations and the radiative transfer with various dust sizes $r_{\rm d}$. Comparing the color excess $E(B-V)$ with photometric surveys (~ 0.14, Ouchi et al., 2004), they found that the best-fit model was $r_{\rm d} = 0.05\,\mu$m which supported destruction of small dust grains. Therefore, if we use different dust models from Todini & Ferrara (2001) which includes small grains, the dust temperature could decrease. Harikane et al. (2019) detected the dust continuum of $z \sim 6$ galaxies in two wavelengths with ALMA. Fitting the IR SEDs with the modified blackbody, they derived the dust temperature $T_{\rm d} \sim 30\,$K with the large uncertainties (star symbols in Fig. 3.15), which is close to local galaxies and inconsistent with our predictions. Meanwhile, Bakx et al. (2020) fitted three data points of the dust continuum flux (one detection and two upper-limits) of a $z \sim 8.3$ galaxy, and showed that the galaxy has the high-temperature dusts ($T_{\rm d} \gtrsim 80\,$K). The dust temperature is related to the distributions and properties. To investigate the accurate dust evolution, we need to develop a more realistic model in our simulations (e.g. Aoyama et al., 2017, 2018).

3.5.2 IRX and UV-slope Relationship

The relation between $L_{\rm IR}/L_{\rm UV}$ ratio (IRX) and UV spectral slope $\beta_{\rm UV}$ is often used to predict the dust properties (size distribution and compositions) of high-z galaxies (e.g. Meurer et al., 1999). Recently, Capak et al. (2015) and Bouwens et al. (2016) investigated the IRX–$\beta_{\rm UV}$ relation of galaxies at $z \sim 6$ with ALMA, and found that most of high-z galaxies had lower IRX for a specific $\beta_{\rm UV}$ than that of local star-forming galaxies and the SMC-type galaxies (e.g., Calzetti et al., 2000). However,

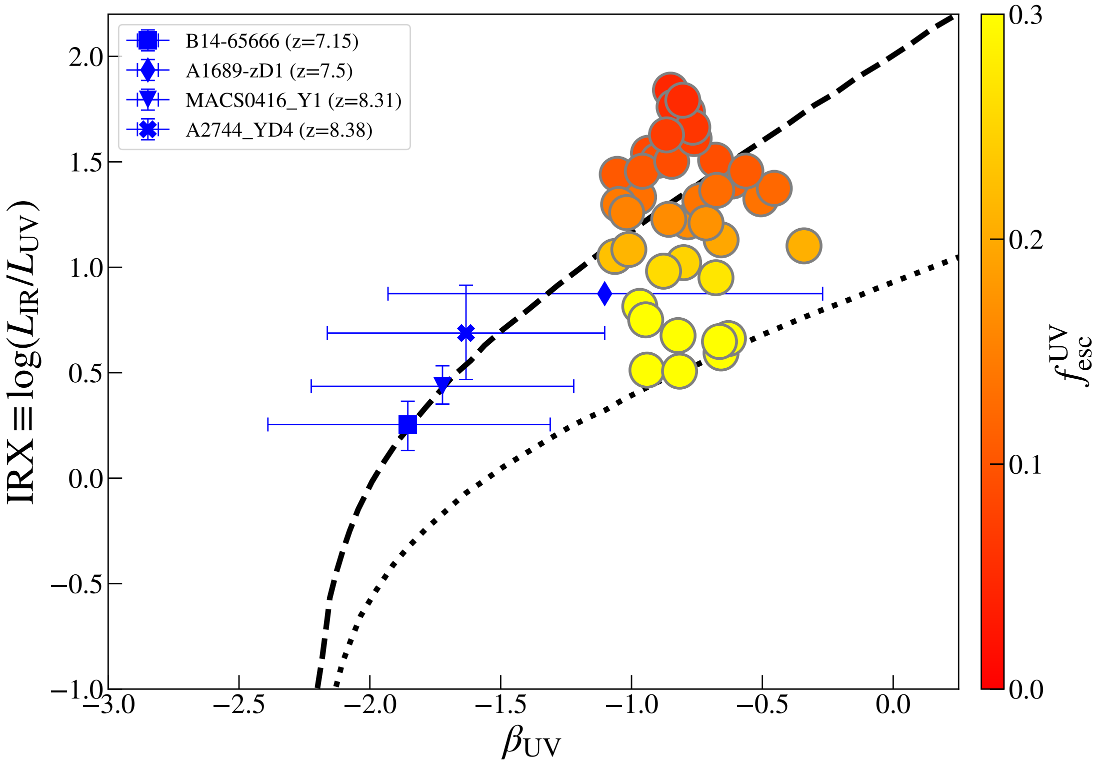

Figure 3.16: Relation between the IRX ($\equiv \log_{10}(L_{\rm IR}/L_{\rm UV})$) and slope of UV spectrum ($\beta_{\rm UV}$). Filled circles represent the IRXs of Halo-11, Halo-12, MHaloes, and LHaloes at $z \sim 6-9$. The color is scaled by escape fraction of UV photons. The dashed and dotted lines represent the Calzetti-law and SMC-law (Meurer et al., 1999; Calzetti et al., 2000), respectively. The blue symbols show the observed high-z LBGs.

analysing the local analogues, Faisst et al. (2017) argued that the typical dust temperature of high-z galaxies was higher than previously assumed ($T_{\rm d} \sim 30\,{\rm K}$), which increases IRX of 0.6 dex with increasing $\Delta T_{\rm d} = 40\,{\rm K}$ (see also, Ouchi et al., 1999). In addition, Ferrara et al. (2017) analytically modeled dust emission from diffuse ISM and molecular clouds, and showed that large molecular fraction significantly decreased IRX, which could explain low-IRX Capak et al. (2015) samples. Narayanan et al. (2018a) conducted cosmological simulations, and found that IR-bright dusty star-forming galaxies had bluer UV spectra (lower $\beta_{\rm UV}$) comparing with the observational reference relation (Casey et al., 2014), which was generated by complex geometry i.e., decoupling young stars from the birth clouds.

Figure 3.16 shows the IRX–$\beta_{\rm UV}$ relation for our simulations. Here we use Halo-11, Halo-12, MHaloes and LHaloes at $z \sim 6-9$. $\beta_{\rm UV}$ is computed from the least square fitting of SEDs in range of $1500 - 2800\,\text{Å}$ by the power-law function of $L_\lambda \propto \lambda^{\beta_{\rm UV}}$, where L_λ is specific emergent luminosity. We find that the IRX increases with decreasing $f_{\rm esc}^{\rm UV}$, and the high and low-$f_{\rm esc}^{\rm UV}$ galaxies are consistent with the SMC-type and Calzetti relations, respectively. Our simulations suggest that intermittent star formation creates the large dispersion of about 1 dex in IRX, and the value of IR-bright phases is consistent with recent high-z observations (blue symbols, Watson et al., 2015; Laporte et al., 2017; Tamura et al., 2019; Hashimoto et al., 2019). However, our galaxies have smaller (redder) $\beta_{\rm UV}$ than observed LBGs. The dust size distribution in our simulations is biased to small grains ($a < 0.1\,\mu$m), resulting in the efficient absorption of shot-wavelength UV photons, and generating the flat UV SED. The difference of $\beta_{\rm UV}$ from the observations might suggest preference to larger size distribution.

As described in Sec. 3.5, our simulations support high dust temperature, which ascribes to the compactness of dusty clouds and strong UV irradiation from nearby massive stars. Recently, Ma et al. (2019) investigated the IRX–$\beta_{\rm UV}$ relation of high-z galaxies in cosmological simulations. They showed that the IRXs of high-z galaxies were consistent with the LMC dust model, and that the typical peak wavelength of dust emission was shorter than the local or intermediate redshift galaxies. This implied that the star-burst efficiently heated the compactly-distributed dust. This trend is consistent with our simulations. However, we note that Casey et al. (2018) argued that the hot dust is not necessarily needed to explain the observed dust characteristics of high-z galaxies; namely, the tension between IRX$-\beta_{\rm UV}$ relation for high-z galaxies and the local relation can also be eased by a cool dust temperature and a mid-IR power-law component. Future multi-band observations of dust continuum flux will be able to validate these theoretical predictions.

3.6 Size Evolution

In this section we investigate evolution of galaxy sizes at UV and [C II] wavelength. In the classical picture, the disk size is determined from the conservation of angular momentum of accreted gas (Mo et al., 1998). However, analysing large samples in the Illustris simulations, Genel et al. (2015) showed that the galactic angular momentum was redistributed due to stellar feedback (see also, Scannapieco et al., 2008; Zavala et al., 2008). They found that the feedback processes change the galactic morphologies, and succeeded to reproduce the observational relation between the specific angular momentum and stellar mass at $z = 0$ (Fall & Romanowsky, 2013). Here we study how the sizes of clumpy high-z galaxies change with time and affect the detectability of galaxies. Our simulated galaxies have disks at $z \lesssim 10$, and the sizes are affected by SN feedback as described in Yajima et al. (2017b).

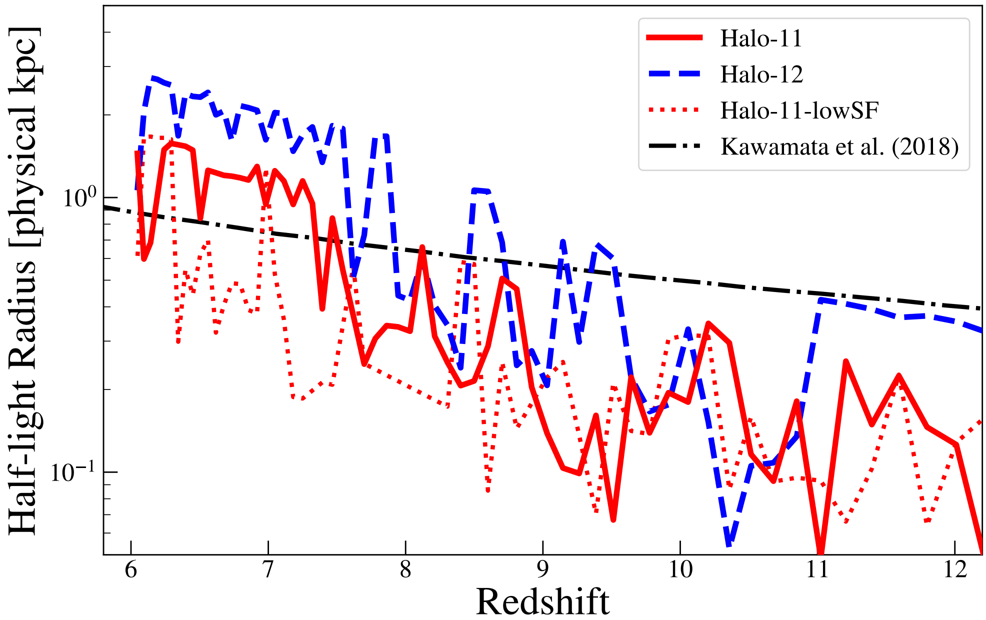

Figure 3.17: Redshift evolution of the UV half-light radius as a function of redshift, which is upper limited at $0.1r_{\rm vir}$ avoiding artificial extending due to mergers (see text). The black line represent observational fit (Kawamata et al., 2018). (Modified from Arata et al., 2019)

3.6.1 UV Half-light Radius

Figure 3.17 shows the UV half-light radii ($r_{\rm e}$) of Halo-11 and Halo-12 as a function of redshift. To determine $r_{\rm e}$, we draw a circle centering on the UV brightest pixel, and increase the radius until the enclosed brightness becomes less than half of the total brightness. However, if the galaxies are merging, this method could predict too large $r_{\rm e}$ artificially. Therefore we set the upper limit of $r_{\rm e}$ to 10 per cent of virial radius. We observe that $r_{\rm e}$ fluctuates around $0.02 - 0.1$ times the virial radius. In star-burst phases, stars and gas distribute at the galactic center compactly due to the gravitational potential, resulting in smaller $r_{\rm e}$. Meanwhile, $r_{\rm e}$ reaches the upper limit ($0.1r_{\rm vir}$) in outflowing phases or when the main galaxies interact with satellite galaxies. In addition, $r_{\rm e}$ gradually increases with decreasing redshift following to the virial radius ($\propto M_{\rm h}^{1/3}(1+z)^{-1}$). Finally, the galactic size becomes ~ 1 physical kpc at $z \sim 6$, and more massive galaxy has a larger size.

Understanding the size distribution of high-z galaxies is crucially important for the correction of detection incompleteness in deriving a luminosity function (LF). If two galaxies have same luminosity but different sizes, surface brightness per pixel in the extended galaxy is lower than that of compact one. Thus the extended galaxies are more unlikely to be detected for a given magnitude limit, or some fraction of their flux is lost due to the limited sensitivity. This affects the estimation of faint-end slope of UV LFs (e.g., Grazian et al., 2011).

Figure 3.18 presents the size–luminosity (RL) relation of Halo-11, Halo-12 and all satellite galaxies in their zoom-in regions at $z \sim 6-10$. Observationally, Kawamata et al. (2018) conducted the simultaneous maximum-likelihood estimation of UV LF and RL relation for $z > 6$ galaxies in HFF, and found that the slope β for the RL relation $r_{\rm e} \propto L^{\beta}$ is ~ 0.4 (green line). Our simulation shows that more bright galaxies have larger $r_{\rm e}$ and the slope of RL relation for $M_{\rm UV} < -15$ is ~ 0.4, which remarkably matches observations.

On the other hand, however, faint galaxies ($M_{\rm UV} \gtrsim -15$) have a larger dispersion and their sizes do not match the observational fit. The minimum softening length is ~ 30 physical kpc at $z = 6$, thus the extending is not artificial. This can be explained from the intermittent star formation histories of low-mass galaxies. The SN feedback induces the angular momentum redistribution of gas disc and make newly formed stellar distribution extended (see also, El-Badry et al., 2016). Or if star clusters are virialized with the local gravitational potential, they can spread out with the gas outflow due to feedback (Ricotti et al., 2016). In addition, the quenching time of star formation becomes longer as the galaxy mass decreases, which induces larger size decided from extended residual stars. These effects might change the slope of RL relation at the faint end ($M_{\rm UV} \gtrsim -13$). Thus, we suggest that previous observations could lost some fraction of low-mass galaxies due to the extended stellar distribution and faint surface brightness. This could change the faint-end slope of UV LF. Note that Ma et al. (2018) also showed the large dispersion of galaxy sizes at the faint-end. They argued that if the sensitivity of surface brightness was lower than $\mu \sim 25.5\,{\rm mag\ arcsec^{-2}}$, the size measurement was biased by the central bright star-forming clumps, resulting in the underestimation of sizes. To avoid picking up multiple clumps in low-mass galaxies which could boost up the value of $r_{\rm e}$, we did not include the galaxies that are larger than 0.1 times virial radii.

Note that, however, the galactic size or 'compactness' can be affected by star formation model as described in Y17. In addition, Wyithe & Loeb (2011) pointed out that the RL relation is also affected by SN feedback model. We also present the size evolution of Halo-11-lowSF in Fig. 3.17 to show the difference from that of fiducial case. The low-A star formation induces inefficient SN feedback and allows the formation of very dense and compact gas clumps at the galactic center, which efficiently traps UV photons. Thus $r_{\rm e}$ remains lower value for long time. We discuss

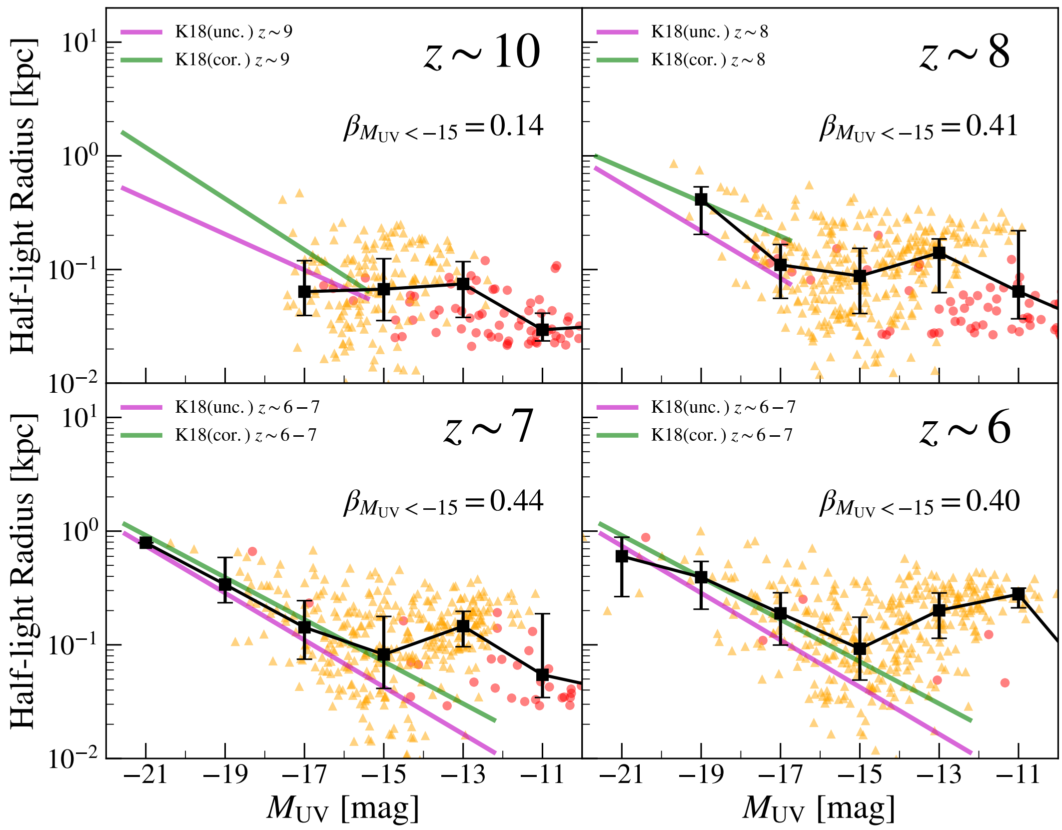

Figure 3.18: Relation between galaxy size and absolute UV magnitude for all main and satellite galaxies in Halo-11 (red circles) and Halo-12 (orange triangles) zoom regions at $z \sim 10$, 8, 7 & 6. Black squares and errorbars show medians and quantiles for bins of $\Delta M_{\rm UV} = 2.0$. In each panel, we also show slope of the size-luminosity relation ($r_{\rm e} \propto L^{\beta}$) using galaxies with $M_{\rm UV} < -15$. Green and magenta lines represent observational fit from Kawamata et al. (2018) with/without correction of detection incompleteness, respectively. (Modified from Arata et al., 2019)

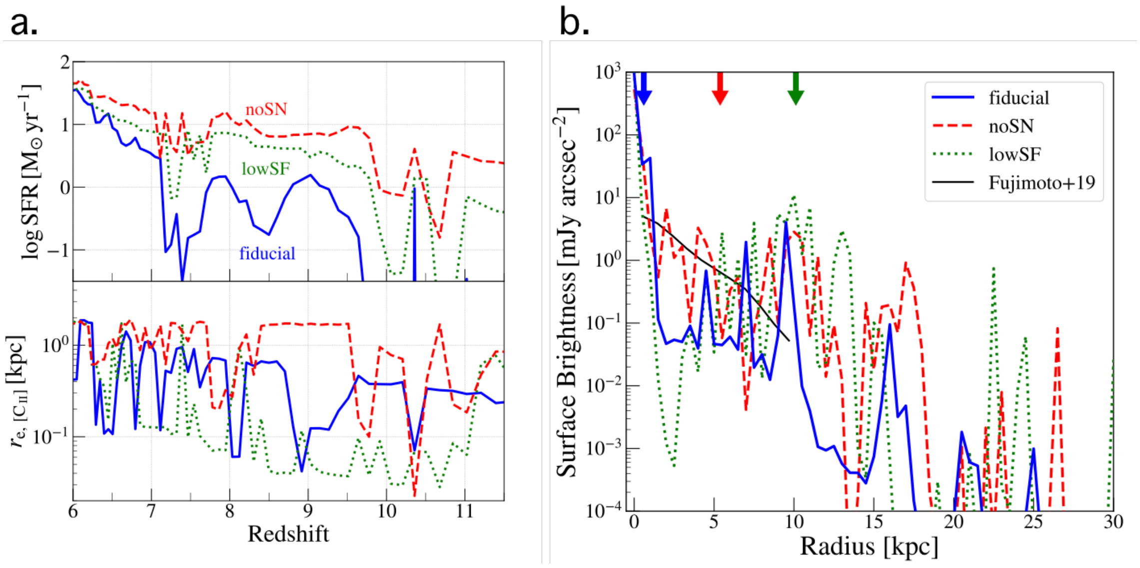

Figure 3.19: **(a)** Redshift evolution of SFRs (top panel) and the half-light radii in [C II] 158 μm (bottom panel) of Halo-11 (blue solid), Halo-11-lowSF (green dotted) and Halo-11-noSN (red dashed). We set upper limit of $r_{\mathrm{e,[C\,II]}}$ to avoid artificial extension when the main galaxy mergers with the companions. **(b)** Radial profiles of the [C II] surface brightness of Halo-12, Halo-12-lowSF and Halo-12-noSN at $z = 6.45$. Upper arrows represent positions of the half-light radii. Black line represent observational result of Fujimoto et al. (2019). (Modified from Arata et al., 2020)

more details of model dependence in Section 3.7.

3.6.2 [C II] Radial Profiles

Galaxy size has been studied in the UV wavelength which represents stellar distribution. However, recent ALMA observations have allowed us to study the gas kinematics and distribution in distant galaxies via [C II] emission. Fujimoto et al. (2019) stacked the ALMA data of 18 galaxies at $z \sim 5 - 7$, and detected the [C II] emission extended over ~ 10 kpc. The effective radius was larger than the disk scale measured from the rest-UV and FIR continuum emissions. This implies that there was abundant gas supply to form stars in the first galaxies.

Figure 3.19a shows evolution of half-light radius of Halo-11 measured by [C I I] wavelength (blue solid). $r_{\mathrm{e,[C\,II]}}$ becomes small in star-burst phase, because the [C II] emitting clouds concentrate at the galaxy center. It extends to $0.1 r_{\mathrm{vir}}$ when gas outflows due to SN feedback or the galaxy mergers. At $z < 8$, the galaxy forms multiple high-density clumps in the disk, resulting in large fluctuation of $r_{\mathrm{e,[C\,II]}}$. We also compare [C II] sizes in the cases of low-SF and no-SN. SN feedback is inefficient due to rapid cooling in low-SF case, which induces smaller size than fiducial case. However, this also form [C II] clumps outer regions which boosts up $r_{\mathrm{e,[C\,II]}}$ temporally (Figure 3.19b). The [C II] clumps are not destroyed in no-SN case, resulting in smoothed distribution and larger size than fiducial case over all redshift.

Figure 3.20 shows stacked [C II] surface brightness profiles at $z \sim 6$. We find that more massive system is more extended. Also the simulated profiles are very peaky at inner radii ($r < 5$ physical kpc) and smoothly extend outer part. To mimic observations, we convolve them with the PSF of ALMA by following two ways. The PSF has the central Gaussian profile (black dashed) and takes negative values at outer part ($r > 7$ kpc). In the first case, we set the negative values to zero and normalize it, and take convolution with the simulations (dotted lines). Second, we convolve the PSF including the negatives with the simulations and scale them to conserve the total surface brightness (dot-dashed lines). In both cases, the slopes of inner profiles ($r < 7$ kpc) are completely determined by the PSF due to the original very peaky structures. As shown in Table. 2.1, our samples of LHaloes (purple) have similar UV magnitudes to those of stacked samples in Fujimoto et al. (2019) ($-23 < M_{\mathrm{UV}} < -21$). We find that the simulated surface brightness is significantly higher than the observational result at $r < 7$ kpc.

To reproduce the observation, our simulation are required to decrease the central surface brightness about two order magnitudes. As Neri et al. (2014) suggested, high-z galaxies might be optically thick to [C II] emission, which can reduce the central brightness. Also our simulations do not resolve formation of molecular clouds, which is possible to suppress [C II] emission (Narayanan & Krumholz, 2017).

We also need to enhance brightness of outer part, because the total [C II] luminosity in our simulations has a good agreement with observations. This might be improved by using more realistic feedback models. In star-forming galaxies, gas clouds are ejected from the disk by stellar radiation pressure, and further accelerated by SN feedback (Murray et al., 2011; Muratov et al., 2015). The outflowing gas clouds are cool ($\sim 10^4$ K), and stacking over various viewing angles will produce more extended profile. Anyway, galaxy sizes are related to intermittent star formation. Using abundant samples of the ALPINE survey, Ginolfi et al. (2019) showed that higher-SFR galaxies have more extended [C II] profiles.

3.7 Impact of Sub-grid Models

We have studied the radiative properties of different haloes simulated with the *fiducial* star formation and feedback models. Here we investigate how the radiative

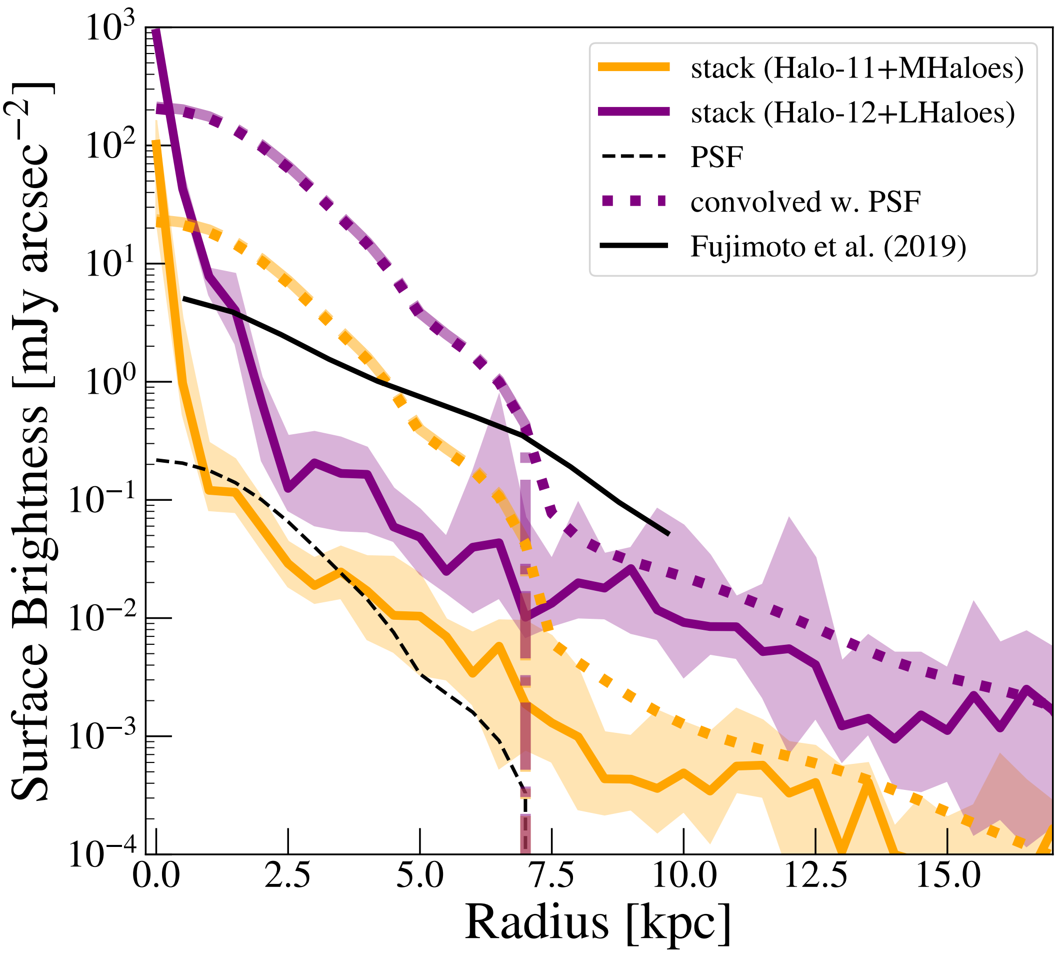

Figure 3.20: Average [C II] radial profiles of $M_{\rm h} \sim 10^{11}\,{\rm M}_\odot$ haloes (orange) and $M_{\rm h} \sim 10^{12}\,{\rm M}_\odot$ haloes (purple) at $z \sim 6$. The solid lines represent medians of stacking over (Halo-11+MHaloes) $\times$ 3-viewing angles and (Halo-12+LHaloes) $\times$ 3-viewing angles, respectively, and the shades are for the quartiles. The dotted lines show the profiles convolved with the point spread function (PSF) of ALMA (see text).

properties change if we decrease the star formation efficiency (low-SF case) or turn off the SN feedback (no-SN case). Recent observations suggested that the amplitude factor of Kennicutt–Schmidt law for merging galaxies or high-redshift galaxies was much higher than local galaxies (Genzel et al., 2010; Tacconi et al., 2013). Therefore we use a high amplitude factor of $A = 1.5 \times 10^{-3}\ \mathrm{M_\odot\,yr^{-1}\,kpc^{-1}}$ which is higher than that of the local galaxies by a factor 10. The low-SF runs use the amplitude factor same as the local galaxies, i.e., $A = 1.5 \times 10^{-4}\ \mathrm{M_\odot\,yr^{-1}\,kpc^{-1}}$. We have already discussed the impact of sub-grid models onto some radiative properties in Fig. 3.8 (the number density of SMGs), 3.12 (chemical enrichment) & 3.19 ([C II] surface brightness profile).

Figure 3.21 shows different evolution of UV/IR wavelength in Halo-11, Halo-11-lowSF and Halo-11-noSN runs. Lower amplitude factor A induces formation of high-density gas clouds which efficiently absorb UV photons, resulting in lower escape fraction in low-SF case. The dense gas rapidly cools the released energy by SNe, thus dust distribution does not change and the escape fraction keeps low value ($f^{\rm UV}_{\rm esc,lowSF} \sim 0.1$) at $z < 10$. The galaxy is continuously bright in sub-mm wavelength due to dust emission, which increases the observability by ALMA and the number density of SMGs (Fig. 3.8). Although the SFR is higher than that of fiducial case, apparent UV magnitude becomes very similar due to efficient dust absorption. On the other hand, gas density does not become quite high in no-SN case because of the high star formation efficiency. The SN energy is not injected into surrounding gas, and dust continuously accumulate in the galaxy center. By these effects, escape fraction takes moderate values ($f^{\rm UV}_{\rm esc,noSN} \sim 0.3$). The no-SN run has the highest SFR, and is brighter in UV wavelength of $\Delta m_{\rm UV} \sim 2\,$mag than other runs. The UV light at $z \sim 12$ could be observed by F200W filter of JWST.

Figure 3.22 shows the relation between SFR and metal-line luminosities in each case. In low-SF case, dense gas induces rapid hydrogen recombination, and massive stars do not form huge ionized regions. The galaxy is dominated by neutral regions, thus has higher [C II] and lower [O III] luminosities than the fiducial case. The $L_{\rm [O\,III]}$–SFR relation is close to the local star-burst galaxies , but $L_{\rm [C\,II]}$–SFR relation is significantly higher than the local relations. On the other hand, $L_{\rm [O\,III]}$–SFR relation in no-SN case is much close to that of fiducial case, because gas density in the two cases is similar and stars form H II regions with similar sizes. However, the chemical evolution is much earlier in no-SN run (Fig. 3.12), resulting in higher $L_{\rm [C\,II]}$ than that of fiducial run. Finally, we present the $L_{\rm [O\,III]}/L_{\rm [C\,II]}$ ratio of the three cases in the bottom panel. We find that only our fiducial run can reproduce observational negative correlation. Our simulations suggest that the future survey of high-z [O III] and [C II] emitters will reveal the validity of the theoretical models of star formation

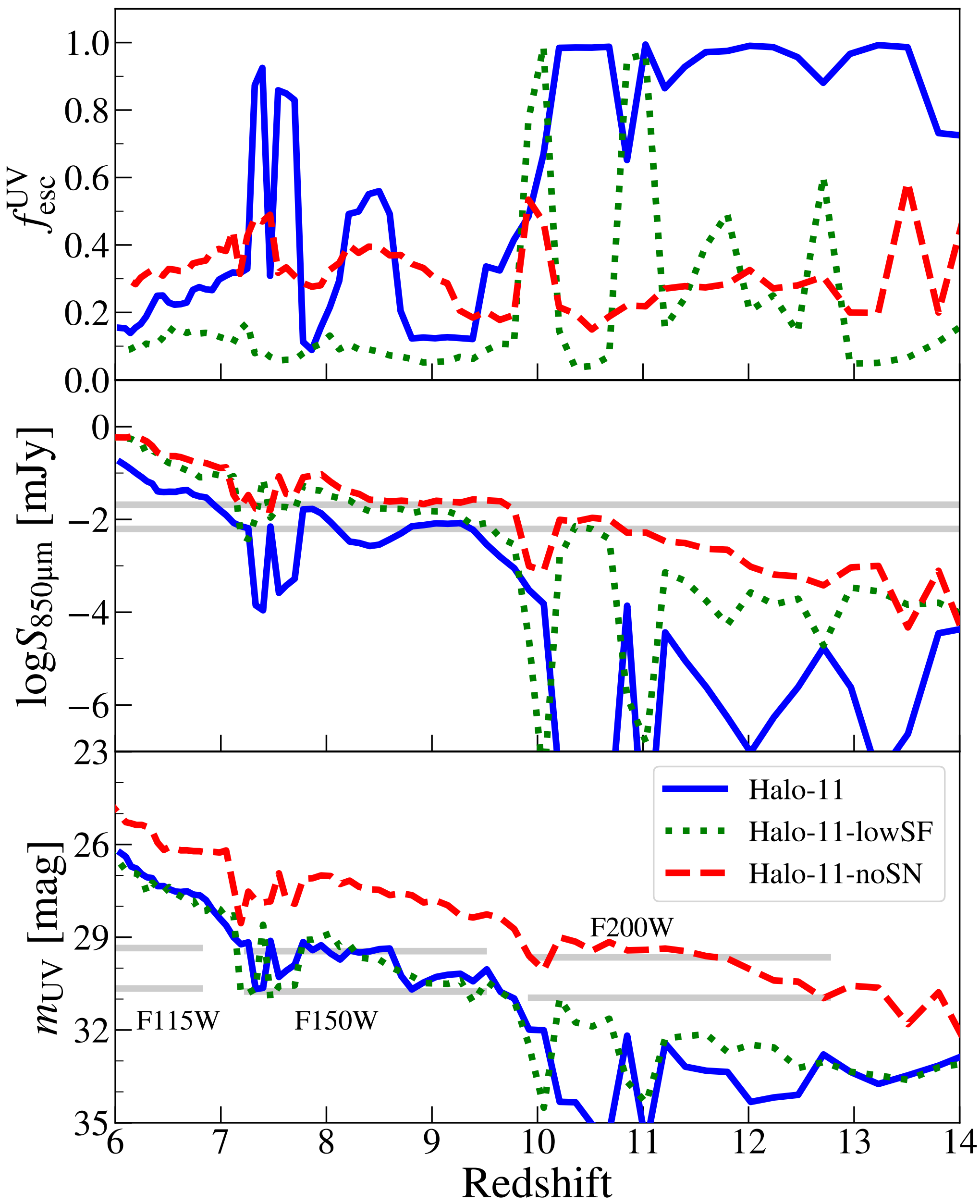

Figure 3.21: Redshift evolution of escape fraction of UV photons (top), sub-mm flux (middle) and apparent UV magnitude (bottom) in the fiducial (blue solid), low-SF (green dotted) and no-SN cases (red dashed). The meanings of grey lines are same as Fig. 3.4.

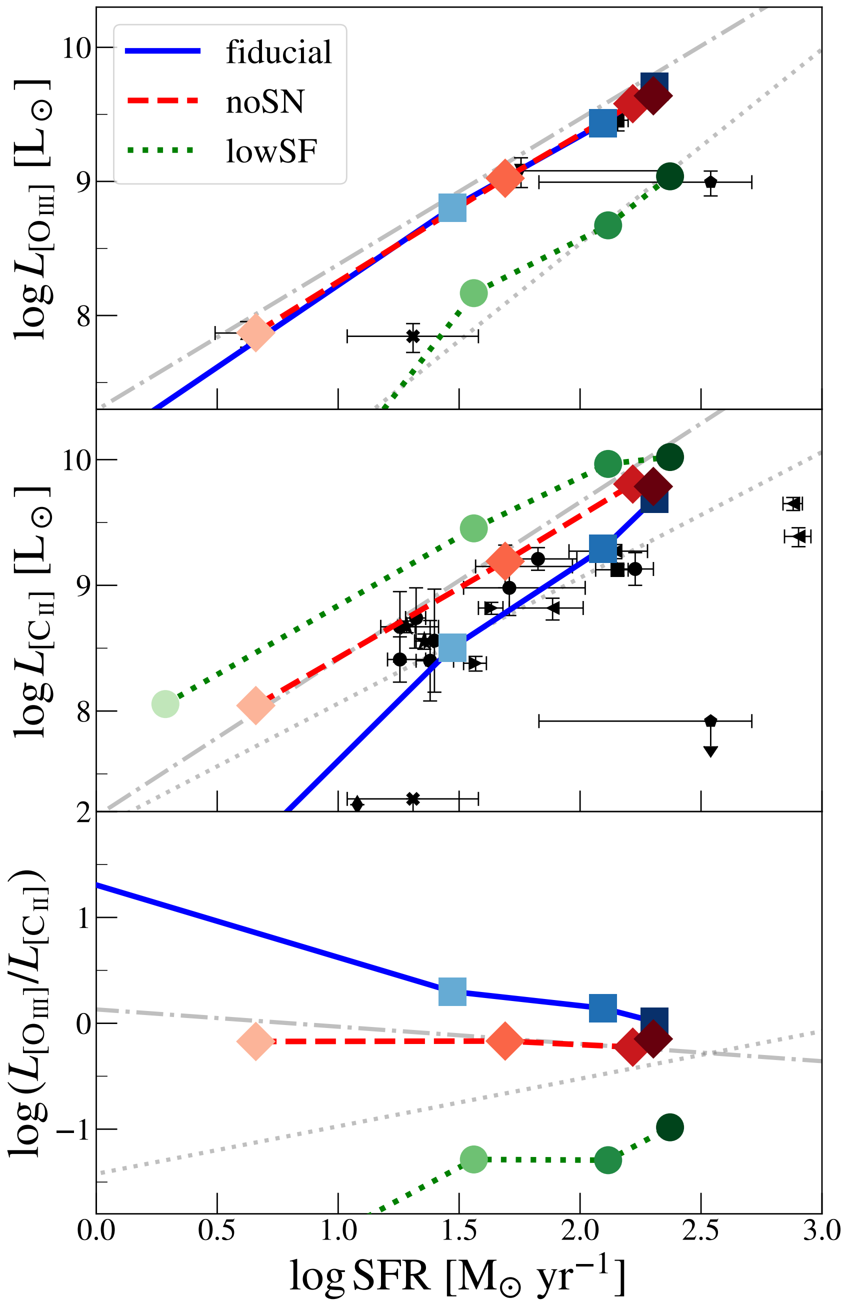

Figure 3.22: Relation between SFR and [O III] luminosity (top), [C II] luminosity (middle) and $L_{[\mathrm{O\,III}]}/L_{[\mathrm{C\,II}]}$ ratio (bottom) of Halo-12, Halo-12-lowSF and Halo-12-noSN at $z = 9,\ 8,\ 7\ \&\ 6$ (lighter to darker). The meaning of symbols is same as Fig. 3.10 & 3.11. Dotted and dot-dashed lines represent the local relations for star-burst galaxies and metal-poor galaxies, respectively (De Looze et al., 2014).

and feedback processes.

Chapter 4

Summary and Future Prospects

To investigate the relation between galaxy evolution and radiative properties in the reionization epoch, we combined cosmological hydrodynamic simulations and multi-wavelength radiative transfer calculations at $z = 6 - 15$. We used the zoom-in technique and resolved the detailed gas structure in $M_{\rm h}|_{z=6} \sim 10^{11} - 10^{12}\,{\rm M_\odot}$ haloes (Halo-11, Halo-12, MHalo-0, 1, 2, 3 and LHalo-0, 1, 2, 3, 4, 5; Table 2.1). Our major findings are as follows.

1. Escape fraction of UV continuum photons fluctuates between $20-80\,\%$ with intermittent star formation due to supernova feedback and gas accretion (Fig. 3.4). In star-burst phases, dust efficiently absorbs UV photons, and the re-emission makes the SED bright in the infrared wavelength (Fig. 3.5b). We find that the simulated IR luminosity has a good agreement with recent observational results (Fig. 3.9). On the other hand, galaxies become UV-bright in outflowing phases. The time-scale of SED transition is $\sim 100\,$Myr.

2. [O III] $88\,\mu$m is emitted only in star-burst phases, because O^{2+} ions exist in H II regions formed by massive stars (Fig. 3.6a). On the other hand, [C II] $158\,\mu$m is continuously emitted from neutral gas even in outflowing phases. We find that deep [C II] observation with a sensitivity of $\sim 10^{-2}$ mJy arcsec^{-2} can trace extended neutral gas structure of ~ 20 physical kpc (Fig. 3.1). Also combination of [O III] and [C II] observations will reveal detailed ionization structure of the early galaxies (Fig.3.6b).

3. Using the SEDs of all satellite galaxies in the zoom-in boxes of Halo-11 and Halo-12, we study the observability of dust emission from the first galaxies in a sub-millimeter wavelength ($850\,\mu$m). We find that the observability of galaxies with $M_{\rm h} \sim 10^{11}$ ($10^{10.5}$) ${\rm M_\odot}$ exceeds $50\,\%$ if the detection threshold flux is 0.1 (0.01) mJy which corresponds to 20 min (40 hours) time-integration with fully-operated ALMA (Fig. 3.7).

4. The slope of the relation between $\log(\mathrm{SFR}/\mathrm{M}_\odot\ \mathrm{yr}^{-1})$ and $\log(L_{[\mathrm{O\,III}]}/\mathrm{L}_\odot)$ is 1.04 at $z = 6-9$, and 1.43 for $\log(L_{[\mathrm{C\,II}]}/\mathrm{L}_\odot)$ (Fig. 3.10). These results are consistent with recent high-z observations, and close to the relation of the local metal-poor galaxies. Measurement of the sizes of [O III] emitting regions will constrain the theoretical models of radiative feedback.

5. The luminosity ratio $L_{[\mathrm{O\,III}]}/L_{[\mathrm{C\,II}]}$ decreases from ~ 10 to ~ 1 with increasing total gas metallicity from $\sim 0.1\,\mathrm{Z}_\odot$ to $\sim \mathrm{Z}_\odot$ (Fig. 3.11). The abundance ratio O/C is initially dominated by the oxygen-enrichment of Type-II SNe, but decreases later due to carbon-rich winds from AGB stars. We find that the origin of observed negative correlation can be explained by this process.

6. The simulated galaxies have hot dust (~ 90 K) at the centre, and also cool dust (~ 30 K) at the outer disk. Analyzing the peak wavelength of IR SEDs, we find that typical dust temperature in high-z galaxies is $\sim 60\,\mathrm{K}$ which is a few times higher than those of nearby star-forming galaxies, local ULIRGs and SMGs at $z \sim 2-3$ (Fig. 3.15). The compactness of the first galaxies induces dust heating due to intense stellar radiation, resulting in the high temperature.

7. The half-light radii in UV and [C II] wavelengths become small ($\sim 0.01 r_{\mathrm{vir}}$) during the star-burst phases, because stellar and gas distribution become concentrated at the centre due to gravitational potential (Fig. 3.17, 3.19). The size–luminosity relation for bright galaxies ($M_{\mathrm{UV}} \lesssim -15$) is remarkably consistent with the observational fits (Fig. 3.18). However, our relation turns over at the fainter side ($-15 \lesssim M_{\mathrm{UV}} \lesssim -11$), which is a result of longer time-scale of star formation quenching. We suggest that the present observations miss the fainter population, which could make the observed faint-end slope of UV luminosity function flatter. Furthermore, we compare the average 1D surface brightness profile of [C II] emission with observations. Our simulations predict very peaky structure at the center, while the stacked result of observations show a more extended profile (Fig. 3.20). More realistic feedback models might carry more cool mass ($\sim 10^4\,\mathrm{K}$) to farther out and reproduce the observations.

In short, we find that *the first galaxies rapidly change their radiative properties due to intermittent star formation and SN feedback, which is consistent with observations.* We also present the impact of sub-grid models onto radiative properties using low-SF and no-SN runs (Table.2.1). The lower star formation efficiency induces higher gas density, resulting in lower escape fraction of UV photons and higher [C I

I] luminosity. Therefore the predicted number density of observable sub-mm sources (Fig. 3.8) and $L_{[\mathrm{O\,III}]}/L_{[\mathrm{C\,II}]}$ ratio (Fig. 3.22) changes significantly with the models. Future deep survey of high-z galaxies by ALMA will constrain theoretical models by comparing with our simulations. As discussed in Sec. 3.5, our assumed dust size distribution is likely to be smaller than the reality, because the UV slopes of simulated galaxies are shallower (redder) than observations at a specific IRX (Fig. 3.16). For more accurate treatment of dust, we need to track the evolution of dust grains locally in cosmological simulations. Also more realistic modeling of dust in radiative transfer calculations could be important to reproduce the $(L_{[\mathrm{C\,II}]}/L_{\mathrm{IR}})$–$L_{\mathrm{IR}}$ relation (Fig. 3.13). In addition, our simulations could not reproduce the properties of some observed galaxies e.g., very [C II]-faint galaxies and extremely star-bursting SMGs ($\gtrsim 1000\,\mathrm{M_\odot\ yr^{-1}}$) (Fig. 3.10). In the future, we will investigate properties of these galaxies using large samples in large-scale simulations. Understanding formation mechanism and observational properties of the first galaxies is closely linked to the cosmological structure formation history based on the Λ cold dark matter (ΛCDM) theory. Combination of state-of-the-art simulations and observations by the next generation telescopes e.g., JWST and TMT will solve the fundamental questions in astronomy.

Appendix A

Details of Simulation Models

A.1 Radiative Transfer

The Monte Carlo radiative transfer tracks propagation of photon packets considering with dust scattering, absorption and re-emission under the assumption of radiative equilibrium. Our radiative transfer calculation code, $\mathrm{A}\textsc{rt}^2$ (Li et al., 2008; Yajima et al., 2012a), employs this method based on Bjorkman & Wood (2001). Also the $\mathrm{A}\textsc{rt}^2$ uses the sub-grid model of multi-phase ISM by Springel & Hernquist (2003) to obtain optical depth in cold and hot phases. Here we briefly explain their treatment.

The energy carried by a photon packet is E_γ, and the number of packets which are absorbed by the i-th cell is N_i, then the total absorbed energy is

$$E_i^{\mathrm{abs}} = N_i E_\gamma. \tag{A.1}$$

We assume that the emission spectrum of the cell with dust temperature T_i follows the Planck function $B_\nu(T)$, and the total emission energy is described as

$$\begin{aligned} E_i^{\mathrm{em}} &= 4\pi \Delta t\, V_i \int \rho_i \kappa_\nu B_\nu(T_i) d\nu \\ &= 4\pi \Delta t\, m_i \kappa_{\mathrm{P}}(T_i)\, B(T_i), \end{aligned} \tag{A.2}$$

where V_i is the volume of i-th cell, ρ_i is the dust mass density, and κ_ν is the dust opacity as a function of frequency. In the lower equation, m_i is the dust mass within the cell, and $\kappa_{\mathrm{P}} = \int \kappa_\nu B_\nu d\nu / B$ is the Planck mean opacity, where $B = \int B_\nu d\nu = \sigma T^4/\pi$ and σ the Stefan–Boltzmann constant. From the condition of radiative equilibrium ($E_i^{\mathrm{abs}} = E_i^{\mathrm{em}}$), we obtain the equilibrium dust temperature,

$$\begin{aligned} \sigma T_i^4 &= \frac{N_i E_\gamma}{4\Delta t\, m_i \kappa_{\mathrm{P}}(T_i)} \\ &= \frac{L N_i}{4 N_\gamma m_i \kappa_{\mathrm{P}}(T_i)}. \end{aligned} \tag{A.3}$$

At the second equality, we use the total source luminosity, $L = E_{\rm tot}/\Delta t = N_\gamma E_\gamma/\Delta t$, where $E_{\rm tot}$ and N_γ are the total energy and number of photon packets in the simulation, respectively. Then the re-emission emissivity Δj_ν is determined by the temperature increment ΔT_i,

$$\Delta j_\nu = \kappa_\nu \rho_i \Delta T_i \frac{dB_\nu(T_i)}{dT_i}. \tag{A.4}$$

Note that the re-emitted packets continue to be scattered, absorbed and re-emitted until they finally escape from the system.

The location of scattering or absorbing a photon packet is determined by the probability given by the albedo $a = n_s\sigma_s/(n_s\sigma_s + n_a\sigma_a)$, where n and σ are the number density and cross-section for either scattering or absorption, respectively. If the photon is scattered, its direction and polarization state are altered using the Henyey–Greenstein phase function. If instead the packet is absorbed, it will be re-emitted with new frequency sampled from the updated spectrum, as described above. It is well-known that dust mainly exists in the cold phase because dust would be destroyed by collisions with the gas in hot phase (e.g. Draine et al., 2007). To estimate the optical depth, we combine the multi-phase ISM model and empirical relations of the giant molecular clouds (GMCs).

Assuming pressure equilibrium between cold and hot phases, we obtain their densities ρ_c, ρ_h for each cell (see the next sub-section, Springel & Hernquist, 2003). We also assume that the cold clouds follow the two observational relations,

$$\frac{dn}{dM} = AM^{-\alpha}, \tag{A.5}$$

$$M = BR^\beta, \tag{A.6}$$

where dn/dM is the distribution function of clouds with mass M, and cloud radius R. We set $\alpha = 1.8$ and $\beta = 2.0$ as observations suggested (e.g., Blitz & Rosolowsky, 2006; Rosolowsky, 2005, 2007). From these equations, we obtain the cloud size distribution,

$$\frac{dn}{dR} = \beta AB^{1-\alpha}R^{-(\alpha\beta+1-\beta)} = CR^{-\gamma}, \tag{A.7}$$

where $C = \beta AB^{1-\alpha}$ and $\gamma = \alpha\beta + 1 - \beta$.

Integrating the mass of cold clouds over the range of minimum and maximum values (M_0 and M_1), the normalization constant of the mass spectrum A is determined as

$$\int_{M_0}^{M_1} M\frac{dn}{dM}dM = x_c\rho_c, \tag{A.8}$$

and

$$A = x_c\rho_c\frac{2-\alpha}{M_1^{2-\alpha} - M_0^{2-\alpha}}, \tag{A.9}$$

where x_c is the volume filling factor of the cold phase. Furthermore, the normalization constant of the mass–size relation B is determined from

$$x_c = \int_{M_0}^{M_1} \frac{4\pi}{3} R^3 \frac{dn}{dM} dM, \tag{A.10}$$

and

$$B = \left[\frac{4\pi A}{3\eta x_c} (M_1^\eta - M_0^\eta) \right]^{\beta/3}, \tag{A.11}$$

where $\eta = 1 + 3/\beta - \alpha$. In this paper, we set $M_0 = 10^3\,\mathrm{M}_\odot$ and $M_1 = 10^7\,\mathrm{M}_\odot$, which is consistent with the mass of observed proto-cluster clouds in star-forming galaxies.

The average number of cold clouds with the radius R, which a photon will intersect, is given by

$$\frac{dN}{dR} = \pi R^2 L \frac{dn}{dR} = \pi L C R^{2-\gamma}, \tag{A.12}$$

where L is the traveling distance of the photon. Integrating over the cloud radius $[R_0 = (M_0/B)^{1/\beta},\, R_1 = (M_1/B)^{1/\beta}]$, we obtain

$$N = \pi L C \frac{R_1^{3-\gamma} - R_0^{3-\gamma}}{3-\gamma}. \tag{A.13}$$

Thus, the average distance of photon travels before hits a cold cloud (the mean free path) is given by

$$L_m = \frac{3-\gamma}{\pi C (R_1^{3-\gamma} - R_0^{3-\gamma})}. \tag{A.14}$$

In radiative transfer calculations, we assume that both of cold and hot phases contribute dust absorption with specific dust-to-gas mass ratio (see Sec. 2.2). We first determine the traveling distance in hot phase, $L_h = -L_m \ln \xi$, where ξ is a random number uniformly distributed between 0 and 1. The radius of cold cloud encountering the photon is also given randomly assuming distribution function eq. (A.12),

$$R = \left[R_0^{3-\gamma} + (R_1^{3-\gamma} - R_0^{3-\gamma})\xi \right]^{1/(3-\gamma)}. \tag{A.15}$$

The traveling distance in this cold cloud is given by $L_c = 2R\sqrt{\xi}$ assuming that clouds distribute uniformly. Here we obtain the column density of hot and cold phases,

$$\begin{aligned} N_h &= \rho_h L_h, \\ N_c &= \frac{3M}{4\pi R^3} L_c = \frac{3 B R^{\beta-3} L_c}{4\pi}. \end{aligned} \tag{A.16}$$

Given a opacity curve, we can calculate the optical depths τ_h and τ_c from these equations. We accumulate the optical depth $\tau_{\rm tot}$ along the photon path, and compare with a random number $\tau_i = -\ln \xi$ at the each boundary between hot and cold phases. If $\tau_i \le \tau_{\rm tot}$, the photon is either scattered or absorbed with the probability given by the albedo, and set $\tau_{\rm tot}$ to zero.

A.2 Multi-phase ISM

The formation of cold clouds is induced via thermal instability. When the cooling rate increases with decreasing temperature, the condition of thermal instability is satisfied (Field, 1965). Assuming ionization equilibrium under the UV background (Haardt & Madau, 1996, 2012), the cooling function at a specific temperature is computed. For the primordial gas (only H and He), the cooling rate satisfies the condition at $T \sim 10^5 - 10^6\,\mathrm{K}$ (McKee & Ostriker, 1977; Fall & Rees, 1985; Katz et al., 1996). The turnover of cooling function shifts to $\sim 10^7\,\mathrm{K}$ for metal-enriched gas (Wiersma et al., 2009a; Richings et al., 2014a,b). In thermally unstable ISM, density (temperature) perturbations rapidly grow under the pressure equilibrium with ambient hot medium, and become cool clouds with $T \sim 10^4\,\mathrm{K}$. The clouds also satisfy the condition of thermal instability due to [C II] and O I cooling rates, and further cool down to $\sim 100\,\mathrm{K}$ and become confined molecular clouds which will form stars (Arata et al., 2018). Massive stars release the energy as SN feedback, which evaporates cold clouds and returns the mass to the hot phase. The increase of density of the hot phase induces the cooling rate and forms cold clouds again. In this way, 'self-regulation' is made up in quiescent star-forming galaxies.

The scale of thermal instability is much smaller than the resolution scale (the smoothing length in SPH simulations) even in isolated galaxy simulations, much more cosmological simulations. Therefore, Springel & Hernquist (2003) suggested a sub-grid model to mimic the multi-phase ISM via thermal instability in each SPH particle. The ART^2 first makes grids with smoothing physical parameters of inside SPH particles, and adapts the method of Springel & Hernquist (2003) to split gas into cold and hot phases (Li et al., 2008). We here briefly explain the method. It is based on the theory of McKee & Ostriker (1977). We assume primordial gas and ignore metal and molecular cooling for simplicity.

We assume that the two-phase medium has the balances between (1) star formation, (2) evaporation of cold clouds due to SN feedback and (3) cloud formation via thermal instability. The total density is composed by densities of cold clouds and hot ambient medium,

$$\rho = \rho_c + \rho_h. \tag{A.17}$$

The average thermal energy per unit volume is

$$\epsilon = \rho_c u_c + \rho_h u_h. \tag{A.18}$$

We set the time-scale of star formation to $t_\star$, and the change rate of stellar density is described as

$$\frac{d\rho_\star}{dt} = (1 - \beta)\frac{\rho_c}{t_\star}, \tag{A.19}$$

where β is a fraction of the mass returned to the ISM due to SN feedback, which is determined by the IMF. For Salpeter IMF with the range of $0.1-40\,\mathrm{M}_\odot$, $\beta = 0.106$. We thus set β to 0.1.

The SNe release the energy into hot phase medium,

$$\left.\frac{d}{dt}(\rho_h u_h)\right|_{\mathrm{SN}} = \epsilon_{\mathrm{SN}}\frac{d\rho_\star}{dt} = \beta u_{\mathrm{SN}}\frac{\rho_c}{t_\star}, \tag{A.20}$$

where $u_{\mathrm{SN}} = (1-\beta)\beta^{-1}\epsilon_{\mathrm{SN}}$ which corresponds to the supernova temperature, $T_{\mathrm{SN}} = 2\mu m_{\mathrm{H}} u_{\mathrm{SN}}/3k_{\mathrm{B}} \approx 10^8\,\mathrm{K}$. Also the SNe evaporate cold clouds and decrease the density,

$$\left.\frac{d\rho_c}{dt}\right|_{\mathrm{EV}} = A\beta\frac{\rho_c}{t_\star}, \tag{A.21}$$

where A represents the efficiency of evaporation. McKee & Ostriker (1977) showed that A depended on the local density as $A \propto \rho^{-4/5}$. To determine the normalization factor A_0, we require that temperature of the heated gas is in the range of thermal instability for primordial gas ($\sim 10^5 - 10^6\,\mathrm{K}$). Thus $T_{\mathrm{SN}}/A_0 = 10^5\,\mathrm{K}$ and $A_0 \approx 1000$.

The formation rate of cold clouds via thermal instability is written by

$$\left.\frac{d\rho_c}{dt}\right|_{\mathrm{TI}} = -\left.\frac{d\rho_h}{dt}\right|_{\mathrm{TI}} = \frac{1}{u_h - u_c}\Lambda_{\mathrm{net}}(\rho_h, u_h), \tag{A.22}$$

where Λ_{net} is the net cooling rate per volume (Katz et al., 1996). Below $T \sim 10^4\,\mathrm{K}$, Lyman-α cooling becomes inefficient and the cooling rate depends on the amount of metals and molecules (Eq. 3.14). However, we simply assume temperature of the cold gas is constant at $T_c = 1000\,\mathrm{K}$. We also assume that thermal instability occurs only in the gas whose density exceeds the threshold density ρ_{th}. This is motivated by the observational fact that the local galaxies have star formation only when the surface gas density is higher than some critical value ($\Sigma_{\mathrm{g,crit}} \sim 10\,\mathrm{M}_\odot\ \mathrm{pc}^{-2}$, Kennicutt, 1998).

By above descriptions, the basic equations are

$$\frac{d\rho_c}{dt} = -\frac{\rho}{t_\star} - A\beta\frac{\rho_c}{t_\star} + \frac{1-f}{u_h - u_c}\Lambda_{\mathrm{net}}(\rho_h, u_h), \tag{A.23}$$

$$\frac{d\rho_h}{dt} = \beta\frac{\rho}{t_\star} + A\beta\frac{\rho_c}{t_\star} - \frac{1-f}{u_h - u_c}\Lambda_{\mathrm{net}}(\rho_h, u_h). \tag{A.24}$$

The $f = 0$ represents the onset of thermal instability. The first term in the right hand side describes the effect of star formation, second term is for evaporation of cold clouds, and third term cloud formation via thermal instability. Also the energy budget is written by

$$\frac{d}{dt}(\rho_h u_h + \rho_c u_c) = -\Lambda_{\mathrm{net}}(\rho_h, u_h) + \beta\frac{\rho_c}{t_\star}u_{\mathrm{SN}} - (1-\beta)\frac{\rho_c}{t_\star}u_c. \tag{A.25}$$

In the gas of $\rho > \rho_{\rm th}$, cloud formation and evaporation due to SN feedback are balanced (self-regulated). We therefore expect that the effective pressure is constant in time,

$$P_{\rm eff} = (\gamma - 1)(\rho_h u_h + \rho_c u_c) = (\gamma - 1)\rho\,[(1 - x)u_h + x u_c] = (\gamma - 1)\rho u_{\rm eff}, \quad \text{(A.26)}$$

where $x \equiv \rho_c/\rho$ is mass fraction of cold phase. From this condition, we set the left hand side of equation A.25 to zero, then we obtain

$$\frac{\rho_c}{t_\star} = \frac{\Lambda_{\rm net}(\rho_h, u_h)}{\beta u_{\rm SN} - (1 - \beta)u_c}. \quad \text{(A.27)}$$

The ratio of cold and hot phases is

$$\frac{\rho_c}{\rho_h} = \frac{\rho_h}{\rho} y, \quad \text{(A.28)}$$

where

$$y \equiv \frac{t_\star \Lambda_{\rm net}(\rho, u_h)}{\rho\,[\beta u_{\rm SN} - (1 - \beta)u_c]}. \quad \text{(A.29)}$$

Using equations of (A.17) and (A.28), x is rewritten as

$$x = \frac{\rho_c}{\rho} = 1 + \frac{1}{2y} - \sqrt{\frac{1}{y} + \frac{1}{4y^2}}. \quad \text{(A.30)}$$

We have five free parameters i.e., A_0, $t_\star$, $\rho_{\rm th}$, β and $u_{\rm SN}$. The last two are decided from the IMF. We set $A_0 = 1000$ as described above. The $t_\star$ is related to the local dynamical time as $t_\star(\rho) = t_0^\star(\rho/\rho_{\rm th})^{-1/2}$. We require that the effective pressure is continuous function of density at $\rho = \rho_{\rm th}$. Ignoring radiative cooling of metals and molecules, temperature of gas whose density is just below $\rho_{\rm th}$ decreases to $\sim 10^4$ K, thus $u_{\rm eff}(\rho_{\rm th}) = u_4$. From Eq. (A.29) and $y = x/(1 - x)^2$,

$$\rho_{\rm th} = \frac{x_{\rm th}}{(1 - x_{\rm th})^2} \frac{\beta u_{\rm SN} - (1 - \beta)u_c}{t_0^\star L(u_{\rm SN}/A_0)}, \quad \text{(A.31)}$$

where $x_{\rm th} = (u_h - u_4)/(u_h - u_c) = 1 + (u_c - u_4)/(u_h - u_c) \approx 1 - A_0 u_4/u_{\rm SN}$ (from equation A.26), and $L(u) = \Lambda_{\rm net}(\rho, u)/\rho^2$ is the cooling function. Springel & Hernquist (2003) studied how the threshold density reproduces the cut-off of Kennicutt–Schmidt relation with changing $t_0^\star$, and showed the best fit value is 2.1 Gyr.

A.3 SN Energy Feedback

Massive stars crucially affect subsequent star formation via radiative and supernova (SN) feedback. SN heats surrounding medium up and induces outflow. In order to implement model of the SN feedback in SPH simulations, one naively should increase temperature of neighbor particles of a stellar particle. In fact, however, this SN feedback with state-of-the-art cosmological simulations (even with isolated case) would be very inefficient, because gas rapidly cools the injected energy before expands. The cause of the 'over-cooling problem' is that ratio of mass of heated gas by SN ($m_{\rm g,heat}$) to mass of the star ($m_\star$) is $\gg 1$ and the increment of temperature for each gas particle is low, resulting in that SN energy will be immediately cooled down. In reality, hot low-density bubble adiabatically expands with the ratio $m_{\rm g,heat}/m_\star \ll 1$ initially, and the expansion proceeds with momentum conservation after the swept gas mass becomes comparable with the ejecta mass.

Decreasing the mass of heated gas, one can avoid the computational problem. Dalla Vecchia & Schaye (2012) suggested the method saying that one should heat up only probablistically selected particles, not all neighbors. In the following, we describe the 'stochastic feedback model' briefly.

If we use the Chabrier IMF for the range of $[6, 100]\,{\rm M}_\odot$, we obtain the number of SNII sources per unit stellar mass, $n_{\rm SNII} = 1.736 \times 10^{-2}\,{\rm M}_\odot{}^{-1}$. Thus the total available energy provided SNII is given by,

$$\epsilon_{\rm SNII} = 8.73 \times 10^{15} \left(\frac{n_{\rm SNII}}{1.736 \times 10^{-2}\,{\rm M}_\odot{}^{-1}} \right) E_{51}\,{\rm erg\ g^{-1}}, \tag{A.32}$$

where $E_{\rm SNII} \equiv E_{51} \times 10\ 51\,{\rm erg}$ is the available energy from a single SNII event and we assume $E_{51} = 1$. For the energy conservation, the temperature increment per each particle is written by,

$$\begin{aligned} \Delta T &= (\gamma - 1)\frac{\mu m_{\rm H}}{k_{\rm B}} \epsilon_{\rm SNII} \frac{m_\star}{m_{\rm g,heat}} \\ &= 4.23 \times 10^7 \left(\frac{n_{\rm SNII}}{1.736 \times 10^{-2}\,{\rm M}_\odot{}^{-1}} \right) \left(\frac{\mu}{0.6} \right) E_{51} \frac{m_\star}{m_{\rm g,heat}}\,{\rm K}, \end{aligned} \tag{A.33}$$

where $\gamma = 5/3$ is the ratio of specific heats for an ideal monatomic gas, and μ is the mean molecular weight which becomes ~ 0.6 if we assume completely ionized primordial gas.

If we input thermal energy of SNII into all of the neighbor particles ($N_{\rm ngb} \approx 48$), the $m_\star/m_{\rm g,heat}$ ratio becomes $\ll 1$ and the temperature increases to $\Delta T \sim 10^6\,{\rm K}$, which will be immediately cooled especially in metal-enriched gas (Wiersma et al., 2009a). Meanwhile, if a few gas particles are heated by SNII, the temperature increment is $\Delta T \sim 10^7\,{\rm K}$ and the dominant cooling process is the Brehmsstrahlung radiation. The cooling rate depends on $T^{1/2}$, thus if once gas temperature rises upto $\gtrsim 10^7\,{\rm K}$, it would not be cooled rapidly and induce conversion of thermal energy into kinetic energy.

We give all of the neighbors same probability p of receiving energy from a star particle, irrespective of its mass and kernel weight. Drawing a random number $0 < r < 1$ for each gas-star pair, we increase the internal energy by $\Delta\epsilon$ if $r \geq p$. We require that the mean injected energy equals the energy contributed by star particle, $f_{\rm th} m_\star \epsilon_{\rm SNII}$, then the probability p follows,

$$p = f_{\rm th} \frac{\epsilon_{\rm SNII}}{\Delta\epsilon} \frac{m_\star}{\Sigma_{i=1}^{N_{\rm ngb}} m_i}, \tag{A.34}$$

where $f_{\rm th}$ is the fraction of total themally available SNII energy, and $\Delta\epsilon$ is the amount of thermal energy per unit mass that is given to each heated gas particles. The expectation value of the number of heated neighbors is described as,

$$\begin{aligned} \langle N_{\rm heat} \rangle &= p N_{\rm ngb} \\ &= 1.34\, E_{51} \left(\frac{n_{\rm SNII}}{1.736 \times 10^{-2}\,{\rm M_\odot}} \right) \left(\frac{\mu}{0.6} \right) f_{\rm th} \left(\frac{\Delta T}{10^{7.5}\,{\rm K}} \right)^{-1}. \end{aligned} \tag{A.35}$$

To ensure that indeed the stochastic feedback model is effective, here we compare the sound crossing time ($t_{\rm sc}$) and cooling time ($t_{\rm cool}$). If $t_{\rm sc} < t_{\rm cool}$, SN heated particles can efficiently convert the thermal energy into kinetic energy of surrounding gas. The sound crossing time is estimated using the smoothing length h of the resolution element,

$$\begin{aligned} t_{\rm sc} &= \frac{h}{c_s} = \left(\frac{\mu m_{\rm H}}{\gamma k_{\rm B}} \right)^{1/2} \frac{h}{T^{1/2}} \\ &= 2.3 \times 10^4 \left(\frac{\mu}{0.6} \right)^{1/2} \left(\frac{T}{10^{7.5}\,{\rm K}} \right)^{-1/2} \left(\frac{h}{20\,{\rm pc}} \right) {\rm yr}, \end{aligned} \tag{A.36}$$

where c_s is the local sound speed. Here we set h to the minimum value in our zoom-in simulations. Meanwhile, the cooling time is described as,

$$t_{\rm cool} = \frac{u}{\Lambda} = \frac{\rho\epsilon}{\Lambda}, \tag{A.37}$$

where u and Λ are internal energy and radiative cooling rate per unit volume, respectively. If temperature is higher than $\sim 10^7\,{\rm K}$, the cooling rate is dominated by the free-free emission (the Brehmsstrahlung radiation):

$$\begin{aligned} \Lambda &\approx 7.99 \times 10^{-22} \left(\frac{n_{\rm H}}{10\,{\rm cm^{-3}}} \right)^2 \left(\frac{T}{10^{7.5}\,{\rm K}} \right)^{1/2} g_{\rm f} \eta_{\rm e} (\eta_{\rm H_{II}} + \eta_{\rm He_{II}} + \eta_{\rm He_{III}}) \qquad (A.38) \\ &\approx 1.12 \times 10^{-21} \left(\frac{n_{\rm H}}{10\,{\rm cm^{-3}}} \right)^2 \left(\frac{T}{10^{7.5}\,{\rm K}} \right)^{1/2} \frac{(1+X_{\rm H})(1+3X_{\rm H})}{8X_{\rm H}^2} {\rm erg\ cm^{-3}\ s^{-1}}, \end{aligned}$$

where $g_{\rm f} \approx 1.4$ is the Gaunt factor, $\eta_i = n_i/n_{\rm H}$ is the relative abundance ratio of species i to hydrogen, and $X_{\rm H}$ is hydrogen mass fraction. At the second equality, we assume the plasma is completely ionized. Here we set $n_{\rm H}$ to the threshold value above which star formation occurs in our simulations. Then, we obtain the cooling time of

$$t_{\rm cool} \approx 3.26 \times 10^6 \left(\frac{n_{\rm H}}{10\,{\rm cm^{-3}}} \right)^{-1} \left(\frac{T}{10^{7.5}\,{\rm K}} \right)^{1/2} \left(\frac{\mu}{0.6} \right)^{1/2} \left(\frac{f(X_{\rm H})}{0.13} \right) {\rm yr}, \tag{A.39}$$

where

$$f(X_{\rm H}) = X_{\rm H}(1+X_{\rm H})^{-1}(1+3X_{\rm H})^{-1}, \tag{A.40}$$

and $f(X_{\rm H}=0.752) \approx 0.13$.

Using the SPH smoothing kernel function,

$$h \approx \left(\frac{3}{4\pi}\frac{\Sigma_{i=1}^{N_{\rm ngb}} m_i}{\rho}\right)^{1/3} \approx \left(\frac{3}{4\pi}\frac{N_{\rm ngb}\langle m\rangle}{m_{\rm H} n_{\rm H}} X_{\rm H}\right)^{1/3}, \tag{A.41}$$

where $\langle m\rangle$ is the average particle mass, and Eqs. (A.36) and (A.39), we obtain

$$\begin{aligned}\frac{t_{\rm cool}}{t_{\rm sc}} \approx 38 \left(\frac{n_{\rm H}}{10\,{\rm cm}^{-3}}\right)^{-2/3} \left(\frac{T}{10^{7.5}\,{\rm K}}\right) \left(\frac{\langle m\rangle}{1.2\times10^4\,{\rm M}_\odot}\right)^{-1/3} \times \\ \left(\frac{N_{\rm ngb}}{48}\right)^{-1/3} \left(\frac{\mu}{0.6}\right)^{-3/2} \left(\frac{g(X_{\rm H})}{0.14}\right),\end{aligned} \tag{A.42}$$

where $g(X_{\rm H}) = X_{\rm H}^{-1/3} f(X_{\rm H})$. Here we set $\langle m\rangle$ to the initial mass of gas particle in our zoom simulations. The exact value of $f_t = t_{\rm cool}/t_{\rm sc}$ can only be determined using simulations, but we expect it to be similar to 10. This agrees well with independent work of Creasey et al. (2011), who showed the resolution criteria for avoiding the numerical over-cooling at the shock front. Requiring $t_{\rm cool} = f_t t_{\rm sc}$, we find the critical density under which the feedback is expected to be effective,

$$\begin{aligned}n_{\rm H,crit} \approx 75 \left(\frac{T}{10^{7.5}\,{\rm K}}\right)^{3/2} \left(\frac{f_t}{10}\right)^{-3/2} \left(\frac{\langle m\rangle}{1.2\times10^4\,{\rm M}_\odot}\right)^{-1/2} \times \\ \left(\frac{N_{\rm ngb}}{48}\right)^{-1/2} \left(\frac{\mu}{0.6}\right)^{-9/4} \left(\frac{g(X_{\rm H})}{0.14}\right)^{3/2} {\rm cm}^{-3}.\end{aligned} \tag{A.43}$$

Eq. (2.14) is derived from this equation. Note that it depends on $T^{3/2}\langle m\rangle^{-1/2}$.

Bibliography

Abel T., Bryan G. L., Norman M. L., *2002*, Science, 295, 93

Agertz O., Teyssier R., Moore B., *2011*, MNRAS, 410, 1391

Aggarwal K. M., Keenan F. P., *1999*, ApJS, 123, 311

Altay G., Theuns T., Schaye J., Crighton N. H. M., Dalla Vecchia C., *2011*, ApJL, 737, L37

Anderson L., et al.,*2014*, MNRAS, 441, 24

Andre P., Ward-Thompson D., Motte F., *1996*, A&A, 314, 625

Anglés-Alcázar D., Faucher-Giguère C.-A., Quataert E., Hopkins P. F., Feldmann R., Torrey P., Wetzel A., Kereš D., *2017*, MNRAS, 472, L109

Aoyama S., Hou K.-C., Shimizu I., Hirashita H., Todoroki K., Choi J.-H., Nagamine K., *2017*, MNRAS, 466, 105

Aoyama S., Hou K.-C., Hirashita H., Nagamine K., Shimizu I., *2018*, MNRAS, 478, 4905

Arata S., Yajima H., Nagamine K., *2018*, MNRAS, 475, 4252

Arata S., Yajima H., Nagamine K., Li Y., Khochfar S., *2019*, MNRAS, 488, 2629

Arata S., Yajima H., Nagamine K., Abe M., Khochfar S., *2020*, arXiv e-prints, p. arXiv:2001.01853

Asano R. S., Takeuchi T. T., Hirashita H., Inoue A. K., *2013*, Earth, Planets, and Space, 65, 213

Bakx T. J. L. C., et al.,*2020*, arXiv e-prints, p. arXiv:2001.02812

Barkana R., Loeb A., *2001*, PhyRev, 349, 125

Barrow K. S. S., Wise J. H., Aykutalp A., O'Shea B. W., Norman M. L., Xu H., *2018*, MNRAS, 474, 2617

Becker G. D., Bolton J. S., Lidz A., *2015*, PASA, 32, e045

Behrens C., Pallottini A., Ferrara A., Gallerani S., Vallini L., *2018*, MNRAS, 477, 552

Bennett C. L., et al.,*1996*, ApJL, 464, L1

Bennett C. L., et al.,*2013*, ApJS, 208, 20

Berg D. A., Erb D. K., Henry R. B. C., Skillman E. D., McQuinn K. B. W., *2019*, ApJ, 874, 93

Bianchi S., Schneider R., *2007*, MNRAS, 378, 973

Bird S., Vogelsberger M., Sijacki D., Zaldarriaga M., Springel V., Hernquist L., *2013*, MNRAS, 429, 3341

Bjorkman J. E., Wood K., *2001*, ApJ, 554, 615

Blitz L., Rosolowsky E., *2006*, ApJ, 650, 933

Blumenthal G. R., Faber S. M., Primack J. R., Rees M. J., *1984*, Nature, 311, 517

Booth C. M., Schaye J., *2009*, MNRAS, 398, 53

Bouwens R. J., Illingworth G. D., Blakeslee J. P., Franx M., *2006*, ApJ, 653, 53

Bouwens R. J., et al.,*2011*, ApJ, 737, 90

Bouwens R. J., et al.,*2015*, ApJ, 803, 34

Bouwens R. J., Aravena M., Decarli R., Walter F., da Cunha E., Labbé I., Bauer F. E., Bertoldi F. e. a., *2016*, ApJ, 833, 72

Bovill M. S., Ricotti M., *2011a*, ApJ, 741, 17

Bovill M. S., Ricotti M., *2011b*, ApJ, 741, 18

Bowler R. A. A., et al.,*2015*, MNRAS, 452, 1817

Bowler R. A. A., Bourne N., Dunlop J. S., McLure R. J., McLeod D. J., *2018*, MNRAS, 481, 1631

Boylan-Kolchin M., Springel V., White S. D. M., Jenkins A., Lemson G., *2009*, MNRAS, 398, 1150

Brocklehurst M., *1971*, MNRAS, 153, 471

Brodie J. P., Strader J., *2006*, ARA&A, 44, 193

Bromm V., Loeb A., *2003*, Nature, 425, 812

Bromm V., Yoshida N., *2011*, ARA&A, 49, 373

Bromm V., Yoshida N., Hernquist L., McKee C. F., *2009*, Nature, 459, 49

Bruzual G., Charlot S., *2003*, MNRAS, 344, 1000

Calzetti D., Kinney A. L., Storchi-Bergmann T., *1994*, ApJ, 429, 582

Calzetti D., Armus L., Bohlin R. C., Kinney A. L., Koornneef J., Storchi-Bergmann T., *2000*, ApJ, 533, 682

Capak P. L., et al.,*2015*, Nature, 522, 455

Carniani S., et al.,*2017*, A&A, 605, A42

Casey C. M., et al.,*2014*, ApJ, 796, 95

Casey C. M., Hodge J., Zavala J. A., Spilker J., da Cunha E., Staguhn J., Finkelstein S. L., Drew P., *2018*, ApJ, 862, 78

Cen R., Ostriker J., *1992*, ApJ, 393, 22

Chabrier G., *2003*, PASP, 115, 763

Chapman S. C., Blain A. W., Smail I., Ivison R. J., *2005*, ApJ, 622, 772

Chiaki G., Yoshida N., Kitayama T., *2013a*, ApJ, 762, 50

Chiaki G., Nozawa T., Yoshida N., *2013b*, ApJL, 765, L3

Chiaki G., Marassi S., Nozawa T., Yoshida N., Schneider R., Omukai K., Limongi M., Chieffi A., *2015*, MNRAS, 446, 2659

Choi J.-H., Nagamine K., *2011*, MNRAS, 410, 2579

Cormier D., Lebouteiller V., Madden S. C., Abel N., Hony S., Galliano F., Baes M., Barlow M. J. e. a., *2012*, A&A, 548, A20

Cormier D., Madden S. C., Lebouteiller V., Abel N., Hony S., Galliano F., Rémy-Ruyer A., Bigiel F. e. a., *2015*, A&A, 578, A53

Couchman H. M. P., Rees M. J., *1986*, MNRAS, 221, 53

Crain R. A., et al.,*2015*, MNRAS, 450, 1937

Creasey P., Theuns T., Bower R. G., Lacey C. G., *2011*, MNRAS, 415, 3706

Croxall K. V., et al.,*2017*, ApJ, 845, 96

Cullen F., McLure R. J., Khochfar S., Dunlop J. S., Dalla Vecchia C., *2017*, MNRAS, 470, 3006

Cullen F., et al.,*2018*, MNRAS, 476, 3218

Dalla Vecchia C., Schaye J., *2008*, MNRAS, 387, 1431

Dalla Vecchia C., Schaye J., *2012*, MNRAS, 426, 140

Davis M., Efstathiou G., Frenk C. S., White S. D. M., *1985*, ApJ, 292, 371

Davis S. W., Jiang Y.-F., Stone J. M., Murray N., *2014*, ApJ, 796, 107

De Looze I., et al.,*2014*, A&A, 568, A62

De Lucia G., Blaizot J., *2007*, MNRAS, 375, 2

Dekel A., Birnboim Y., *2006*, MNRAS, 368, 2

Dekel A., Birnboim Y., *2008*, MNRAS, 383, 119

Dekel A., et al.,*2009*, Nature, 457, 451

Delubac T., et al.,*2015*, A&A, 574, A59

Dey A., Spinrad H., Stern D., Graham J. R., Chaffee F. H., *1998*, ApJL, 498, L93

Di Matteo T., Springel V., Hernquist L., *2005*, Nature, 433, 604

Di Matteo T., Colberg J., Springel V., Hernquist L., Sijacki D., *2008*, ApJ, 676, 33

Di Matteo T., Khandai N., DeGraf C., Feng Y., Croft R. A. C., Lopez J., Springel V., *2012*, ApJL, 745, L29

Díaz-Santos T., et al.,*2014*, ApJL, 788, L17

Dijkstra M., *2014*, PASA, 31, e040

Dijkstra M., Loeb A., *2009*, MNRAS, 400, 1109

Dijkstra M., Wyithe J. S. B., *2010*, MNRAS, 408, 352

Dijkstra M., Haiman Z., Rees M. J., Weinberg D. H., *2004*, ApJ, 601, 666

Dijkstra M., Lidz A., Wyithe J. S. B., *2007*, MNRAS, 377, 1175

Dijkstra M., Haiman Z., Mesinger A., Wyithe J. S. B., *2008*, MNRAS, 391, 1961

Draine B. T., Bertoldi F., *1996*, ApJ, 468, 269

Draine B. T., et al.,*2007*, ApJ, 663, 866

Efstathiou G., *1992*, MNRAS, 256, 43P

Eisenstein D. J., Hu W., *1998*, ApJ, 496, 605

Eisenstein D. J., et al.,*2005*, ApJ, 633, 560

El-Badry K., Wetzel A., Geha M., Hopkins P. F., Kereš D., Chan T. K., Faucher-Giguère C.-A., *2016*, ApJ, 820, 131

Fabian A. C., *1999*, MNRAS, 308, L39

Faisst A. L., et al.,*2017*, ApJ, 847, 21

Fall S. M., Rees M. J., *1985*, ApJ, 298, 18

Fall S. M., Romanowsky A. J., *2013*, ApJL, 769, L26

Fan X., et al.,*2006*, AJ, 132, 117

Faucher-Giguère C.-A., Kereš D., Dijkstra M., Hernquist L., Zaldarriaga M., *2010*, ApJ, 725, 633

Ferkinhoff C., Hailey-Dunsheath S., Nikola T., Parshley S. C., Stacey G. J., Benford D. J., Staguhn J. G., *2010*, ApJL, 714, L147

Ferland G. J., Korista K. T., Verner D. A., Ferguson J. W., Kingdon J. B., Verner E. M., *1998*, PASP, 110, 761

Ferrara A., Hirashita H., Ouchi M., Fujimoto S., *2017*, MNRAS, 471, 5018

Ferrarese L., Merritt D., *2000*, ApJL, 539, L9

Field G. B., *1965*, ApJ, 142, 531

Finkelstein S. L., et al.,*2015*, ApJ, 810, 71

Fujimoto S., et al.,*2019*, arXiv e-prints, p. arXiv:1902.06760

Furlanetto S. R., Zaldarriaga M., Hernquist L., *2004*, ApJ, 613, 1

Furlanetto S. R., Oh S. P., Briggs F. H., *2006*, PhR, 433, 181

Galli D., Palla F., *1998*, A&A, 335, 403

Genel S., Fall S. M., Hernquist L., Vogelsberger M., Snyder G. F., Rodriguez-Gomez V., Sijacki D., Springel V., *2015*, ApJL, 804, L40

Genzel R., Tacconi L. J., Gracia-Carpio J., Sternberg A., Cooper M. C., Shapiro K., Bolatto A., Bouché N. et al., *2010*, MNRAS, 407, 2091

Ginolfi M., et al.,*2019*, arXiv e-prints, p. arXiv:1910.04770

Glover S. C. O., Jappsen A. K., *2007*, ApJ, 666, 1

Gnedin N. Y., *2000a*, ApJ, 535, 530

Gnedin N. Y., *2000b*, ApJ, 542, 535

Gnedin N. Y., Kravtsov A. V., *2011*, ApJ, 728, 88

Gnedin N. Y., Kravtsov A. V., Chen H.-W., *2008*, ApJ, 672, 765

Goldsmith P. F., Langer W. D., Pineda J. L., Velusamy T., *2012*, ApJS, 203, 13

Granato G. L., De Zotti G., Silva L., Bressan A., Danese L., *2004*, ApJ, 600, 580

Grazian A., et al.,*2011*, A&A, 532, A33

Greif T. H., Johnson J. L., Klessen R. S., Bromm V., *2008*, MNRAS, 387, 1021

Greif T. H., Glover S. C. O., Bromm V., Klessen R. S., *2010*, ApJ, 716, 510

Grogin N. A., et al.,*2011*, ApJS, 197, 35

Gunn J. E., Peterson B. A., *1965*, ApJ, 142, 1633

Guo Q., et al.,*2011*, MNRAS, 413, 101

Guth A. H., *1981*, Physical Review D, 23, 347

Haardt F., Madau P., *1996*, ApJ, 461, 20

Haardt F., Madau P., 2001, in Neumann D. M., Tran J. T. V., eds, Clusters of Galaxies and the High Redshift Universe Observed in X-rays. p. 64 (`arXiv:astro-ph/0106018`)

Haardt F., Madau P., *2012*, ApJ, 746, 125

Hahn O., Abel T., *2011*, MNRAS, 415, 2101

Haiman Z., Thoul A. A., Loeb A., *1996*, ApJ, 464, 523

Haiman Z., Rees M. J., Loeb A., *1997*, ApJ, 476, 458

Harikane Y., et al.,*2018*, ApJ, 859, 84

Harikane Y., et al.,*2019*, arXiv e-prints, p. arXiv:1910.10927

Hashimoto T., et al.,*2018*, Nature, 557, 392

Hashimoto T., et al.,*2019*, PASJ, 71, 71

Hawking S. W., *1982*, Physics Letters B, 115, 295

Herrera-Camus R., et al.,*2018a*, ApJ, 861, 94

Herrera-Camus R., et al.,*2018b*, ApJ, 861, 95

Hinshaw G., et al.,*2013*, ApJS, 208, 19

Hopkins P. F., Hernquist L., Cox T. J., Di Matteo T., Robertson B., Springel V., *2006*, ApJS, 163, 1

Hopkins P. F., Cox T. J., Hernquist L., Narayanan D., Hayward C. C., Murray N., *2013*, MNRAS, 430, 1901

Hopkins P. F., Kereš D., Oñorbe J., Faucher-Giguère C.-A., Quataert E., Murray N., Bullock J. S., *2014*, MNRAS, 445, 581

Hopkins P. F., et al.,*2018*, MNRAS, 480, 800

Hu E. M., Cowie L. L., McMahon R. G., Capak P., Iwamuro F., Kneib J. P., Maihara T., Motohara K., *2002*, ApJL, 568, L75

Hwang H. S., Elbaz D., Magdis G., Daddi E., Symeonidis M., Altieri B., Amblard A., Andreani P. et al., *2010*, MNRAS, 409, 75

Iliev I. T., Mellema G., Pen U.-L., Merz H., Shapiro P. R., Alvarez M. A., *2006*, MNRAS, 369, 1625

Iliev I. T., Mellema G., Shapiro P. R., Pen U.-L., *2007*, MNRAS, 376, 534

Illingworth G. D., et al.,*2013*, ApJS, 209, 6

Inoue A. K., *2003*, PASJ, 55, 901

Inoue A. K., *2011*, MNRAS, 415, 2920

Inoue T., Omukai K., *2015*, ApJ, 805, 73

Inoue A. K., Shimizu I., Tamura Y., Matsuo H., Okamoto T., Yoshida N., *2014*, ApJL, 780, L18

Inoue A. K., et al.,*2016*, Science, 352, 1559

Inoue A. K., et al.,*2018*, PASJ, 70, 55

Ivison R. J., et al.,*2010a*, A&A, 518, L35

Ivison R. J., et al.,*2010b*, A&A, 518, L35

Jaacks J., Choi J.-H., Nagamine K., Thompson R., Varghese S., *2012a*, MNRAS, 420, 1606

Jaacks J., Nagamine K., Choi J. H., *2012b*, MNRAS, 427, 403

Johnson J. L., Dalla Vecchia C., Khochfar S., *2013*, MNRAS, 428, 1857

Kashikawa N., et al.,*2006*, ApJ, 648, 7

Kashikawa N., et al.,*2011*, ApJ, 734, 119

Katz N., Weinberg D. H., Hernquist L., *1996*, ApJS, 105, 19

Katz H., Sijacki D., Haehnelt M. G., *2015*, MNRAS, 451, 2352

Katz H., et al.,*2019*, MNRAS, 487, 5902

Kauffmann G., Haehnelt M., *2000*, MNRAS, 311, 576

Kauffmann G., White S. D. M., Guiderdoni B., *1993*, MNRAS, 264, 201

Kauffmann G., Colberg J. M., Diaferio A., White S. D. M., *1999*, MNRAS, 303, 188

Kawamata R., Ishigaki M., Shimasaku K., Oguri M., Ouchi M., Tanigawa S., *2018*, ApJ, 855, 4

Kennicutt Jr. R. C., *1998*, ARA&A, 36, 189

Kereš D., Katz N., Weinberg D. H., Davé R., *2005*, MNRAS, 363, 2

Kereš D., Katz N., Fardal M., Davé R., Weinberg D. H., *2009*, MNRAS, 395, 160

Kim H.-S., Wyithe J. S. B., Raskutti S., Lacey C. G., Helly J. C., *2013*, MNRAS, 428, 2467

Kim J.-h., et al.,*2018*, MNRAS, 474, 4232

Kimm T., Cen R., *2014*, ApJ, 788, 121

Kimm T., Cen R., Rosdahl J., Yi S. K., *2016*, ApJ, 823, 52

King A., *2003*, ApJL, 596, L27

Knudsen K. K., Watson D., Frayer D., Christensen L., Gallazzi A., Michałowski M. J., Richard J., Zavala J., *2017*, MNRAS, 466, 138

Komatsu E., et al.,*2009*, ApJS, 180, 330

Konno A., et al.,*2014*, ApJ, 797, 16

Kormendy J., Ho L. C., *2013*, ARA&A, 51, 511

Kovács A., Chapman S. C., Dowell C. D., Blain A. W., Ivison R. J., Smail I., Phillips T. G., *2006*, ApJ, 650, 592

Kowalski M., et al.,*2008*, ApJ, 686, 749

Koyama H., Inutsuka S.-i., *2002*, ApJL, 564, L97

Kravtsov A. V., *2003*, ApJL, 590, L1

Kravtsov A. V., Gnedin O. Y., *2005*, ApJ, 623, 650

Kruijssen J. M. D., *2015*, MNRAS, 454, 1658

Krumholz M. R., McKee C. F., *2005*, ApJ, 630, 250

Kuo T.-M., Hirashita H., *2012*, MNRAS, 424, L34

Lacey C., Cole S., *1993*, MNRAS, 262, 627

Lagache G., Cousin M., Chatzikos M., *2018*, A&A, 609, A130

Laor A., Draine B. T., *1993*, ApJ, 402, 441

Laporte N., et al.,*2017*, ApJL, 837, L21

Laporte N., et al.,*2019*, MNRAS, 487, L81

Larson D., et al.,*2011*, ApJS, 192, 16

Leitherer C., et al.,*1999*, ApJS, 123, 3

Li Y., et al.,*2007*, ApJ, 665, 187

Li Y., et al.,*2008*, ApJ, 678, 41

Liu H.-M., Hirashita H., *2019*, MNRAS, 490, 540

Lotz J. M., et al.,*2017*, ApJ, 837, 97

Luhman M. L., Satyapal S., Fischer J., Wolfire M. G., Sturm E., Dudley C. C., Lutz D., Genzel R., *2003*, ApJ, 594, 758

Luo Y., Shlosman I., Nagamine K., Fang T., *2019*, arXiv e-prints, p. arXiv:1910.07556

Ma X., Kasen D., Hopkins P. F., Faucher-Giguère C.-A., Quataert E., Kereš D., Murray N., *2015*, MNRAS, 453, 960

Ma X., et al.,*2018*, MNRAS, 477, 219

Ma X., et al.,*2019*, MNRAS, 487, 1844

Madau P., Dickinson M., *2014*, ARA&A, 52, 415

Madden S. C., et al.,*2013*, PASP, 125, 600

Magorrian J., et al.,*1998*, AJ, 115, 2285

Maio U., Ciardi B., Dolag K., Tornatore L., Khochfar S., *2010*, MNRAS, 407, 1003

Maio U., Khochfar S., Johnson J. L., Ciardi B., *2011*, MNRAS, 414, 1145

Maiolino R., Schneider R., Oliva E., Bianchi S., Ferrara A., Mannucci F., Pedani M., Roca Sogorb M., *2004*, Nature, 431, 533

Malhotra S., Rhoads J. E., *2004*, ApJL, 617, L5

Mandelker N., Padnos D., Dekel A., Birnboim Y., Burkert A., Krumholz M. R., Steinberg E., *2016*, MNRAS, 463, 3921

Mandelker N., van Dokkum P. G., Brodie J. P., van den Bosch F. C., Ceverino D., *2018*, ApJ, 861, 148

Marigo P., *2001*, A&A, 370, 194

Marrone D. P., Spilker J. S., Hayward C. C., Vieira J. D., Aravena M., Ashby M. L. N., Bayliss M. B., Béthermin M. et al., *2018*, Nature, 553, 51

Mather J. C., et al.,*1990*, ApJL, 354, L37

McKee C. F., Ostriker J. P., *1977*, ApJ, 218, 148

McKinnon R., Torrey P., Vogelsberger M., *2016*, MNRAS, 457, 3775

McKinnon R., Vogelsberger M., Torrey P., Marinacci F., Kannan R., *2018*, MNRAS, 478, 2851

McQuinn M., Hernquist L., Zaldarriaga M., Dutta S., *2007*, MNRAS, 381, 75

Mellema G., Iliev I. T., Pen U.-L., Shapiro P. R., *2006*, MNRAS, 372, 679

Meurer G. R., Heckman T. M., Calzetti D., *1999*, ApJ, 521, 64

Mihos J. C., Hernquist L., *1994*, ApJ, 437, 611

Mo H. J., Mao S., White S. D. M., *1998*, MNRAS, 295, 319

Moore B., Diemand J., Madau P., Zemp M., Stadel J., *2006*, MNRAS, 368, 563

Morales M. F., Wyithe J. S. B., *2010*, ARA&A, 48, 127

Moriwaki K., et al.,*2018*, MNRAS, 481, L84

Muñoz J. A., Oh S. P., *2016*, MNRAS, 463, 2085

Muratov A. L., Kereš D., Faucher-Giguère C.-A., Hopkins P. F., Quataert E., Murray N., *2015*, MNRAS, 454, 2691

Murray N., Ménard B., Thompson T. A., *2011*, ApJ, 735, 66

Nagamine K., Wolfe A. M., Hernquist L., *2006*, ApJ, 647, 60

Nagamine K., Choi J.-H., Yajima H., *2010*, ApJL, 725, L219

Nahar S. N., *1999*, ApJS, 120, 131

Nahar S. N., Pradhan A. K., *1997*, ApJS, 111, 339

Narayanan D., Krumholz M. R., *2017*, MNRAS, 467, 50

Narayanan D., Davé R., Johnson B. D., Thompson R., Conroy C., Geach J., *2018a*, MNRAS, 474, 1718

Narayanan D., Conroy C., Davé R., Johnson B. D., Popping G., *2018b*, ApJ, 869, 70

Navarro J. F., Frenk C. S., White S. D. M., *1996*, ApJ, 462, 563

Navarro J. F., Frenk C. S., White S. D. M., *1997*, ApJ, 490, 493

Nelson D., Vogelsberger M., Genel S., Sijacki D., Kereš D., Springel V., Hernquist L., *2013*, MNRAS, 429, 3353

Neri R., Downes D., Cox P., Walter F., *2014*, A&A, 562, A35

Nozawa T., Kozasa T., Habe A., Dwek E., Umeda H., Tominaga N., Maeda K., Nomoto K., *2007*, ApJ, 666, 955

Nussbaumer H., Storey P. J., *1981*, A&A, 99, 177

Oesch P. A., Brammer G., van Dokkum P. G., Illingworth G. D., Bouwens R. J., Labbé I., Franx M., Momcheva I. et al., *2016*, ApJ, 819, 129

Oh S. P., Haiman Z., *2002*, ApJ, 569, 558

Okamoto T., Shimizu I., Yoshida N., *2014*, PASJ, 66, 70

Olsen K., Greve T. R., Narayanan D., Thompson R., Davé R., Niebla Rios L., Stawinski S., *2017*, ApJ, 846, 105

Omukai K., Tsuribe T., Schneider R., Ferrara A., *2005*, ApJ, 626, 627

Omukai K., Schneider R., Haiman Z., *2008*, ApJ, 686, 801

Ono Y., et al.,*2012*, ApJ, 744, 83

Ono Y., et al.,*2018*, PASJ, 70, S10

Oppenheimer B. D., Davé R., *2006*, MNRAS, 373, 1265

Ouchi M., Yamada T., Kawai H., Ohta K., *1999*, ApJL, 517, L19

Ouchi M., et al.,*2004*, ApJ, 611, 660

Ouchi M., et al.,*2008*, ApJS, 176, 301

Ouchi M., et al.,*2009*, ApJ, 706, 1136

Ouchi M., et al.,*2010*, ApJ, 723, 869

Ouchi M., et al.,*2013*, ApJ, 778, 102

Paardekooper J.-P., Khochfar S., Dalla Vecchia C., *2015*, MNRAS, 451, 2544

Pallottini A., Ferrara A., Gallerani S., Vallini L., Maiolino R., Salvadori S., *2017*, MNRAS, 465, 2540

Pallottini A., et al.,*2019*, MNRAS, 487, 1689

Partridge R. B., Peebles P. J. E., *1967*, ApJ, 147, 868

Peebles P. J. E., Ratra B., *1988*, ApJL, 325, L17

Peebles P. J., Ratra B., *2003*, Reviews of Modern Physics, 75, 559

Percival W. J., Cole S., Eisenstein D. J., Nichol R. C., Peacock J. A., Pope A. C., Szalay A. S., *2007*, MNRAS, 381, 1053

Percival W. J., et al.,*2010*, MNRAS, 401, 2148

Perlmutter S., et al.,*1999*, ApJ, 517, 565

Petkova M., Springel V., *2011*, MNRAS, 412, 935

Pillepich A., et al.,*2018*, MNRAS, 473, 4077

Planck Collaboration et al., *2014*, A&A, 571, A16

Planck Collaboration et al., *2016*, A&A, 594, A13

Planck Collaboration et al., *2018*, arXiv e-prints, p. arXiv:1807.06209

Portinari L., Chiosi C., Bressan A., *1998*, A&A, 334, 505

Press W. H., Schechter P., *1974*, APJ, 187, 425

Prieto J. L., Gnedin O. Y., *2008*, ApJ, 689, 919

Rahmati A., Pawlik A. H., Raičević M., Schaye J., *2013*, MNRAS, 430, 2427

Rauch M., *1998*, ARA&A, 36, 267

Reed D., Gardner J., Quinn T., Stadel J., Fardal M., Lake G., Governato F., *2003*, MNRAS, 346, 565

Rees M. J., Ostriker J. P., *1977*, MNRAS, 179, 541

Rhoads J. E., Malhotra S., *2001*, ApJ, 563, L5

Richings A. J., Schaye J., Oppenheimer B. D., *2014a*, MNRAS, 440, 3349

Richings A. J., Schaye J., Oppenheimer B. D., *2014b*, MNRAS, 442, 2780

Ricotti M., Gnedin N. Y., *2005*, ApJ, 629, 259

Ricotti M., Gnedin N. Y., Shull J. M., *2002a*, ApJ, 575, 33

Ricotti M., Gnedin N. Y., Shull J. M., *2002b*, ApJ, 575, 49

Ricotti M., Parry O. H., Gnedin N. Y., *2016*, ApJ, 831, 204

Riechers D. A., Bradford C. M., Clements D. L., Dowell C. D., Pérez-Fournon I., Ivison R. J., Bridge C., Conley A. et al., *2013*, Nature, 496, 329

Riess A. G., et al., *1998*, AJ, 116, 1009

Riess A. G., et al., *2004*, ApJ, 607, 665

Riess A. G., et al., *2007*, ApJ, 659, 98

Robertson B. E., Ellis R. S., Furlanetto S. R., Dunlop J. S., *2015*, ApJL, 802, L19

Rosolowsky E., *2005*, PASP, 117, 1403

Rosolowsky E., *2007*, ApJ, 654, 240

Rybak M., et al.,*2019*, ApJ, 876, 112

Safranek-Shrader C., Agarwal M., Federrath C., Dubey A., Milosavljević M., Bromm V., *2012*, MNRAS, 426, 1159

Safranek-Shrader C., Milosavljević M., Bromm V., *2014*, MNRAS, 438, 1669

Saitoh T. R., *2017*, AJ, 153, 85

Scannapieco C., Tissera P. B., White S. D. M., Springel V., *2008*, MNRAS, 389, 1137

Schaye J., *2004*, ApJ, 609, 667

Schaye J., Dalla Vecchia C., *2008*, MNRAS, 383, 1210

Schaye J., et al.,*2010*, MNRAS, 402, 1536

Schaye J., et al.,*2015*, MNRAS, 446, 521

Seo H.-J., Eisenstein D. J., *2003*, ApJ, 598, 720

Seon K.-I., Edelstein J., Korpela E., Witt A., Min K.-W., Han W., Shinn J., Kim I.-J. e. a., *2011*, ApJS, 196, 15

Shapiro P. R., Iliev I. T., Raga A. C., *2004*, MNRAS, 348, 753

Shapley A. E., *2011*, ARA&A, 49, 525

Sheth R. K., Tormen G., *1999*, MNRAS, 308, 119

Sheth R. K., Tormen G., *2002*, MNRAS, 329, 61

Shimasaku K., et al.,*2006*, PASJ, 58, 313

Shimizu I., Todoroki K., Yajima H., Nagamine K., *2019*, MNRAS, 484, 2632

Sijacki D., Vogelsberger M., Genel S., Springel V., Torrey P., Snyder G. F., Nelson D., Hernquist L., *2015*, MNRAS, 452, 575

Silk J., Rees M. J., *1998*, A&A, 331, L1

Smoot G. F., et al.,*1992*, ApJL, 396, L1

Solomon P. M., Rivolo A. R., Barrett J., Yahil A., *1987*, ApJ, 319, 730

Somerville R. S., Kolatt T. S., *1999*, MNRAS, 305, 1

Somerville R. S., Hopkins P. F., Cox T. J., Robertson B. E., Hernquist L., *2008*, MNRAS, 391, 481

Spergel D. N., et al.,*2003*, ApJS, 148, 175

Spergel D. N., et al.,*2007*, ApJS, 170, 377

Springel V., *2000*, MNRAS, 312, 859

Springel V., *2005*, MNRAS, 364, 1105

Springel V., Hernquist L., *2003*, MNRAS, 339, 289

Springel V., Di Matteo T., Hernquist L., *2005a*, MNRAS, 361, 776

Springel V., et al.,*2005b*, Nature, 435, 629

Stark D. P., *2016*, ARA&A, 54, 761

Stark D. P., Ellis R. S., Chiu K., Ouchi M., Bunker A., *2010*, MNRAS, 408, 1628

Steidel C. C., Adelberger K. L., Giavalisco M., Dickinson M., Pettini M., *1999*, ApJ, 519, 1

Stinson G., Seth A., Katz N., Wadsley J., Governato F., Quinn T., *2006*, MNRAS, 373, 1074

Stinson G. S., Brook C., Macciò A. V., Wadsley J., Quinn T. R., Couchman H. M. P., *2013*, MNRAS, 428, 129

Sugimura K., Omukai K., Inoue A. K., *2014*, MNRAS, 445, 544

Tacconi L. J., Neri R., Genzel R., Combes F., Bolatto A., Cooper M. C., Wuyts S., Bournaud F. et al., *2013*, ApJ, 768, 74

Takeuchi T. T., Yuan F.-T., Ikeyama A., Murata K. L., Inoue A. K., *2012*, ApJ, 755, 144

Tamura Y., Mawatari K., Hashimoto T., Inoue A. K., Zackrisson E., Christensen L., Binggeli C., Matsuda Y. e. a., *2019*, ApJ, 874, 27

Tegmark M., Silk J., Rees M. J., Blanchard A., Abel T., Palla F., *1997*, ApJ, 474, 1

Thacker R. J., Couchman H. M. P., *2001*, ApJL, 555, L17

Todini P., Ferrara A., *2001*, MNRAS, 325, 726

Trebitsch M., Blaizot J., Rosdahl J., Devriendt J., Slyz A., *2017*, MNRAS, 470, 224

Trenti M., Stiavelli M., *2009*, ApJ, 694, 879

Trenti M., Padoan P., Jimenez R., *2015*, ApJL, 808, L35

Vallini L., Gallerani S., Ferrara A., Pallottini A., Yue B., *2015*, ApJ, 813, 36

Valtchanov I., et al.,*2011*, MNRAS, 415, 3473

Verner D. A., Ferland G. J., Korista K. T., Yakovlev D. G., *1996*, ApJ, 465, 487

Vishwas A., et al.,*2018*, ApJ, 856, 174

Vogelsberger M., et al.,*2014*, MNRAS, 444, 1518

Wang T., et al.,*2019*, Nature, 572, 211

Watson D., Christensen L., Knudsen K. K., Richard J., Gallazzi A., Michałowski M. J., *2015*, Nature, 519, 327

Webber W. R., *1998*, ApJ, 506, 329

Weinberg S., *1989*, Reviews of Modern Physics, 61, 1

Weingartner J. C., Draine B. T., *2001*, ApJ, 548, 296

White S. D. M., Frenk C. S., *1991*, ApJ, 379, 52

White S. D. M., Rees M. J., *1978*, MNRAS, 183, 341

Wiersma R. P. C., Schaye J., Smith B. D., *2009a*, MNRAS, 393, 99

Wiersma R. P. C., Schaye J., Theuns T., Dalla Vecchia C., Tornatore L., *2009b*, MNRAS, 399, 574

Wilkins S. M., Feng Y., Di-Matteo T., Croft R., Stanway E. R., Bunker A., Waters D., Lovell C., *2016*, MNRAS, 460, 3170

Wise J. H., Abel T., *2007*, ApJ, 665, 899

Wise J. H., Abel T., *2008*, ApJ, 685, 40

Wise J. H., Cen R., *2009*, ApJ, 693, 984

Wise J. H., Abel T., Turk M. J., Norman M. L., Smith B. D., *2012a*, MNRAS, 427, 311

Wise J. H., Turk M. J., Norman M. L., Abel T., *2012b*, ApJ, 745, 50

Wise J. H., Demchenko V. G., Halicek M. T., Norman M. L., Turk M. J., Abel T., Smith B. D., *2014*, MNRAS, 442, 2560

Wolcott-Green J., Haiman Z., Bryan G. L., *2011*, MNRAS, 418, 838

Wolfire M. G., Tielens A. G. G. M., Hollenbach D., *1990*, ApJ, 358, 116

Wolfire M. G., McKee C. F., Hollenbach D., Tielens A. G. G. M., *2003*, ApJ, 587, 278

Wyithe J. S. B., Loeb A., *2011*, MNRAS, 413, L38

Xu H., Wise J. H., Norman M. L., Ahn K., O'Shea B. W., *2016*, ApJ, 833, 84

Yajima H., Li Y., *2014*, MNRAS, 445, 3674

Yajima H., Choi J.-H., Nagamine K., *2011*, MNRAS, 412, 411

Yajima H., Li Y., Zhu Q., Abel T., *2012a*, MNRAS, 424, 884

Yajima H., Choi J.-H., Nagamine K., *2012b*, MNRAS, 427, 2889

Yajima H., Nagamine K., Thompson R., Choi J.-H., *2014a*, MNRAS, 439, 3073

Yajima H., Li Y., Zhu Q., Abel T., Gronwall C., Ciardullo R., *2014b*, MNRAS, 440, 776

Yajima H., Shlosman I., Romano-Díaz E., Nagamine K., *2015a*, MNRAS, 451, 418

Yajima H., Li Y., Zhu Q., Abel T., *2015b*, ApJ, 801, 52

Yajima H., Ricotti M., Park K., Sugimura K., *2017a*, ApJ, 846, 3

Yajima H., Nagamine K., Zhu Q., Khochfar S., Dalla Vecchia C., *2017b*, ApJ, 846, 30

Yajima H., Sugimura K., Hasegawa K., *2018*, MNRAS, 477, 5406

Yang M., Greve T. R., Dowell C. D., Borys C., *2007*, ApJ, 660, 1198

Yoshida N., Abel T., Hernquist L., Sugiyama N., *2003*, ApJ, 592, 645

Yoshida N., Omukai K., Hernquist L., Abel T., *2006*, ApJ, 652, 6

Yoshida N., Omukai K., Hernquist L., *2008*, Science, 321, 669

Yoshii Y., Peterson B. A., *1995*, ApJ, 444, 15

Younger J. D., Fazio G. G., Huang J.-S., Yun M. S., Wilson G. W., Ashby M. L. N., Gurwell M. A., Peck A. B. et al., *2009*, ApJ, 704, 803

Zavala J., Okamoto T., Frenk C. S., *2008*, MNRAS, 387, 364

Zel'Dovich Y. B., *1970*, A&A, 500, 13

Zheng Z., Cen R., Trac H., Miralda-Escudé J., *2010*, ApJ, 716, 574

da Cunha E., et al.,*2013*, ApJ, 766, 13